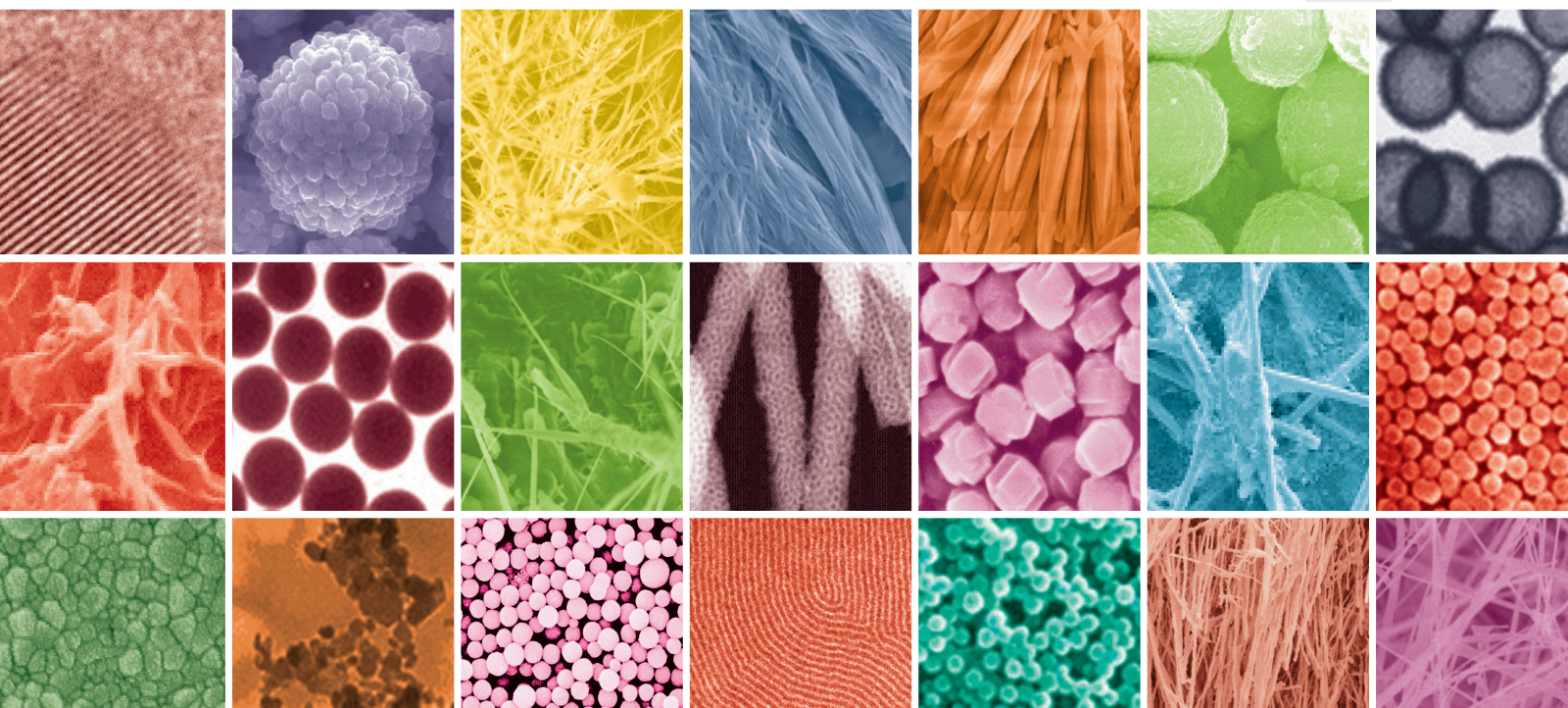


Advanced Nanomaterials for Applications in Photonic and Sensor Devices

Lead Guest Editor: Sheng-Joue Young

Guest Editors: Shoou-Jinn Chang and Yi-Hsing Liu





Advanced Nanomaterials for Applications in Photonic and Sensor Devices

**Advanced Nanomaterials for
Applications in Photonic and Sensor
Devices**

Lead Guest Editor: Sheng-Joue Young

Guest Editors: Shoou-Jinn Chang and Yi-Hsing Liu

Chief Editor

Stefano Bellucci, Italy

Editorial Board

Domenico Acierno, Italy
Katerina Aifantis, USA
Ibrahim Alarifi, Saudi Arabia
Nageh K. Allam, USA
Martin Andersson, Sweden
Raul Arenal, Spain
Hassan Azzazy, Egypt
Vincenzo Baglio, Italy
Lavinia Balan, France
Thierry Baron, France
Andrew R. Barron, USA
Enrico Bergamaschi, Italy
Debes Bhattacharyya, New Zealand
Sergio Bietti, Italy
Raghvendra A. Bohara, India
Mohamed Bououdina, Bahrain
Victor M. Castaño, Mexico
Albano Cavaleiro, Portugal
Bhanu P. S. Chauhan, USA
Shafiu Chowdhury, USA
Yu-Lun Chueh, Taiwan
Elisabetta Comini, Italy
Giuseppe Compagnini, Italy
David Cornu, France
Miguel A. Correa-Duarte, Spain
P. Davide Cozzoli, Italy
Anuja Datta, USA
Loretta L. Del Mercato, Italy
Yong Ding, USA
Yu Dong, Australia
Zehra Durmus, Germany
Ovidiu Ersen, France
Ana Espinosa, France
Claude Estournès, France
Rajalakshmanan Eswaramoorthy, India
Giuliana Faggio, Italy
Andrea Falqui, Saudi Arabia
Matteo Ferroni, Italy
Ilaria Fratoddi, Italy
C.L. Gan, Taiwan
Siddhartha Ghosh, Singapore
Filippo Giubileo, Italy
Iaroslav Gnilitskyi, Ukraine
Fabien Grasset, Japan

Jean M. Greneche, France
Kimberly Hamad-Schifferli, USA
Simo-Pekka Hannula, Finland
Michael Harris, USA
Yasuhiko Hayashi, Japan
Michael Z. Hu, USA
Zafar Iqbal, USA
Balachandran Jeyadevan, Japan
Hassan Karimi-Maleh, Iran
Antonios Kelarakis, United Kingdom
Ali Khorsand Zak, Iran
Philippe Knauth, France
Prashant Kumar, United Kingdom
Eric Le Bourhis, France
Shijun Liao, China
Meiyong Liao, Japan
Silvia Licoccia, Italy
Nathan C. Lindquist, USA
Zainovia Lockman, Malaysia
Jim Low, Australia
Gaurav Mago, USA
Muhamamd A. Malik, United Kingdom
Ivan Marri, Italy
Laura Martinez Maestro, United Kingdom
Sanjay R. Mathur, Germany
Tony McNally, United Kingdom
Yogendra Mishra, Denmark
Paulo Cesar Morais, Brazil
Paul Munroe, Australia
Jae-Min Myoung, Republic of Korea
Rajesh R. Naik, USA
Albert Nasibulin, Russia
Toshiaki Natsuki, Japan
MU NAUSHAD, Saudi Arabia
Hiromasa Nishikiori, Japan
Sherine Obare, USA
Won-Chun Oh, Republic of Korea
Abdelwahab Omri, Canada
Ungyu Paik, Republic of Korea
Dillip K. Panda, USA
Mazeyar Parvinzadeh Gashti, Canada
Edward A. Payzant, USA
Alessandro Pegoretti, Italy
Oscar Perales-Pérez, Puerto Rico





Jorge Pérez-Juste, Spain
Suresh Perumal, India
Alexey P. Popov, Finland
Ram Prasad, India
Thathan Premkumar, Republic of Korea
Helena Prima-García, Spain
Alexander Pyatenko, Japan
Haisheng Qian, China
You Qiang, USA
Philip D. Rack, USA
Mohammad Rahimi-Gorji, Belgium
Ilker S. Bayer, Italy
Lucien Saviot, France
Shu Seki, Japan
Gaurav Sharma, India
Donglu Shi, USA
Surinder Singh, USA
Bhanu P. Singh, India
Vladimir Sivakov, Germany
Pingan Song, Australia
Adolfo Speghini, Italy
Kishore Sridharan, India
Marinella Striccoli, Italy
Andreas Stylianou, Cyprus
Fengqiang Sun, China
Ashok K. Sundramoorthy, India
Angelo Taglietti, Italy
Bo Tan, Canada
Leander Tapfer, Italy
Valeri P. Tolstoy, Russia
Muhammet S. Toprak, Sweden
Sri Ramulu Torati, Republic of Korea
R. Torrecillas, Spain
Achim Trampert, Germany
Adriana Trapani, Italy
Takuya Tsuzuki, Australia
Tamer Uyar, USA
Cristian Vacacela Gomez, Ecuador
Luca Valentini, Italy
Viet Van Pham, Vietnam
Antonio Vassallo, Italy
Ester Vazquez, Spain
Ajayan Vinu, Australia
Ruibing Wang, Macau
Magnus Willander, Sweden
Zhi Li Xiao, USA
Ping Xiao, United Kingdom

Yingchao Yang, USA
Hui Yao, China
Yoke K. Yap, USA
Dong Kee Yi, Republic of Korea
Jianbo Yin, China
William Yu, USA
Michele Zappalorto, Italy
Wenhui Zeng, USA
Renyun Zhang, Sweden


Contents

Advanced Nanomaterials for Applications in Photonic and Sensor Devices

Sheng-Joue Young , Shouu-Jinn Chang , and Yi-Hsing Liu




Editorial (2 pages), Article ID 9895385, Volume 2022 (2022)

Development of a Continuous Blood Pressure Measurement and Cardiovascular Multi-Indicator Platform for Asian Populations by Using a Back Propagation Neural Network and Dual Photoplethysmography Sensor Signal Acquisition Technology

Chih-Ta Yen , Sheng-Nan Chang, and Cheng-Yang Cai

Research Article (15 pages), Article ID 6613817, Volume 2021 (2021)

Characteristics of Metal–Semiconductor–Metal Ultraviolet Photodetectors Based on Pure ZnO/Amorphous IGZO Thin-Film Structures

Kin-Tak Lam, Sheng-Joue Young , Yen-Lin Chu , Chi-Nan Tsai, Tung-Te Chu, Ting-Sung Lu, and Liang-Wen Ji 




Research Article (6 pages), Article ID 6649200, Volume 2021 (2021)

Development of Detection Equipment for a Polymerase Chain Reaction with a Loop-Mediated Isothermal Amplification Reaction

Wei-Chien Weng  and Yu-Cheng Lin 

Research Article (9 pages), Article ID 5513772, Volume 2021 (2021)

Biosynthesis of Zinc Oxide Nanoparticles Using Aqueous Piper betle Leaf Extract and Its Application in Surgical Sutures

Quynh Mai Thi Tran, Hong Anh Thi Nguyen , Van-Dat Doan , Quang-Hieu Tran, and Van Cuong Nguyen 

Research Article (15 pages), Article ID 8833864, Volume 2021 (2021)

Determination of the Immunoglobulin G Spectrum by Surface-Enhanced Raman Spectroscopy Using Quasispherical Gold Nanoparticles

Alejandra Ortiz-Dosal , Elizabeth Loredó-García, Ana Gabriela Álvarez-Contreras, Juan Manuel Núñez-Leyva, Luis Carlos Ortiz-Dosal, and Eleazar Samuel Kolosovas-Machuca 

Research Article (6 pages), Article ID 8874193, Volume 2021 (2021)

Design and Synthesis of Nanostructured Materials for Sensor Applications

Naumih M. Noah 

Review Article (20 pages), Article ID 8855321, Volume 2020 (2020)

Editorial

Advanced Nanomaterials for Applications in Photonic and Sensor Devices

Sheng-Joue Young¹, Shouu-Jinn Chang², and Yi-Hsing Liu²

¹Department of Electronic Engineering, National United University, Miaoli City 36063, Taiwan

²Institute of Microelectronics, Department of Electrical Engineering, National Cheng Kung University, Tainan 701, Taiwan

Correspondence should be addressed to Sheng-Joue Young; shengjoueyoung@gmail.com
and Shouu-Jinn Chang; changsj@mail.ncku.edu.tw

Received 21 January 2022; Accepted 21 January 2022; Published 12 February 2022

Copyright © 2022 Sheng-Joue Young et al. This is an open access article distributed under the Creative Commons Attribution License, which permits unrestricted use, distribution, and reproduction in any medium, provided the original work is properly cited.

In recent years, nanostructures for photonic/sensor device applications have been increasingly developed because of their flexibility and light weight for daily use, making them deployable. Therefore, photonic/sensor devices have been the subject of much interest. Photonic/sensor devices are environmentally sustainable, considering the availability of nanostructured raw materials. The main goal of this special issue is to discover new scientific knowledge relevant to IOT-based intelligent sensor systems and applied materials in nanoscience and nanotechnology.

This special issue collected five excellent papers. The published papers are introduced as follows.

Prof. C.-T. Yen et al. reported on “Development of a Continuous Blood Pressure Measurement and Cardiovascular Multi-Indicator Platform for Asian Populations by Using a Back Propagation Neural Network and Dual Photoplethysmography Sensor Signal Acquisition Technology.” This study proposed a measurement platform for continuous blood pressure estimation based on dual photoplethysmography sensors and a back propagation neural network (BPNN) that can be used for the continuous and rapid measurement of blood pressure and analysis of cardiovascular-related indicators. To increase the robustness of the BPNN model, the authors input data of 100 Asian participants into the training database, including those with and without cardiovascular disease, each with a proportion of approximately 50%. The proposed real-time blood pressure measurement system exhibited a mean accuracy of 98.22% and 95.58% for SBP and DBP, respectively.

Prof. K.-T. Lam et al. reported on “Characteristics of Metal–Semiconductor–Metal Ultraviolet Photodetectors Based on Pure ZnO/Amorphous IGZO Thin-Film Structures.” In this study, metal–semiconductor–metal-structured ultraviolet (UV) photodetectors (PDs) based on pure zinc oxide (ZnO) and amorphous indium gallium ZnO (a-IGZO) thin films were fabricated and characterized. The ZnO seed layers were deposited on corning glass substrates via a radio frequency magnetron sputtering technique. Results showed that under a 5 V applied bias, the dark currents of the pure ZnO and a-IGZO thin films were 0.112 pA and 2.85 nA, respectively. Meanwhile, the UV-to-visible rejection ratios of the pure ZnO and a-IGZO thin films were 14.33 and 256, respectively. Finally, the PDs of the a-IGZO thin films had a lower leakage current and higher rejection ratio than the pure ZnO thin films from the UV-to-visible light region.

Q. M. Thi Tran et al. reported on “Biosynthesis of Zinc Oxide Nanoparticles Using Aqueous Piper betle Leaf Extract and Its Application in Surgical Sutures.” In this study, the authors aimed to synthesize ZnO nanoparticles (NPs) by using Piper betle leaf extract and used it to coat the suture. The effect of synthesis parameters on the size and morphology of the ZnO NPs was also analyzed. The UV-Vis spectrum indicated the formation of ZnO NPs at approximately 370 nm. The volume of leaf extract plays a role in controlling the size and morphology of ZnO NPs. The average particle size of the as-synthesized ZnO NPs was approximately 112 nm with a hexagonal and spherical shape. The results proved that

Sheng-Joue Young
Shoou-Jinn Chang
Yi-Hsing Liu

the ZnO NPs performed a high antibacterial activity against *Staphylococcus aureus* and *Escherichia coli* with its antibacterial effectiveness up to 5 days. The ZnO NP-coated sutures also exhibited a high performance on bacterial inactivation. With key findings, this study largely contributed to lowering the burden on medical services in terms of medical treatment cost in developing countries.

A. Ortiz-Dosal et al. reported on “Determination of the Immunoglobulin G Spectrum by Surface-Enhanced Raman Spectroscopy Using Quasispherical Gold Nanoparticles.” This study is aimed at determining the Raman spectrum of IgG at physiological concentrations using quasispherical gold NPs as a surface-enhanced Raman spectroscopy (SERS) substrate. **Methods.** We initially determined the Raman spectrum of IVIG at 5%. Subsequently, for SERS characterization, decreasing dilutions of the protein were prepared by adding deionized water and an equal volume of the 5 nm gold quasispherical NP colloid. For each protein concentration, the Raman spectrum was determined using a 10x objective. We focused the 532 and 785 nm laser on the sample surface in a range of 500–1800 cm⁻¹, with five acquisitions and an acquisition time of 30 s. **Results.** We obtained the IVIG spectrum using SERS up to a concentration of 75 mg/dL. The Raman bands correspond to aromatic amino acid side chains and the characteristic beta-sheet structure of IgG. **Conclusion.** The use of 5 nm quasispherical gold NPs as a SERS substrate allows for detecting the Raman spectrum of IVIG at physiological concentrations.

N. M. Noah reported on “Design and Synthesis of Nanostructured Materials for Sensor Applications.” The development of sensor devices with improved characteristics, such as sensitivity, low cost, fast response, reliability, rapider recovery, reduced size, in situ analysis, and simple operation, has attracted increasing attention. Nanostructured materials have shown great potential in improving these properties for chemical and biological sensors. Different nanostructured materials have been used in manufacturing nanosensors, which include nanoscale wires (capability of high detection sensitivity), carbon nanotubes (very high surface area and high electron conductivity), thin films, metal and metal oxide NPs, polymer, and biomaterials. This review provides different methods that have been used in the synthesis and fabrication of these nanostructured materials followed by an extensive review of the recent developments of metal, metal oxides, carbon nanotubes, and polymer nanostructured materials in sensor applications.

Conflicts of Interest

We, the guest editorial team of the special issue, declare that we do not have any conflict of interest or private agreements with companies.

Acknowledgments

The guest editors would like to thank the authors for their contributions to this special issue and all the reviewers for their constructive comments.

Research Article

Development of a Continuous Blood Pressure Measurement and Cardiovascular Multi-Indicator Platform for Asian Populations by Using a Back Propagation Neural Network and Dual Photoplethysmography Sensor Signal Acquisition Technology

Chih-Ta Yen ¹, Sheng-Nan Chang,² and Cheng-Yang Cai³

¹Department of Electrical Engineering, National Taiwan Ocean University, Keelung City 202301, Taiwan

²Division of Cardiology, Department of Internal Medicine, National Taiwan University, Yun-Lin Branch, Dou-Liu City 640, Taiwan

³Department of Electrical Engineering, National Formosa University, Yunlin County 632, Taiwan

Correspondence should be addressed to Chih-Ta Yen; chihtayen@gmail.com

Received 25 December 2020; Revised 1 February 2021; Accepted 30 April 2021; Published 29 May 2021

Academic Editor: Victor M. Castano

Copyright © 2021 Chih-Ta Yen et al. This is an open access article distributed under the Creative Commons Attribution License, which permits unrestricted use, distribution, and reproduction in any medium, provided the original work is properly cited.

This study proposed a measurement platform for continuous blood pressure estimation based on dual photoplethysmography (PPG) sensors and a back propagation neural network (BPNN) that can be used for continuous and rapid measurement of blood pressure and analysis of cardiovascular-related indicators. The proposed platform measured the signal changes in PPG and converted them into physiological indicators, such as pulse transit time (PTT), pulse wave velocity (PWV), perfusion index (PI), heart rate (HR), and pulse wave analysis (PWA); these indicators were then fed into the BPNN to calculate blood pressure. The hardware of the experiment comprised 2 PPG components (i.e., Raspberry Pi 3 Model B and analog-to-digital converter [MCP3008]), which were connected using a serial peripheral interface. The BPNN algorithm converted the stable dual PPG signals acquired from the strictly standardized experimental process into various physiological indicators as input parameters and finally obtained the systolic blood pressure (SBP) and diastolic blood pressure (DBP). To increase the robustness of the BPNN model, this study input data of 100 Asian participants into the training database, including those with and without cardiovascular disease, each with a proportion of approximately 50%. The experimental results revealed that the mean and standard deviation of SBP were 2.23 ± 2.24 mmHg, with a mean squared error of 3.15 mmHg. The mean and standard deviation of DBP was 3.5 ± 3.53 mmHg, with a mean squared error of 4.96 mmHg. The proposed real-time blood pressure measurement system exhibited a mean accuracy of 98.22% and 95.58% for SBP and DBP, respectively.

1. Introduction

Hypertension remains a major factor in cardiovascular disease in Taiwan, and it is also a considerable global health concern. Hypertension is a crucial indicator of whether the human heart is functioning normally. The related treatment process is long and challenging, and people still have extremely low awareness of hypertension. Research has revealed that in those aged between 19 and 44 years, the prevalence of prehypertension is higher than the proportion of patients with hypertension. The age trend is also decreasing, suggesting that cardiovascular disease is no longer a concern

only for older adults. Factors such as family medical history, eating habits, living habits, work stress, fatigue, temperature, and aging are all closely related to cardiovascular disease.

Research on photoplethysmography (PPG) is increasing, and numerous scholars have discussed its measurement methods, signal processing, algorithm applications, measurement applications, hardware improvement and innovation, and system construction. As early as 1937, Hertzman and Spielman [1] proposed the concept of PPG by using optical measurement of blood volume changes. Burton [2] observed strong correlations among systolic blood pressure (SBP) of the finger, pulse rate, and the sympathetic nervous system.

Mendelson and Ochs [3] developed a sensor for reflectance pulse oximetry to evaluate a prototype skin-reflectance pulse oximeter in humans. In 1994, Nitzan [4] used PPG to produce two parameters, namely, amplitude modulation (AM) and baseline, and proved that the PPG signal and heart rate (HR) variability have similar spectral sections. In addition, Task Force [5] and Nakajima [6] have both confirmed the correlation between PPG signal, and HR. Rhee et al. [7] proposed a finger-ring plethysmographic sensor, indicating that PPG can continuously monitor arterial pulsation without causing harm. Numerical simulations and experiments were conducted to verify and evaluate the aforementioned model. In the same year, Chan et al. [8] proposed a noninvasive and cuffless measurements of blood pressure for telemedicine. This technology used the time interval between electrocardiography (ECG) and PPG to predict the systolic, diastolic, and mean blood pressure on the basis of the pulse transit time (PTT) technology, and it applied the wireless application protocol to display information on portable wireless devices. Moreover, Murthy et al. [9] analyzed the spectrum of PPG signals in cardiovascular patients; they noted that PPG can be used as an alternative diagnostic tool for studying the cardiovascular system, particularly HR variability. Teng and Zhang [10] confirmed the feasibility of continuous and non-invasive estimation of arterial pressure by using PPG. The aforementioned works have confirmed the application of PPG for measuring and analyzing health conditions and characteristics as feasible; they also revealed that the PPG sensor can effectively reflect the relationship between the heart and the blood vessel, leading to its extensive use.

Various methods for measuring blood pressure-related physiological signals have been proposed. In signal processing, biological signals must be converted to electric potentials before the signals can be processed by computers or control devices. The biological signal is generally weak and accompanied by a range of noise; hence, the signal must be amplified through an amplifier and the noise filtered out. Subsequently, samples are taken through the alternating current (AC)/direct current (DC) converter; then, the analog signal is converted to a digital signal; finally, the digital signal is input into a computer for analysis. The biological signal mainly includes biomechanical and biooptical signals. Of these two, biomechanical signals are the more widely used in blood pressure measurement, as is the case in ECG and pulse sensors. Biooptical signals are increasingly being used to measure blood pressure, and the most representative measurement tool is PPG. Many related studies have also indicated that multiwavelength PPG can be used for cuffless blood pressure measurement [11–13].

Various methods related to measuring the correlation between blood and optics currently apply PPG for estimating blood pressure. They can generally be classified into PTT, pulse wave velocity (PWV), and pulse wave analysis (PWA). PWV is inversely correlated with PTT. Although the methods differ, the three variables are closely related [14]. However, in recent years, some scholars have proposed perfusion index (PI), which is defined as the ability of the cardiovascular system to provide sufficient blood for normal functioning and metabolism of body tissues. PI is also an

essential metric for judging the condition of the cardiovascular system [15].

PTT represents the time interval of the arterial pulse wave from the aortic valve to a peripheral artery; PTT is said to be inversely proportional to the change in blood pressure [16], and it can be used for noninvasive continuous blood pressure estimation. PTT is defined as the time between two specific parts of the PPG signal waveform. Both events occur at each heartbeat and can be easily detected. The main purpose is to study the relationship between the time course of the heart's electrical activity and cardiovascular activity. In the past few decades, PPG has also been widely applied to estimate blood pressure by using PTT [17–22]. Current clinical best practice involves starting the timing from the apex of the R wave in the ECG to the starting point of the largest upward branch in the PPG of a certain part of the peripheral artery blood flow. This measurement is now collectively referred to as PTT, which is typically the distance from the heart to the wrist or fingertips. Some scholars have also suggested the use of dual PPG to obtain PTT. This process involves using a peak detection algorithm to process two PPG signals and identify the peaks in each cardiac cycle, measuring the blood transit time from shoulder to finger, and calculating the sample difference between the two peaks [23]. Lin et al. [24] used PTT to estimate blood pressure and calibrated the system by using linear regression with reference to multiple data samples of blood pressure. However, under different conditions, the velocity of transferring energy formed by heart activity to the peripheral blood vessel differs. For example, vasoactive substances and autonomic tone can affect heart and blood vessel activity, thereby affecting blood flow.

For PWV, two PPG signals are used to analyze the PPG signal along the same artery branch at a known distance and set position simultaneously. A specific part of the signal is evaluated to identify the difference in time and distance between the two signals; these values are then used to calculate the PWV. This method, which is used to determine arteriosclerosis, has been extensively studied and proven in internal medicine [25]. In clinical medicine, PWV measurements are also used as a diagnostic parameter of arteriosclerosis. Although PWV has proven a direct correlation between blood pressure and measurement velocity [26, 27], a precise distance between the two sensors is required to accurately calculate blood pressure. However, the sensor may move over time or during the measurement, resulting in inaccurate calculation. Moreover, precise placement of the sensor is required to achieve optimal results.

PWA is used to evaluate the pressure waveform generated by systolic and diastolic flow in the arteries. It can accurately record the peripheral pressure waveform and generate the corresponding central waveform, from which the augmentation index and central pressure can be derived. PWA also includes the relevant characteristics of PTT and PWV. Clinical studies have indicated that PWA is a technology that produces reliable results and can be applied easily. Samria et al. [28] were the first to propose that using PWA to assess stiffness may provide a more satisfactory risk assessment and target treatment for those in greatest need. Blood vessel stiffness may not only be a sign of atherosclerosis but may also be

involved in the pathogenesis of cardiovascular diseases through diverse mechanisms. Therefore, the use of PWA to assess arterial stiffness may provide a more efficient risk assessment and enable treatment to be targeted to those who need it most. Nevertheless, to enable more accurate judgment and assessment, this technology must acquire a complete PPG waveform without interference. Therefore, Joseph et al. [29] suggested the use of discrete wavelet transform to strengthen the waveform characteristics and completeness by eliminating the damaged PPG signal caused by motion artifacts. In addition, Fischer et al. introduced a new embedded algorithm for real-time pulse waveform segmentation and artifact detection based on PPG time domain analysis to analyze various physiological indicators. Furthermore, Zhang [30] proposed a method on the basis of mean impact value combined with a genetic algorithm-back propagation neural network (BPNN) to improve the analysis accuracy of PPG waveforms for predicting blood pressure; the results of SBP and diastolic blood pressure (DBP) were 4.213 ± 5.609 mmHg and 3.230 ± 4.591 mmHg, respectively, proving again that the condition of the PPG waveform can affect the accuracy of blood pressure estimation.

2. Experimental and System Setup

2.1. Participants. The data source is cooperated with physicians from National Taiwan University Hospital, Yun-Lin Branch, to conduct a clinical trial after being granted approval by the relevant institutional review board. A total of 100 people participated in this study, including 57 outpatients from the cardiovascular disease department and 43 students from the National Formosa University. A large sample was desirable for increasing the number of data in the experimental database and improving the robustness of the BPNN algorithm model when measuring SBP and DBP.

(1) The inclusion criteria for this study were as follows:

- (i) Inpatients or outpatients with cardiovascular diseases who routinely undergo general physiological parameter examinations
- (ii) Students with normal blood pressure
- (iii) Patients over 20 years of age

(2) The exclusion criteria were as follows:

- (i) Pregnant women
- (ii) Children or minors (under 20 years old)
- (iii) People with mental disorders

This study used the dual PPG measurement method to capture waveform signals of the human body. The number

of male participants was 87, and their SBP and DBP ranged from 98 to 179 and 32 to 121, respectively. The SBP and DBP of the 13 female participants ranged from 99 to 193 and 57 to 102, respectively. The participants' age range, average height, average weight, SBP, and DBP are presented in Tables 1 and 2.

The experimental location was a quiet empty room next to the physician's office; the experimental environment is depicted in Figure 1. During the experiment, the participants did not have any contact or interaction with the physician. At the beginning of the experiment, the participants were provided with detailed information on the process and purpose of the experiment. The experiment started after patients signed the consent form. The crucial elements of the experiment are as follows:

- (1) Informed consent form
- (2) Dual PPG system
- (3) Raspberry Pi 3
- (4) Omron HEM-7070 (Omron Corporation, Kyoto, Japan) electronic blood pressure monitor
- (5) Lay participant's hands flat on a table, aligned with the position of the heart
- (6) Quiet environment
- (7) Basic information of experimental participants

In the experimental process, this study referred to a related study [43] on the influence of office blood pressure measurement on the diagnosis and treatment of hypertension. The study explored the use of noninvasive PPG for measuring human photoelectric signals and obtained relevant waveforms to identify the characteristics related to blood pressure. The experimental measurement process, BPNN training framework, and apparatus setup are illustrated in Figures 2, 3, and 4, respectively. The data of the participants were collected through the following procedure:

- (1) Male and female volunteers with and without cardiovascular disease were invited to participate in this study. All participants were informed regarding the research objective and experimental methods, and they subsequently signed an informed consent form
- (2) The participants placed both their hands at the same height as the heart and sat quietly (without talking) for 5 min; this enabled the researchers to obtain a stable PPG waveform and blood pressure
- (3) The inflatable sleeve (Omron) was wrapped around the left upper arm and compressed once every 2 min for a total of three times. The dual PPG was fixed on the index and middle fingers to measure the PPG signal waveform, and the waveform and conversion parameters were continuously recorded for approximately 5 min. The experiment had a duration of 10 min per person, and the collected data were used as the training data set of the BPNN

TABLE 1: Characteristics of male participants.

Parameters	Daily activity
Men	87
Age range (years)	20-88
Height (cm)	171 \pm 17
Weight (kg)	74 \pm 14
SBP range (mmHg)	128 \pm 15
DBP range (mmHg)	81 \pm 13

TABLE 2: Characteristics of female participants.

Parameters	Daily activity
Women	13
Age range (years)	20-84
Height (cm)	155 \pm 8
Weight (kg)	57 \pm 8
SBP range (mmHg)	132 \pm 25
DBP range (mmHg)	79 \pm 9



FIGURE 1: Experimental environment and apparatus layout.

- (4) The age, height, and weight of the participants were obtained after the experiment

2.2. Apparatus. This study implemented a continuous blood pressure measurement platform. The system included two green-light PPG sensors, a Raspberry Pi 3, an MCP3008, and an Omron blood pressure monitor. The two PPGs were clipped onto the index and middle fingers and were connected to the Raspberry Pi 3 through the serial peripheral interface (SPI). The MCP3008 was used to convert analog signals to digital signals, and Python syntax was used to process PPG signals to obtain signal waveforms and extract the characteristics. Finally, the Omron blood pressure monitor was used to measure blood pressure simultaneously on the same hand. After algorithm analysis and calculation, the researchers conducted conversion to obtain the HR, PTT, PWV, PI, and blood pressure-related data, and the SBP and DBP were calculated. The system structure is illustrated in Figure 5.

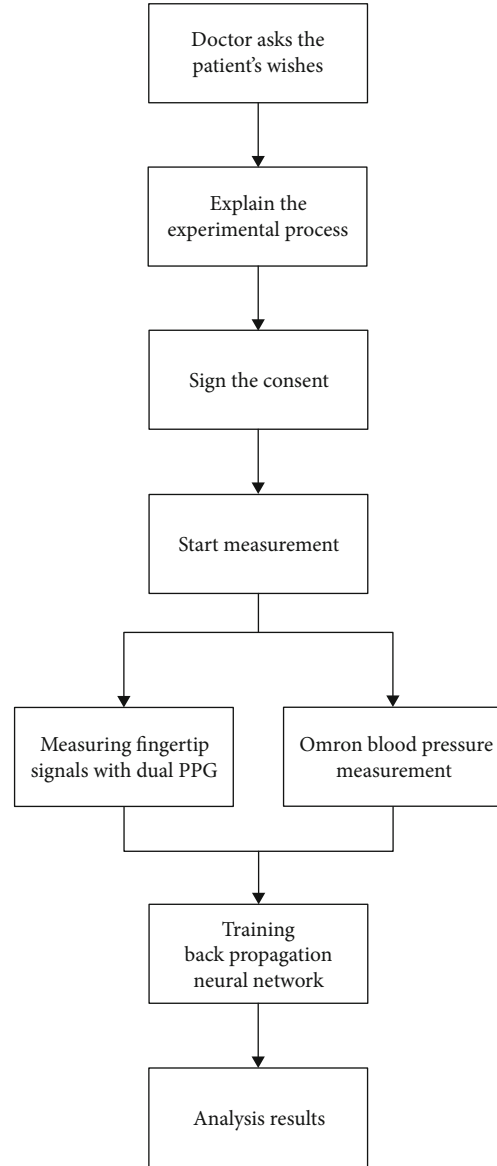


FIGURE 2: Flowchart of the clinical experiment.

2.3. PPG Sensor. PPG is often used in medical research to measure the signals of human subcutaneous tissue and is widely used to monitor the pulse of patients. The key components of a PPG are a light-emitting diode, photodiode, and amplifier. Thus, PPG is a simple and low-cost optical method that can be used to detect changes in blood volume in tissue capillary beds. In addition, the complete waveform composition of the PPG signal is a combination of DC and AC components. The DC component comes from the optical signal reflected or transmitted by tissue and is determined by tissue structure and the volume of venous and arterial blood; the AC component corresponds to the change in blood volume synchronized with the HR. The DC component indicates small changes in breathing, whereas the AC component changes with the HR and is superimposed on the DC baseline (Figure 6).

In the experiment, two sets of reflective pulse sensors were used, the sampling rate was set to 500 Hz, and the

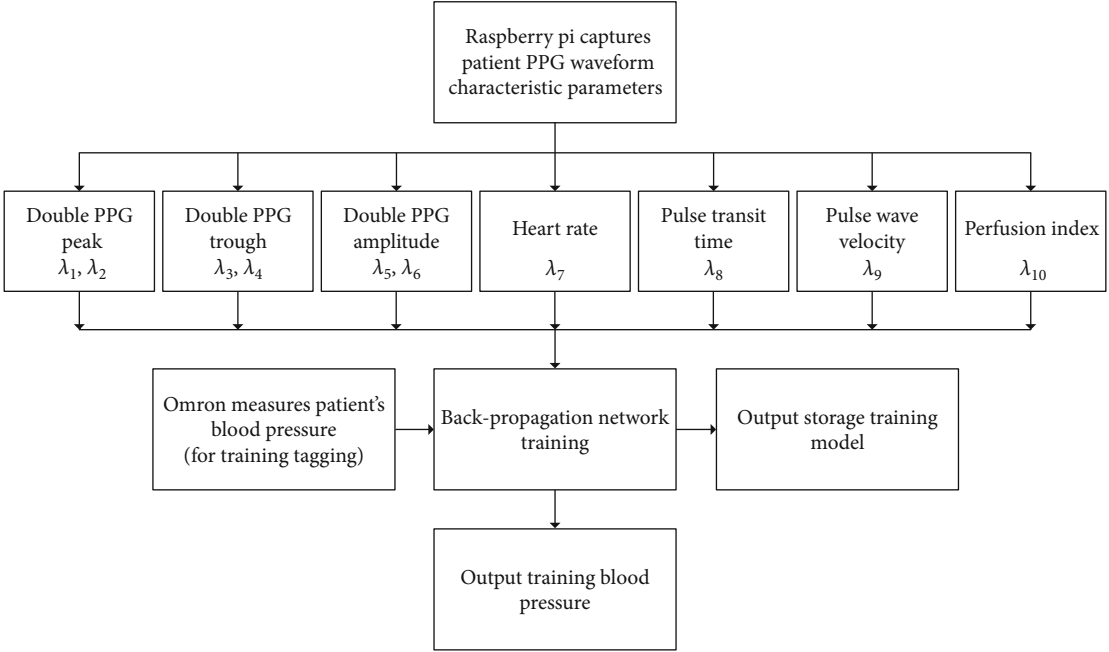


FIGURE 3: Flowchart of the proposed back propagation neural network.

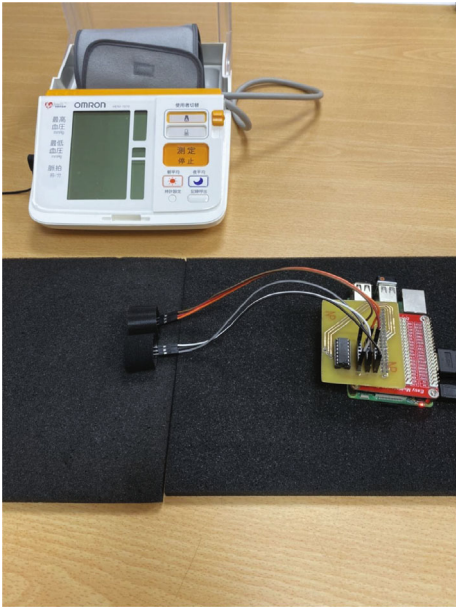


FIGURE 4: Apparatus setup.

transmitter module used a green light-emitting diode (AM2520ZGC09) with a peak wavelength of 515 nm. The pulse sensors were mainly designed for the multiple demands of discrete backlight and the necessity of maintaining high intensity and wide viewing angle radiation. In addition, the receiver used a miniature surface-mount ambient light photo sensor (APDS-9008) with a sensing peak wavelength of 565 nm. Highly sensitive and similar peak response wavelengths of the transmitter and receiver enable the display of a clearer pulse waveform.

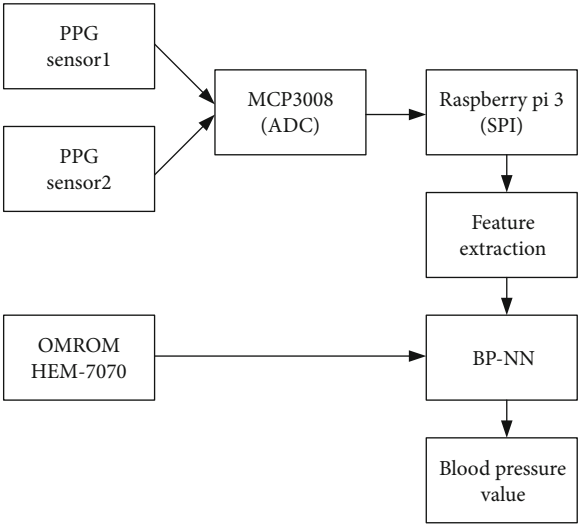


FIGURE 5: System structure diagram.

The pulse sensor proposed in this study adopted a reflective light sensor, which was tightly attached to the finger with a strap during measurement. The sensor was susceptible to a range of signal interference because the frequency band of the signal was generally between 0.05 and 200 Hz and the signal amplitude was extremely small (generally at the millivolt). Therefore, a general passive low-pass filter (model of passive RC: R, 100; C, 4.7uF) and MCP6001 were installed at the receiving end. An operational amplifier served as an amplifying filter module, with the purpose of reducing noise, increasing pulse wave amplitude, and amplifying the received signal by 330 times. The DC bias was set to half of the power supply voltage with a voltage divider, and the signal was

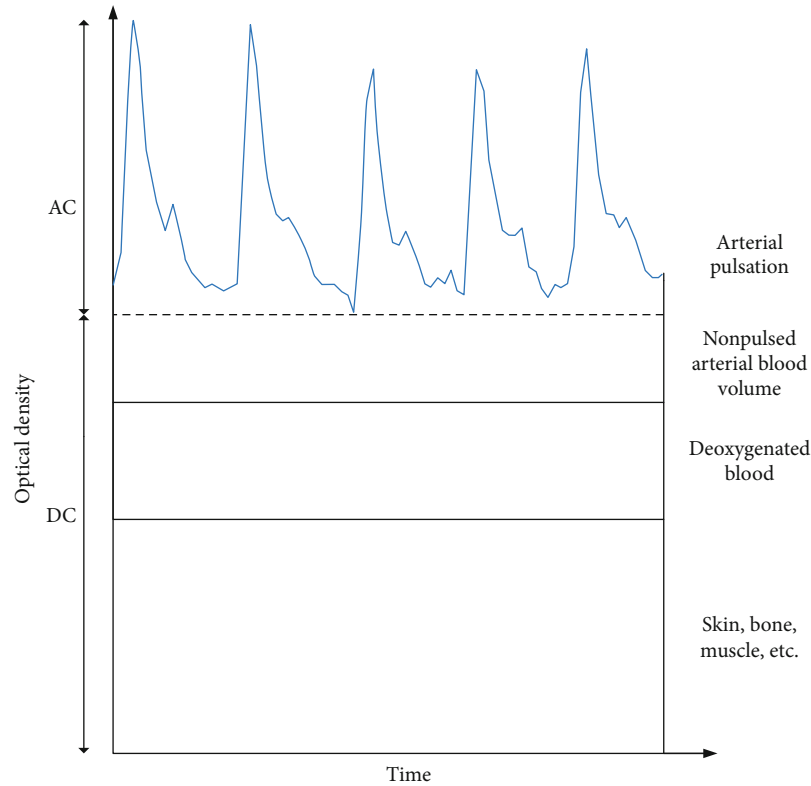


FIGURE 6: PPG signal composed of AC and DC components.

normalized near the reference point to facilitate the collection of the amplified PPG signal waveform by the Raspberry Pi 3. An anti-electric-shock design was also employed to protect the participants. The front and back of the sensor element are depicted in Figure 7.

2.4. Hardware System Design and Connection Method. This experimental system connected the Raspberry Pi 3, MCP3008, and PPG sensor through the SPI. Further details are as follows:

- (1) Digital Ground (DGND): the digital ground was connected to the internal digital circuit of the Raspberry Pi
- (2) Analog Inputs (CH0-CH7): analog inputs 0–7 corresponded to the PPG sensor signal input pins
- (3) Chip Select/Shutdown ($\overline{CS}/SHDN$): the SPI could start the communication between devices when it was set to a low voltage. The communication between the devices stopped and entered the wait state when the SPI was set to a high voltage. During communication, it must be set to a high voltage to enable communication
- (4) Serial Data Output (D_{OUT}): when SPI data were output, the timing of the data changed because of the communication changes between devices
- (5) Serial Data Input (D_{IN}): the SPI data that were input were used to upload the setting data to the communication device
- (6) Serial Clock (CLK): the SPI clock pin was used to start communication

2.5. Calibration and Comparison with Standard Apparatus. To verify the accuracy of the blood pressure converted by the experimental system, this study adopted the Omron electronic blood pressure monitor as the standard apparatus for comparison (Figure 8); its specifications are presented in Table 3 [31]. In the experimental measurement, the dual PPG signals were obtained, and the blood pressure was measured simultaneously; subsequently, the dual PPG signals were extracted and converted to be used in training the BPNN. Finally, test data of the two systems were compared to determine their accuracy.

3. Physiological Parameters Extracted from Experiments

Physiological parameters are crucial indicators for judging the condition of the human body. The use of diverse physiological parameters can assist physicians in judging the condition of their patients. This study mainly discussed the physiological indicators related to blood pressure, including HR, PWA, PTT, PWV, and PI as the training parameters of BPNN to devise a noninvasive continuous blood pressure measurement system.

3.1. Heart Rate. The heart is an essential organ in the human body and plays a critical role in the blood circulation system. The frequency of heart beats is called HR, which is a basic

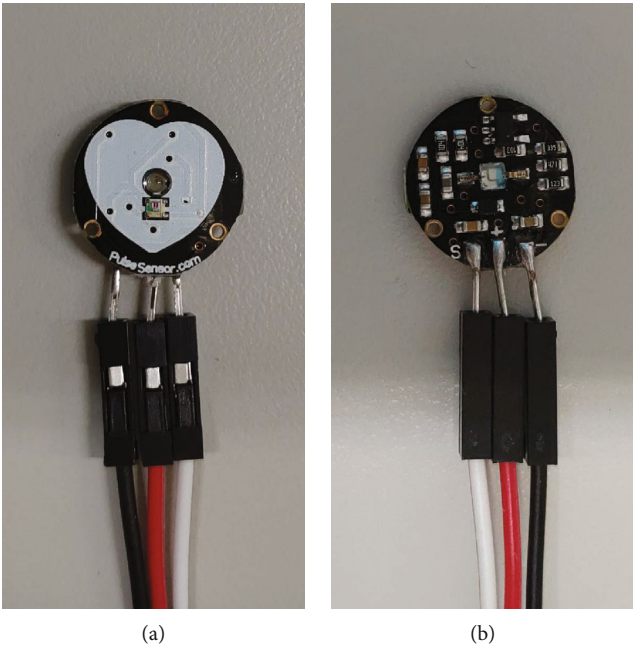


FIGURE 7: PPG pulse sensor: (a) front; (b) back.



FIGURE 8: Experimental verification by Omron HEM-7000 blood pressure monitor.

indicator of the physiological condition of the human body. HR is mostly measured in patients with hypertension, coronary heart disease, heart failure, or in patients under anesthesia or in the intensive care unit. It is also one of the vital signs that clinicians use during monitoring and management. Accurate and real-time HR monitoring can serve as a reference for the clinical assessment of a patient's condition and diagnosis as well as for treatment decisions.

The most common method to estimate HR is by using ECG to extract the R peaks in the QRS complex generated during each heartbeat (the QRS complex is regarded as the criterion of a heartbeat); the heartbeat interval, called the RR interval, occurs after two successive R peaks. According to relevant literature [6], the PPG signal has the same characteristics, and it can also extract P waves, which exhibit the

TABLE 3: Specification of blood pressure monitor.

OMRON HEM-7070 electronic blood pressure monitor	
Measurement method	Oscillometric
Measuring range	Pressure: 0–299 mmHg Pulse: 40–180 beats/min
Inflation	Fully automatic
Deflation	Electronic dynamic control
Precision	Pressure: within ± 3 mmHg Pulse rate: within $\pm 5\%$ read value
Pressure detection	Capacitive pressure sensor
Weight	Approximately 990 g
Size	131 \times 84 \times 155 mm (W \times H \times L)
Cuff	120 \times 480 mm (W \times H) Air tube length 660 mm

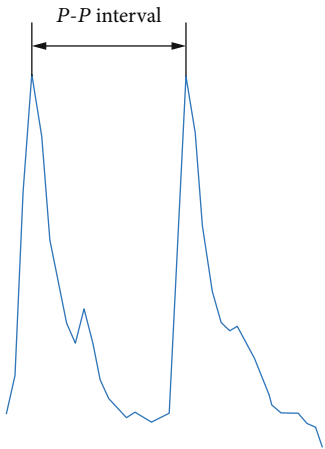


FIGURE 9: Peak-peak interval diagram.

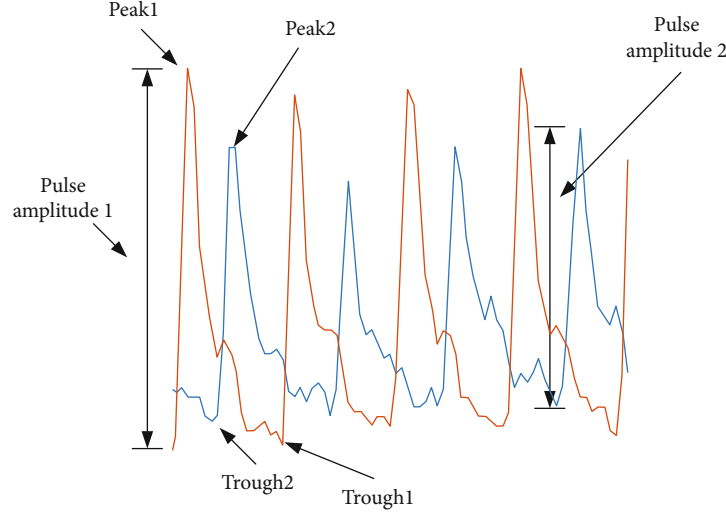


FIGURE 10: Pulse wave characteristic acquisition and analysis.

same characteristics as the ECG and form peak-peak intervals (Figure 9). A peak-peak interval in PPG is extracted by identifying the peak of each complete PPG signal; the time generated between each peak is the peak-peak interval. After averaging the value, it is converted to beats/min; the calculation formula is as follows:

$$HR = \left(\frac{1}{PPI_{\text{mean}}} \right) \times 60. \quad (1)$$

3.2. Pulse Transit Time and Pulse Wave Velocity. PTT and PWV refer to the time and flow rate of blood in the blood vessel, respectively. The harder the vascular wall is, the faster the blood flow becomes. By contrast, softer blood vessels can absorb the effect of blood flow and, thus, reduce the flow rate. Therefore, a larger PWV indicates a harder vascular wall, which means arteriosclerosis is ongoing. According to related studies, PTT is highly correlated with the incidence of cardiovascular disease. A higher PTT suggests a higher possibility of coronary artery disease. The calculation formula of PTT is as follows:

$$PWV = \frac{D}{PTT}, \quad (2)$$

where PTT is the pulse transit time and D is the distance between the two sensors (its definition differs in other methods). According to (2), PTT must be measured before calculating PWV.

3.3. PPG Pulse Wave Analysis. An intact and undisturbed PPG pulse wave can reflect the change in blood volume when the heart beats; thus, PWA typically uses a single PPG signal to estimate blood pressure. Most related studies have extracted parameters such as systolic time, diastolic time, 1/2 pulse amplitude, and maximum-minimum interval to estimate blood pressure. Although this technique improves the accuracy of blood pressure estimation, it must estimate

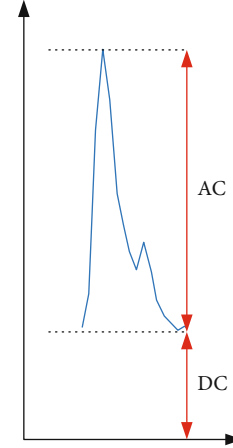


FIGURE 11: Pulse AM and DC component in PPG.

blood pressure according to pulse arrival time, and that can only be achieved when a complete and stable waveform is obtained [14]. Therefore, continuous blood pressure estimation is challenging with this technique. To solve the aforementioned problem, this study simplified the waveform characteristic acquisition method by extracting stable characteristics that appear on the waveform (i.e., peak and trough values of dual PPG and arbitrary amplitude value of the dual PPG during the measurement) (as illustrated in Figure 10).

3.4. Perfusion Index. PI [32] represents the ratio of the AM to the DC component in the PPG signal. Physiologically, this index represents the change in blood volume at the measurement location, which can be used to predict the change in stroke volume caused by blood arterial circulation. Faster pulsating blood flow can result in a greater pulsating component and PI value. The PPG signal obtains the AM and DC. Physiologically, AM relates to artery compliance, which is proportional to the change in tissue blood pulsation; DC (e.g., skin and veins) is related to the smallest end-diastolic volume of blood pulsating in physiological tissues. The

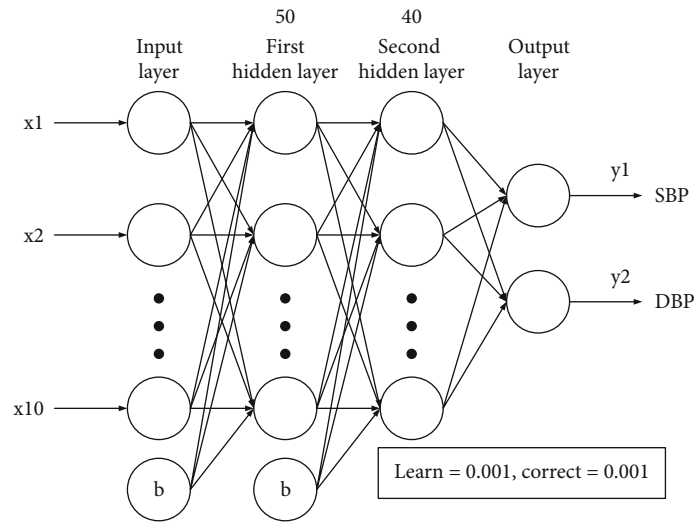


FIGURE 12: Schematic of dual PPG multifeature extraction through the use of BPNN.

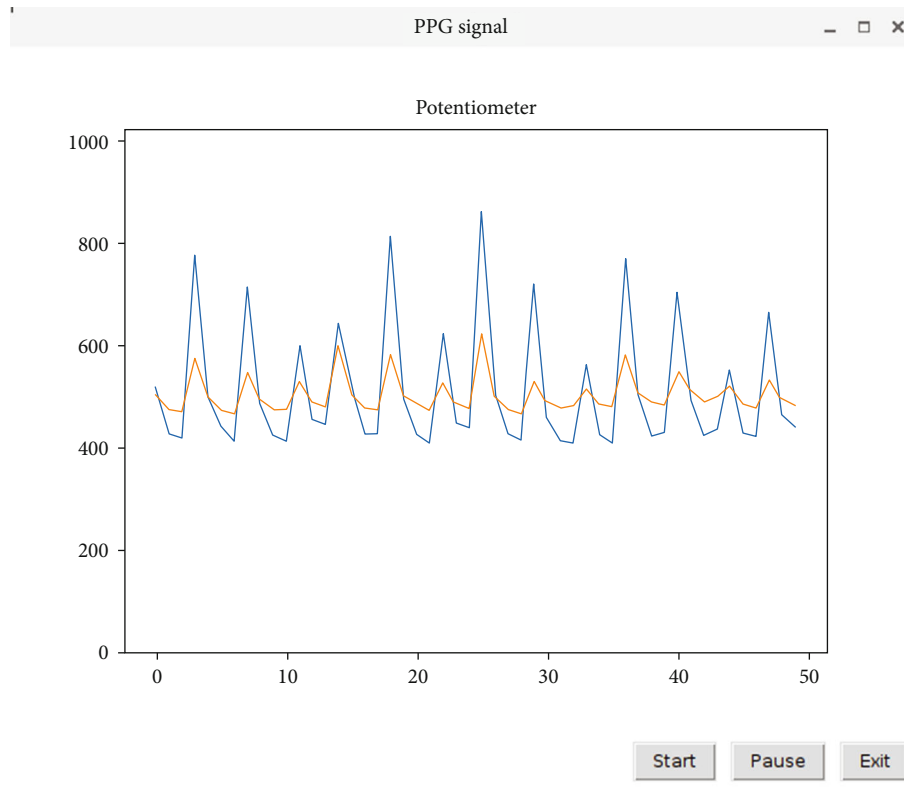


FIGURE 13: Graph of actual dual PPG measurement of the system.

change in blood volume of all sections in the tissue is proportional to the DC component. The AM is obtained by subtracting the trough value (V) from the peak value (P), and the DC component is acquired from V (Figure 11). Therefore, the formula for PI is as follows:

$$PI = \frac{AM}{DC}. \quad (3)$$

4. Design of the Back Propagation Neural Network

The BPNN adopted in this experiment used the characteristics related to blood pressure on the dual PPG signals as parameters; blood pressure, measured by a standard apparatus, was added as the reference value to obtain the blood pressure optimized by the BPNN. The algorithm was classified

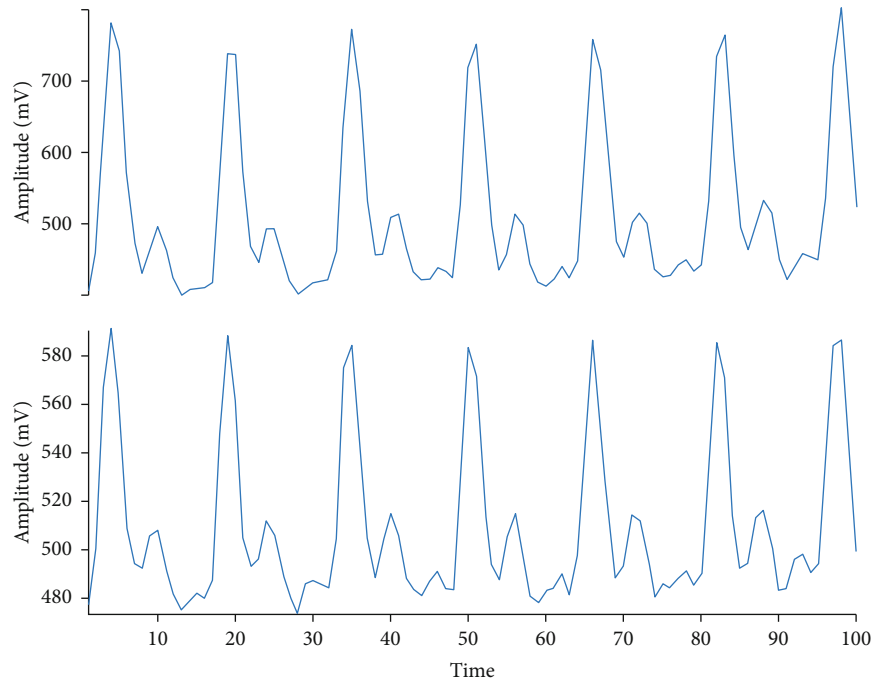


FIGURE 14: Measurement of dual PPG waveforms in participants without cardiovascular disease.

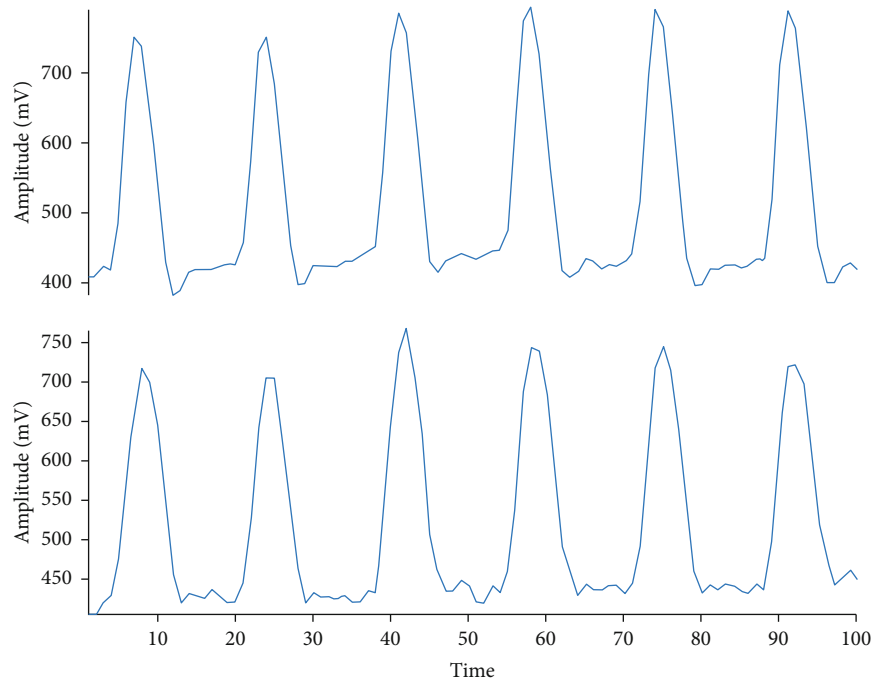


FIGURE 15: Measurement of dual PPG waveforms in participants with cardiovascular disease.

into two processes: the feedforward process and the back propagation and update process. Each iteration process forward transmitted an instance in the training set as well as calculated and saved the output of each neuron layer. The error was obtained by comparing the output of the last layer with the actual value, and the error rate of the output layer obtained from the calculation formula was used to update the weight and bias of each layer. The training sets were iteratively trained, and all the training sets were used in random

order in each iteration. Finally, the predicted value was output, and the model was saved. The following network structure was designed for this experiment:

(1) Input layer

(i) Total of 10 nodes

TABLE 4: Relationship between heart rate and blood pressure.

HR	SBP	DBP
70	99	71
67	105	32
68	112	78
58	125	68
99	134	57
91	145	81
79	150	103
76	168	114
77	176	115
74	187	121

TABLE 5: Relationship between PTT, PWV, and blood pressure.

PTT	PWV	SBP	DBP
0.044	52.273	99	71
0.043	53.488	105	32
0.036	63.889	112	78
0.018	127.778	125	68
0.007	328.571	134	57
0.007	328.571	145	81
0.005	460	150	103
0.003	657.142	168	114
0.003	766.666	176	115
0.002	1150	187	121

TABLE 6: Relationship between PWA and blood pressure.

PWA						SBP	DBP
472	498	479	579	483	579	99	71
487	508	477	533	490	551	105	32
453	491	467	579	492	572	112	78
498	509	505	524	492	579	125	68
472	488	458	578	482	579	134	57
493	497	451	516	478	579	145	81
562	640	426	574	482	564	150	103
534	787	415	572	473	579	168	114
647	728	424	578	470	576	176	115
559	844	384	579	463	578	187	121

(ii) Used 10 eigenvalues extracted by PPG as the input layer

(2) First hidden layer

(i) Total of 50 nodes

(ii) Added a bias

TABLE 7: Relationship between PI and blood pressure.

PI	SBP	DBP
12	99	71
11	105	32
12	112	78
16	125	68
16	134	57
19	145	81
15	150	103
18	168	114
19	176	115
22	187	121

(3) Second hidden layer

(i) Total of 40 nodes

(ii) Added a bias

(4) Output layer

(i) Total of two nodes

(ii) Output as SBP and DBP

The quite important issues are how to find the optimal parameters and hyperparameters of BPNN model. We first use single hidden layer BPNN model and modify the number of neurons in each layer to find the optimal solutions. If the performance is not good enough and then try to add the number of hidden layers and modify each number of neurons to decrease the errors of SBP and DBP values. After that, a total of 10 eigenvalues was input into the input layer. The activation function used to activate the first and second hidden layers was called sigmoid, and the activation function used in the process of back propagation and updating weights was called sigmoid_derivative. Adding a bias into each input layer can improve the activation of neurons. The number of neurons used in the first and second hidden layer were 50 and 40, respectively, with a learning rate of 0.001 and momentum factor of 0.001. The output layer estimated both SBP and DBP simultaneously; the number of iterations in this study was limited to 100,000. See Figure 12 for the network structure.

5. Selection and Analysis of Experimental Eigenvalues

Blood pressure is defined as the force exerted on arteries when blood enters the blood vessels. Therefore, this experiment extracted the eigenvalues from the dual PPG signals.

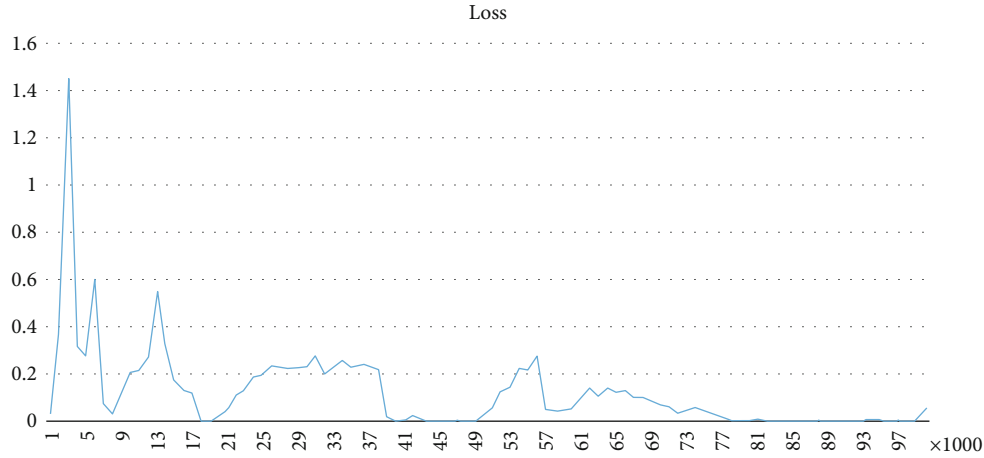


FIGURE 16: Training loss curve, recorded once every 1,000 iterations.

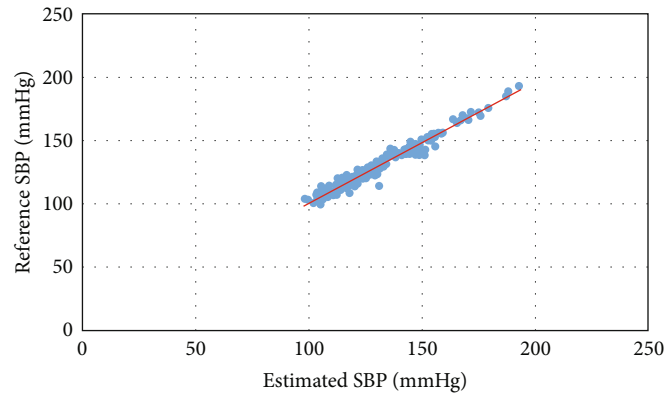


FIGURE 17: Scatter plot of the actual and estimated SBP in all participants.

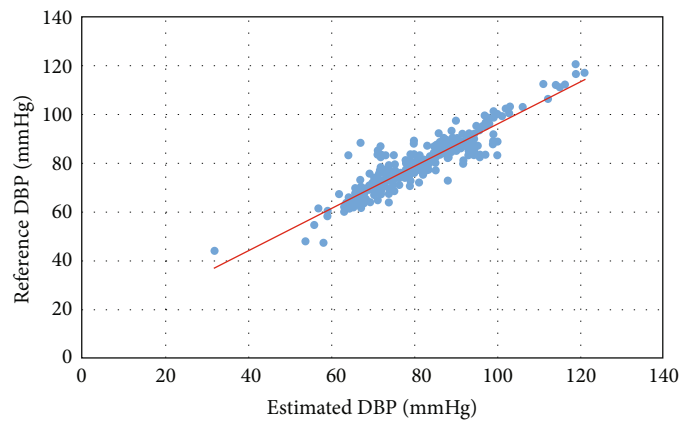


FIGURE 18: Scatter plot of the actual and estimated DBP in all participants.

The actual measurement on the graphical user interface is illustrated in Figure 13, and the dual PPG waveform measurement of healthy people and those with cardiovascular disease are shown in Figures 14 and 15, respectively. This study selected parameters that have a positive correlation with blood pressure and blood vessel condition as the characteristics to strengthen the full correlation of the neural network; these parameters were used as the inputs of the

BPNN. The experiment extracted HR, PTT, PWV, two PPG peaks, two PPG troughs, AM of the dual PPG during measurement, PI, and 10 eigenvalues. Their relationship is explained in the following sections.

5.1. HR. Under normal circumstances, people whose HR exceeds 80 beats/min have increased risk of hypertension. In 1998, a study noted that HR measurement can provide

crucial information regarding cardiovascular risks [33]. Table 4 presents data on the relationship between HR, SBP, and DBP of the 10 participants in that experiment. The data reveal that HR increased as SBP and DBP increased.

5.2. PTT and PWV. PTT is generally defined as the time interval between the pulse wave in the aorta and the peripheral arteries, which is the peak time difference measured by two sensors simultaneously. PWV refers to the transit rate, which is calculated by dividing the distance between the two sensors by PTT. Both PTT and PWV have a strong correlation with the degree of arterial stiffness and blood pressure. Moreover, these methods have been clinically verified by medical scientists, and they have been used in medical diagnosis. Relevant studies have noted that blood pressure and PTT are inversely proportional; that is, blood pressure increases when PTT decreases [34]. Table 5 presents data on the relationship between PTT, PWV, SBP, and DBP in the 10 participants, as measured in the aforementioned experiment. As SBP and DBP increased, PTT decreased, otherwise PWV increased.

5.3. PWA. PWA involves PPG pulse wave analysis, which mainly retrieves all the SBP and DBP data from the PPG waveform. Some studies have analyzed related characteristic parameters, but this method mostly relies on the completeness and correctness of the waveform, which represents a challenge for real-time measurement [35]. Therefore, this experiment first used the sensor hardware to perform preliminary filtering. Subsequently, the peak and trough values of the two PPGs and the AM of the dual PPG during the measurement were extracted under a stable waveform, which represented the blood pressure-related characteristics with stable and obvious change on the PPG waveform. Table 6 presents data on the relationship between PWA, SBP, and DBP of the 10 participants measured in the aforementioned experiment. The data reveal that PWA increased as SBP and DBP increased.

5.4. PI. PI represents the change in blood volume, which can be used to predict the change in stroke volume caused by blood arterial circulation. PI refers to the ratio of pulsatile flow to nonpulsatile blood, which is also one of the essential indicators for judging the condition of blood vessels [36]. Table 7 lists data on the relationship between PI, SBP, and DBP in the 10 participants measured in the aforementioned experiment. The data reveal that PI increased as SBP and DBP increased.

6. Experimental Results and Discussion

The current experiment involved 100 participants. Three experimental samples were extracted from each participant, and each sample had 10 eigenvalues; thus, 300 samples were used for training the BPNN model. The 10 eigenvalues collected from the dual PPG measurement, HR, PTT, PWV, peak and trough values of dual PPGs, AM of the dual PPG during measurement, and PI were input into the BPNN for training. The results revealed that after 80,000 iterations, the error trend stabilized; the convergence curve is illustrated

in Figure 16. After comparing the estimated and actual SBP and DBP, the error (mean and standard deviation) between the estimated and the actual SBP was 2.23 ± 2.24 mmHg, the mean squared error was 3.15 mmHg, and the mean accuracy was 98.22%. Moreover, the error between the estimated and the actual DBP was 3.5 ± 3.53 mmHg, the mean squared error was 4.96 mmHg, and the mean accuracy was 95.58%. The p values calculated using the independent sample t -test were 0.570992122 and 0.158303407, respectively, and both were greater than 0.05. Figures 17 and 18 reveal the scatter plots of the SBP and DBP estimated by the BPNN and the actual SBP and DBP measured by the Omron standard instrument.

7. Conclusions

The blood pressure measurement method proposed in this study used dual PPG sensors, which were placed on the same artery branch to simultaneously capture pulses from fingers. The signals from both sensors were synchronized, and the waveforms were recorded in real time. Moreover, cardiovascular disease-related indicators such as the peak and trough values of PPG pulse, HR, PI, PTT, and PWV were used in the BPNN algorithm to estimate the SBP and DBP. The BPNN was designed with robust experimental data and integrated with blood pressure-related indicators; this enabled the researchers to effectively train the model and complete the continuous blood pressure measurement system. Moreover, to increase the robustness of the model, this study input data of 100 Asian participants (including those with and without cardiovascular disease, each with a proportion of approximately 50%) into the BPNN training database. The designed system only requires 10 eigenvalues to instantly output blood pressure values. In the proposed real-time blood pressure measurement system, the mean accuracy of SBP and DBP was 98.22% and 95.58%, respectively.

Data Availability

Our experiment data restrict by computer-processed personal data protection law in Taiwan.

Conflicts of Interest

The authors declare that they have no conflicts of interest.

Acknowledgments

This study was supported in part by the Ministry of Science and Technology MOST 108-2221-E-150-022-MY3.

References

- [1] A. B. Hertzman and C. R. Spielman, "Observations on the finger volume pulse recorded photoelectrically," *The American Journal of Physiology*, vol. 119, pp. 334-335, 1937.
- [2] A. C. Burton, "The range and variability of the blood flow in the human fingers and the vasomotor regulation by body temperature," *American Physiological Society*, vol. 127, pp. 437-453, 1939.

- [3] Y. Mendelson and B. D. Ochs, "Noninvasive pulse oximetry utilizing skin reflectance photoplethysmography," *IEEE Transactions on Biomedical Engineering*, vol. 35, no. 10, pp. 798–805, 1988.
- [4] M. Nitzan, H. de Boer, S. Turivnenko, A. Babchenko, and D. Sapoznikov, "Power spectrum analysis of spontaneous fluctuations in the photoplethysmographic signal," *Journal of basic and clinical physiology and pharmacology*, vol. 5, no. 3–4, pp. 269–276, 1994.
- [5] M. Marek, J. Thomas Bigger, A. John Camm et al., "Heart rate variability: standards of measurement, physiological interpretation, and clinical use," *European Heart Journal*, vol. 17, no. 3, pp. 354–381, 1996.
- [6] K. Nakajima, T. Tamura, and H. Miike, "Monitoring of heart and respiratory rates by photoplethysmography using a digital filtering technique," *Medical Engineering & Physics*, vol. 18, no. 5, pp. 365–372, 1996.
- [7] S. Rhee, B.-H. Yang, and H. H. Asada, "Artifact-resistant power-efficient design of finger-ring plethysmographic sensors," *IEEE Transactions on Biomedical Engineering*, vol. 48, no. 7, pp. 795–805, 2001.
- [8] K. W. Chan, K. Hung, and Y. T. Zhang, "Noninvasive and cuffless measurements of blood pressure for telemedicine," in *2001 Conference Proceedings of the 23rd Annual International Conference of the IEEE Engineering in Medicine and Biology Society*, vol. 4, pp. 3592–3593, Istanbul, Turkey, 2001.
- [9] V. S. Murthy, S. Ramamoorthy, N. Srinivasan, S. Rajagopal, and M. M. Rao, "Analysis of photoplethysmographic signals of cardiovascular patients," in *2001 Conference Proceedings of the 23rd Annual International Conference of the IEEE Engineering in Medicine and Biology Society*, vol. 3, pp. 2204–2207, Istanbul, Turkey, 2001.
- [10] Y. Y. Gu, Y. Zhang, and Y. T. Zhang, "A novel biometric approach in human verification by photoplethysmographic signals," in *4th International IEEE EMBS Special Topic Conference on Information Technology Applications in Biomedicine*, pp. 13–14, Birmingham, UK, 2003.
- [11] J. Liu, Y. Zhang, X. Ding, W. Dai, and N. Zhao, "A preliminary study on multi-wavelength PPG based pulse transit time detection for cuffless blood pressure measurement," in *2016 38th Annual International Conference of the IEEE Engineering in Medicine and Biology Society (EMBC)*, pp. 615–618, Orlando, FL, 2016.
- [12] H. Lui and K. Chow, "A novel calibration procedure of pulse transit time based blood pressure measurement with heart rate and respiratory rate," in *2018 40th Annual International Conference of the IEEE Engineering in Medicine and Biology Society (EMBC)*, pp. 4318–4322, Honolulu, HI, 2018.
- [13] D. Czerwinski, P. Wojcicki, and T. Zientarski, "On time blood pressure prediction with the use of PPG signals," in *2017 International Conference on Electromagnetic Devices and Processes in Environment Protection with Seminar Applications of Superconductors (ELMECO & AoS)*, pp. 1–4, Lublin, 2017.
- [14] A. Savkar, P. Khatate, and C. Y. Patil, "Study on techniques involved in tourniqueteless blood pressure measurement using PPG," in *2018 Second International Conference on Intelligent Computing and Control Systems (ICICCS)*, pp. 170–172, Madurai, India, 2018.
- [15] R. Shriram, A. Wakankar, N. Daimiwal, and D. Ramdasi, "Continuous cuffless blood pressure monitoring based on PTT," in *2010 International Conference on Bioinformatics and Biomedical Technology*, pp. 51–55, Chengdu, 2010.
- [16] M. H. Pollak and P. A. Obrist, "Aortic-radial pulse transit time and ECG Q-wave to radial pulse wave interval as indices of beat-by-beat blood pressure change," *Psychophysiology*, vol. 20, no. 1, pp. 21–28, 1983.
- [17] L. A. Geddes, M. H. Voelz, C. F. Babbs, J. D. Bourland, and W. A. Tacker, "Pulse transit time as an indicator of arterial blood pressure," *Psychophysiology*, vol. 18, no. 1, pp. 71–74, 1981.
- [18] A. A. Robert, A. S. John, M. D. Dennis, A. W. Mark, and C. B. Taylor, "The covariation of blood pressure and pulse transit time in hypertensive patients," *Psychophysiology*, vol. 18, pp. 301–306, 1981.
- [19] G. V. Marie, C. R. Lo, J. Van Jones, and D. W. Johnston, "The relationship between arterial blood pressure and pulse transit time during dynamic and static exercise," *Psychophysiology*, vol. 21, no. 5, pp. 521–527, 1984.
- [20] J. Kerola, V. Kontra, and R. Sepponen, "Non-invasive blood pressure data acquisition employing pulse transit time detection," in *Proceedings of the 18th Annual International Conference of the IEEE Medicine and Biology Society*, vol. 3, pp. 1308–1309, Amsterdam, Netherlands, 1996.
- [21] K. Meigas, R. Kattai, and J. Lass, "Continuous blood pressure monitoring using pulse wave delay," in *Proceedings of the 23rd Annual International Conference of the IEEE Medicine and Biology Society*, vol. 4, pp. 3171–3174, Istanbul, Turkey, 2001.
- [22] A. Rasool, M. Rafiq, A. Nasir, and F. M. Kashif, "Continuous and noninvasive blood pressure estimation by two-sensor measurement of pulse transit time," in *2018 14th International Conference on Emerging Technologies (ICET)*, pp. 1–5, Islamabad, 2018.
- [23] W. Lin, H. Wang, O. W. Samuel, and G. Li, "Using a new PPG indicator to increase the accuracy of PTT-based continuous cuffless blood pressure estimation," in *2017 39th Annual International Conference of the IEEE Engineering in Medicine and Biology Society (EMBC)*, pp. 738–741, Seogwipo, 2017.
- [24] R. Nye, Z. Zhang, and Q. Fang, "Continuous non-invasive blood pressure monitoring using photoplethysmography: a review," in *2015 International Symposium on Bioelectronics and Bioinformatics (ISBB)*, pp. 176–179, Beijing, 2015.
- [25] L. Peter, N. Noury, and M. Cerny, "A review of methods for non-invasive and continuous blood pressure monitoring: Pulse transit time method is promising?," *Irbm*, vol. 35, no. 5, pp. 271–282, 2014.
- [26] D. B. McCombie, A. T. Reisner, and H. H. Asada, "Adaptive blood pressure estimation from wearable PPG sensors using peripheral artery pulse wave velocity measurements and multichannel blind identification of local arterial dynamics," in *Annual International Conference of the IEEE Engineering in Medicine and Biology-Proceedings*, pp. 3521–3524, New York, NY, USA, 2006.
- [27] R. Samria, R. Jain, A. Jha, S. Saini, and S. R. Chowdhury, "Non-invasive cuffless estimation of blood pressure using photoplethysmography without electrocardiograph measurement," in *IEEE TENSYP 2014 –2014 IEEE Region 10 Symposium*, pp. 254–257, Kuala Lumpur, Malaysia, 2014.
- [28] G. Joseph, A. Joseph, G. Titus, R. M. Thomas, and D. Jose, "Photoplethysmogram (PPG) signal analysis and wavelet de-noising," in *2014 Annual International Conference on Emerging Research Areas: Magnetics, Machines and Drives (AICERA/iCMMD)*, pp. 1–5, Kottayam, 2014.
- [29] C. Fischer, B. Dömer, T. Wibmer, and T. Penzel, "An algorithm for real-time pulse waveform segmentation and artifact

- detection in photoplethysmograms,” *IEEE Journal of Biomedical and Health Informatics*, vol. 21, no. 2, pp. 372–381, 2017.
- [30] Y. Zhang and Z. Wang, “A hybrid model for blood pressure prediction from a PPG signal based on MIV and GA-BP neural network,” in *2017 13th International Conference on Natural Computation, Fuzzy Systems and Knowledge Discovery (ICNC-FSKD)*, pp. 1989–1993, Guilin, 2017.
- [31] P. Boutouyrie, M. Briet, C. Collin, S. Vermeersch, and B. Pannier, “Assessment of pulse wave velocity,” *Artery Research*, vol. 3, pp. 3–8, 2009.
- [32] W. Mower, G. Myers, E. Nicklin, K. Kearin, L. Baraff, and C. Sachs, “Pulse oximetry as a fifth vital sign in emergency geriatric assessment,” *Academic Emergency Medicine*, vol. 5, no. 9, pp. 858–865, 1998.
- [33] G. A. Lanza, V. Guido, M. M. Galeazzi et al., “Prognostic role of heart rate variability in patients with a recent acute myocardial infarction,” *The American Journal of Cardiology*, vol. 82, no. 11, pp. 1323–1328, 1998.
- [34] B. Mishra and N. Thakkar, “Cuffless blood pressure monitoring using PTT and PWV methods,” in *2017 International Conference on Recent Innovations in Signal processing and Embedded Systems (RISE)*, pp. 395–401, Bhopal, 2017.
- [35] Y. Kurylyak, F. Lamonaca, and D. Grimaldi, “A neural network-based method for continuous blood pressure estimation from a PPG signal,” in *2013 IEEE International Instrumentation and Measurement Technology Conference (I2MTC)*, pp. 280–283, Minneapolis, MN, 2013.
- [36] T. Y. Abay and P. A. Kyriacou, “Reflectance photoplethysmography as noninvasive monitoring of tissue blood perfusion,” *IEEE Transactions on Biomedical Engineering*, vol. 62, no. 9, pp. 2187–2195, 2015.

Research Article

Characteristics of Metal–Semiconductor–Metal Ultraviolet Photodetectors Based on Pure ZnO/Amorphous IGZO Thin-Film Structures

Kin-Tak Lam,¹ Sheng-Joue Young²,³ Yen-Lin Chu³,⁴ Chi-Nan Tsai,³ Tung-Te Chu,⁴ Ting-Sung Lu,³ and Liang-Wen Ji³

¹Fujian University of Technology, Fuzhou, Fujian 350108, China

²Department of Electronic Engineering, National United University, Miaoli City 36063, Taiwan

³Department of Electro-Optical Engineering & Institute of Electro-Optical and Materials Science, National Formosa University, Yunlin 632, Taiwan

⁴Department of Mechanical Automation Engineering, Kao Yuan University, Kaohsiung 821, Taiwan

Correspondence should be addressed to Sheng-Joue Young; youngsj@nuu.edu.tw, Yen-Lin Chu; 10576123@gm.nfu.edu.tw, and Liang-Wen Ji; lwji@nfu.edu.tw

Received 14 December 2020; Revised 15 January 2021; Accepted 31 March 2021; Published 12 April 2021

Academic Editor: Stefano Bellucci

Copyright © 2021 Kin-Tak Lam et al. This is an open access article distributed under the Creative Commons Attribution License, which permits unrestricted use, distribution, and reproduction in any medium, provided the original work is properly cited.

In this study, metal–semiconductor–metal-structured ultraviolet (UV) photodetectors (PDs) based on pure zinc oxide (ZnO) and amorphous indium gallium zinc oxide (a-IGZO) thin films were fabricated and characterized. The ZnO seed layers were deposited on Corning glass substrates via a radio frequency (RF) magnetron sputtering technique. Results showed that under a 5 V applied bias; the dark currents of the pure ZnO and a-IGZO thin films were 0.112 pA and 2.85 nA, respectively. Meanwhile, the UV-to-visible rejection ratio of the pure ZnO and a-IGZO thin films were 14.33 and 256, respectively. Lastly, the PDs of the a-IGZO thin films had a lower leakage current and higher rejection ratio than that of the pure ZnO thin films from the UV to visible light region.

1. Introduction

In recent years, ultraviolet (UV) photodetectors (PDs) have played an important role in human health, ozone layer monitoring, and flame detection [1, 2]. Zinc oxide (ZnO) is a novel metal oxide semiconductor material that is used as an integral part of UV PDs [3, 4]. ZnO is an *n*-type and II-VI material; its bandgap is approximately 3.37 eV, and its excitation binding energy is 60 meV at room temperature [5, 6]. ZnO is a good crystallinity material. It has a hexagonal structure, and the lattice constants are $a = 3.24 - 3.26 \text{ \AA}$ and $c = 5.13 - 5.43 \text{ \AA}$ [7–9]. In addition, the lowest surface free energy of ZnO thin films lies on the (002) plane, and a good *c*-axis orientation can be obtained at a low temperature when ZnO thin films are grown. In addition to having good carrier

mobility and photoelectric properties, crystalline metal oxide semiconductors are amorphous oxide semiconductor materials and thus have attracted considerable attention; moreover, the inclusion of ZnO compounds has led to extensive research. The type of material consists of various transition metals and oxygen atoms, such as zinc tin oxide (ZnSnO) [10], indium zinc oxide (InZnO) [11], and indium gallium zinc oxide (InGaZnO) [12], to enhance overall carrier mobility and photoelectric properties. Among them, the InGaZnO (IGZO) is a ternary oxide semiconductor. Its composition includes In_2O_3 , Ga_2O_3 , and ZnO. Amorphous IGZO oxide semiconductors have high carrier mobility, good uniformity, and wide energy bandgap, which offers good transparency in the visible spectrum; its peculiar chemical bonding instigates high field mobility and displays

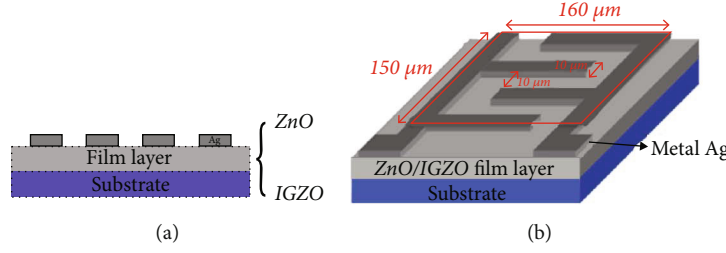


FIGURE 1: (Color online) (a) Side- and (b) top-view images of the IDT electrode.

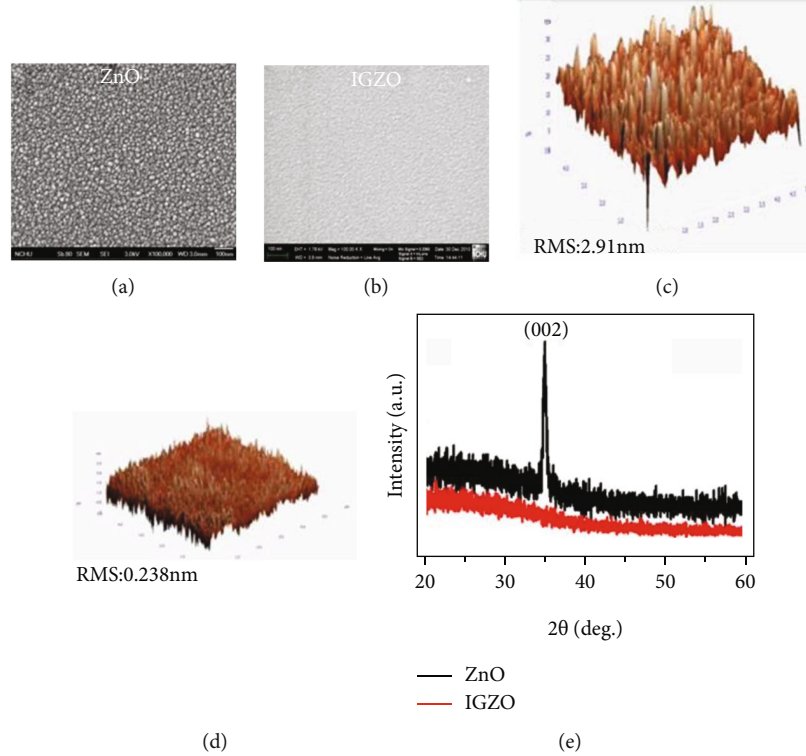


FIGURE 2: (a, b) SEM images of pure ZnO and a-IGZO thin films. (c, d) AFM images of 40 nm pure ZnO and 40 nm a-IGZO thin films. (e) XRD spectra of pure ZnO and a-IGZO thin films.

improved electrical characteristics, such as high I_{ON}/I_{OFF} ratio, enhanced lifetime, improved transmittance, and optimum large-area uniform integration [13–15]. The characteristics of transparency can be applied to the optical field.

In this study, the difference between crystalline ZnO thin-film PDs and amorphous IGZO thin-film PDs is discussed.

2. Experimental

Before UV PDs were manufactured, 1 cm × 1 cm Corning glass substrates were, respectively, cleaned for 10 min with acetone, isopropyl alcohol, and deionized water in an ultrasonic cleaner. Afterward, they were dried with flowing nitrogen and then placed in an oven for approximately 10 min at 45°C. Three-inch-diameter targets of pure ZnO and a-IGZO (atomic ratio In:Ga:Zn = 1:1:1) with a purity of 99.99% were used. The pure ZnO and a-IGZO thin films were grown using the radio frequency magnetron sputtering

technique under a sputtering power of 100 W, a gas mixing ratio of Ar/O₂ (10/1), and a maintained chamber pressure at 5×10^{-2} Torr. The thickness was approximately 40 nm. Afterward, the film was annealed in a vacuum furnace at 450°C for 1 h to improve crystal quality. The resistivity of the pure ZnO thin films was $\sim 10^{-5}$ (ohm-cm), and that of the a-IGZO thin films is approximately 1×10^{-3} (ohm-cm). The surface morphology, surface roughness, and crystallographic of the pure ZnO and a-IGZO thin films were characterized and explored by field-emission scanning electron microscopy (FE-SEM, JEOL JSM-6700F), atomic force microscopy (AFM, NT-MDT), and X-ray diffraction spectrum analysis with Cu K α -1 radiation and $\lambda = 0.15405$ nm (XRD, MO3XHF22 MAC-Science), respectively. The optical characteristic was measured using a UV/visible spectrometer (UV-VIS, Hitachi U-2800).

In part of devices, the standard photolithography and lift-off were then performed to define the interdigitated (IDT)

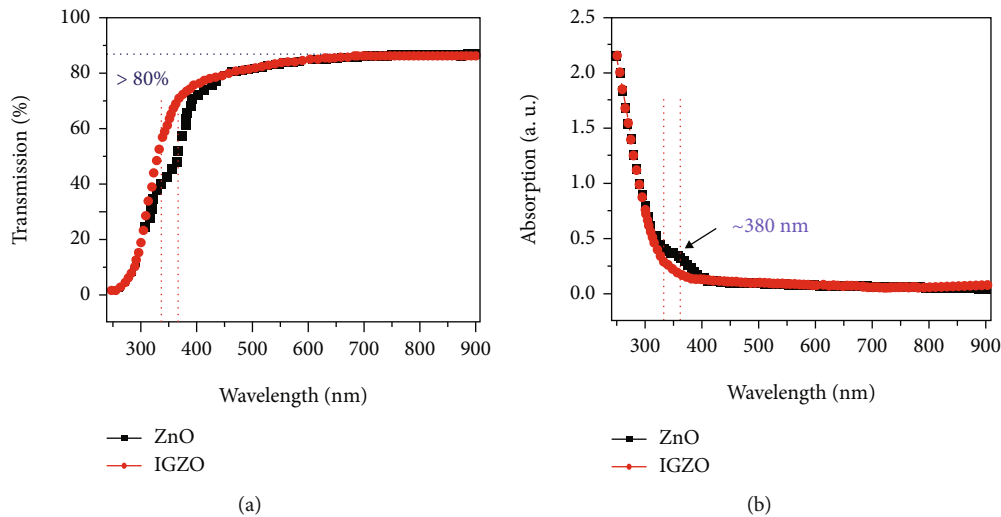


FIGURE 3: (a, b) Transmittance and UV-VIS spectra of pure ZnO and a-IGZO thin films.

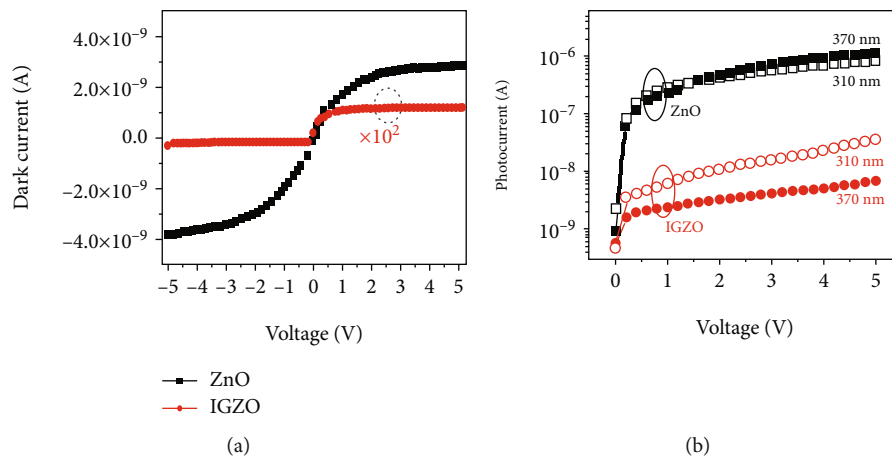


FIGURE 4: (a) Dark current–voltage (I – V) characteristics of the pure ZnO and a-IGZO thin films for UV PDs. (b) Photocurrent of pure ZnO and a-IGZO thin films at a wavelength 310 and 370 nm.

mask region. The IDT electrode measured 146, 10, and 10 μm in length, width, and space, respectively. The sensing active region was 150 $\mu\text{m} \times 160 \mu\text{m}$. Subsequently, the silver (Ag) electrode was deposited by e-gun evaporation and used as contact electrode to form a metal–semiconductor–metal (MSM) structure, as shown in Figures 1(a) and 1(b). The light and dark currents of MSM UV PDs were measured by a semiconductor parameter analyzer (Agilent HP 4156C) system. The photoresponse was measured by a light source, i.e., a 300 W Xe lamp and a monochromator, from a 300–600 nm range. In this work, two MSM UV PD devices were fabricated to identify which is better.

3. Results and Discussion

Figures 2(a) and 2(b) show the surface morphology of pure ZnO and a-IGZO thin films by FE-SEM analysis and clearly indicate the difference between the surfaces of pure ZnO and a-IGZO. The pure ZnO film underwent grain formation, whereas the a-IGZO film did not. According to the AFM

TABLE 1: Dark current and photocurrent of the pure ZnO and a-IGZO thin films for UV PDs at 310 and 370 nm wavelengths.

Current (A)	Pure ZnO	a-IGZO
I_{dark}	2.85 nA	0.112 pA
$I_{\text{ph}(310 \text{ nm})}$	0.82 μA	36.3 nA
$I_{\text{ph}(370 \text{ nm})}$	1.1 μA	6.6 nA
$I_{\text{ph}(\text{ZnO})}/I_{\text{dark}(\text{ZnO})(370 \text{ nm})}$	385.9	
$I_{\text{ph}(\text{IGZO})}/I_{\text{dark}(\text{IGZO})(370 \text{ nm})}$	589.2	
$I_{\text{ph}(\text{ZnO})}/I_{\text{ph}(\text{IGZO})(310 \text{ nm})}$	22.53	
$I_{\text{ph}(\text{ZnO})}/I_{\text{ph}(\text{IGZO})(370 \text{ nm})}$	166.6	

images shown in Figures 2(c) and 2(d), the surface roughness RMS value of the ZnO film was 2.91 nm, and that of the a-IGZO film was 0.238 nm, indicating that the overall surface of the pure ZnO film was rougher than the a-IGZO film because of grain formation. Figure 2(e) depicts the typical

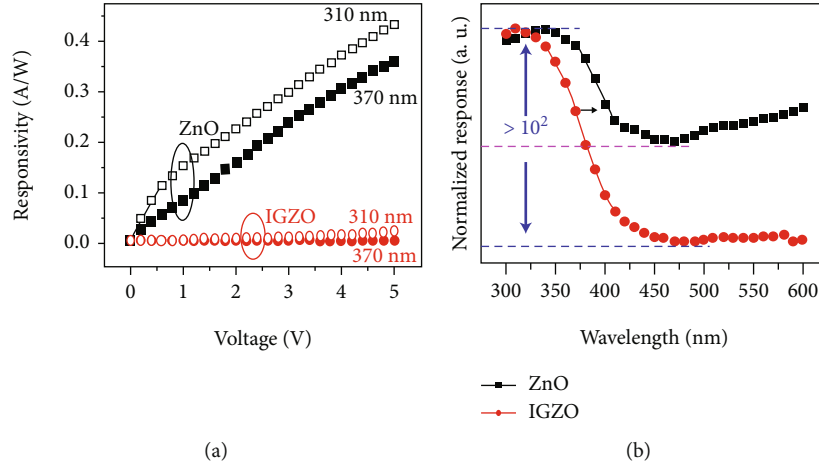


FIGURE 5: (a) Current responsivities of pure ZnO and a-IGZO thin films under different bias voltages. (b) Photoresponsivities of pure ZnO and a-IGZO thin films based on UV PDs at different wavelengths.

XRD results of the pure ZnO NRs and a-IGZO thin films that were prepared on the Corning glass substrate. The results indicated that the diffraction peak corresponded with the (002) planes. The peak revealed the hexagonal wurtzite structure of ZnO (JCPDS Card No. 36-1451) [16]. On the contrary, IGZO films showed amorphous phenomena [17].

Figures 3(a) and 3(b) show the spectrum of transmission and absorption of pure ZnO and a-IGZO thin films. Both had the same thickness of thin films, and the transmission could reach approximately 80% in the visible wavelength [18, 19]. However, the main difference was that the pure ZnO thin films slightly decayed in the 300–400 nm wavelengths. In the absorption spectrum, the absorption of the a-IGZO thin films was deeper than that of the pure ZnO thin films.

The measurements of the current–voltage (I–V) characteristics in pure ZnO and a-IGZO in the absence of light are shown in Figure 4(a). The dark current of the pure ZnO films was larger than that of the a-IGZO thin films because the a-IGZO thin films were amorphous. Therefore, in the a-IGZO thin films, the transmission path of relative current decreased, and the dark current would become relatively small under no effect by grain boundaries [20–22]. In the red parts of the figure, they are magnified to 10² times; the dark current was 0.112 pA under a 5 V applied bias. The black parts show the pure ZnO thin films; the dark current was 2.85 nA under a 5 V bias voltage. Similarly, the dark current of the former was larger than the latter by 256 times. Meanwhile, the pure ZnO thin films were in the (002) lattice direction. Therefore, the dark current would be evident under the transmission path of grain boundaries, indicating that the dark current would be restrained by an amorphous morphology. It was photocurrent in Figure 4(b). In the pure ZnO thin films, it was transferred in grain boundaries. Therefore, the dark current and the photocurrent became larger. As shown in Table 1, the semiconductor photocurrent I_{ph} is expressed as follows [23]:

$$I_{ph} = q\eta A\Phi_{ph}G \quad (1)$$

TABLE 2: Photoresponsivities of the pure ZnO and a-IGZO thin films for UV PDs.

Responsivity (R)	Pure ZnO/a-IGZO
$R_{310\text{ nm}(\text{ZnO})}/R_{370\text{ nm}(\text{ZnO})}$	1.22
$R_{310\text{ nm}(\text{IGZO})}/R_{370\text{ nm}(\text{IGZO})}$	10
$R_{310\text{ nm}(\text{ZnO})}/R_{450\text{ nm}(\text{ZnO})}$	14.33
$R_{310\text{ nm}(\text{IGZO})}/R_{450\text{ nm}(\text{IGZO})}$	256

where q is the electronic charge, η is the quantum efficiency, A is the active area, Φ_{ph} is the photon flux, and G is the photoconductive gain. The ratio of light current to dark current I_{ph}/I_{dark} was 589.2 in a-IGZO and 385.9 in pure ZnO; the former was larger than the latter. In addition, the photocurrent of the pure ZnO films was larger than the a-IGZO thin films, that is, approximately 166.6 times of $I_{ph(\text{ZnO})}/I_{ph(\text{IGZO})}$.

Figure 5(a) shows the current response value of pure ZnO and a-IGZO thin films at 310 and 370 nm wavelengths under a bias voltage of 0–5 V. Figure 5(b) shows the main photoresponsivity of parameter values in PDs. The UV-to-visible rejection ratio of a-IGZO PD was two orders more than that of pure ZnOPD from UV light to visible light, because the a-IGZO thin films were amorphous. This result indicates that the dark current and photocurrent would be restrained by an amorphous morphology, thus affecting the entire response. As shown in Table 2, the responsivity (R) of a PD is defined as follows [24, 25]:

$$R = (I_{light} - I_{dark})/P_{opt} = I_{ph}/P_{opt}, \quad (2)$$

where I_{dark} is the dark current, I_{light} is the photocurrent, and P_{opt} is the incident optical power. The UV-to-visible rejection ratio of a-IGZO PD ($[R_{310\text{ nm}(\text{IGZO})}/R_{450\text{ nm}(\text{IGZO})}] = 256$)

was larger than that of pure ZnOPD ($[R_{310\text{nm}}(\text{ZnO})/R_{450\text{nm}}(\text{ZnO})] = 14.33$); in addition, the absorbance of UV light in the a-IGZO was deeper at a 310 nm wavelength.

4. Conclusion

The MSM structure of UVPDs based on pure ZnO and a-IGZO thin films was fabricated and characterized. Results showed that the dark currents of the pure ZnO and a-IGZO thin films were 0.112 pA and 2.85 nA, respectively, under a 5 V applied bias. Meanwhile, the UV-to-visible rejection ratios of the pure ZnO and a-IGZO thin film were 14.33 and 256, respectively. In the pure ZnO thin films, the dark current was evident under the transmission path of grain boundaries. Therefore, the dark current and photocurrent became larger. This result indicated that the dark current could be restrained by an amorphous morphology. Lastly, the PDs of the a-IGZO thin films had a lower leakage current and higher rejection ratio than that of the pure ZnO thin films from the UV to visible light region. In the future technology, the UV PDs can be combined with the Internet of Things and applied it to human skin to avoid skin aging and skin cancer.

Data Availability

All the data results in our article, we can provide them if requested.

Conflicts of Interest

The authors declare there are no competing interests.

Authors' Contributions

Yen-Lin Chu and Chi-Nan Tsai performed the experiments; Kin-Tak Lam, Sheng-Joue Young, and Liang-Wen Ji conceived the experiments; Tung-Te Chu and Ting-SungLu participated in data analysis.

Acknowledgments

This work was financially supported by the Ministry of Science and Technology of Taiwan (Project numbers MOST 107-2221-E-150-032, MOST 108-2221-E-024-006, MOST 108-2221-E-150-013-MY2, MOST109-2221-E-239-031-MY2, and MOST 106-2221-E-239-037-MY3). The authors would like to thank the Common Laboratory for Micro/Nano Science and Technology of the National Formosa University for the use of their measurement equipment and their assistance in this work; the Center for Micro/NanoScience and Technology, National Cheng Kung University, for device characterization; and C. N. Tsai for device fabrication and equipment support.

References

- [1] M. Liao and Y. Koide, "High-performance metal-semiconductor-metal deep-ultraviolet photodetectors based on homoepitaxial diamond thin film," *Applied Physics Letters*, vol. 89, no. 11, article 113509, 2006.
- [2] M. Razeghi and A. Rogalski, "Semiconductor ultraviolet detectors," *Journal of Applied Physics*, vol. 79, no. 10, pp. 7433–7473, 1996.
- [3] Y.-L. Chu, S.-J. Young, R.-J. Ding, T.-T. Chu, T.-S. Lu, and L.-W. Ji, "Improving ZnO nanorod humidity sensors with Pt nanoparticle adsorption," *ECS Journal of Solid State Science and Technology*, vol. 10, no. 3, article 037003, 2021.
- [4] Y. L. Chu, L. W. Ji, H. Y. Lu et al., "Fabrication and characterization of UV photodetectors with Cu-doped ZnO nanorod arrays," *Journal of The Electrochemical Society*, vol. 167, no. 2, article 027522, 2020.
- [5] Y. L. Chu, S. J. Young, L. W. Ji, T. T. Chu, and C. H. Wu, "UV-enhanced field-emission performances of Pd-adsorbed ZnO nanorods through photochemical synthesis," *ECS Journal of Solid State Science and Technology*, vol. 10, no. 1, article 017001, 2021.
- [6] Y.-L. Chu, S.-J. Young, L.-W. Ji et al., "Characteristics of gas sensors based on co-doped ZnO nanorod arrays," *Journal of The Electrochemical Society*, vol. 167, no. 11, article 117503, 2020.
- [7] Y. L. Chu, S. J. Young, L. W. Ji, I. T. Tang, and T. T. Chu, "Fabrication of ultraviolet photodetectors based on Fe-doped ZnO nanorod structures," *Sensors*, vol. 20, no. 14, p. 3861, 2020.
- [8] Y. L. Chu, S. J. Young, L. W. Ji, T. T. Chu, and P. H. Chen, "Synthesis of Ni-doped ZnO nanorod arrays by chemical bath deposition and their application to nanogenerators," *Energies*, vol. 13, no. 11, p. 2731, 2020.
- [9] Y. L. Chu, L. W. Ji, Y. J. Hsiao et al., "Fabrication and characterization of Ni-doped ZnO nanorod arrays for UV photodetector application," *Journal of The Electrochemical Society*, vol. 167, no. 6, article 067506, 2020.
- [10] L. Feng, G. Yu, X. Li, J. Zhang, Z. Ye, and J. Lu, "Solution processed amorphous ZnSnO thin-film phototransistors," *IEEE Transactions on Electron Devices*, vol. 64, no. 1, pp. 206–210, 2017.
- [11] S. Sugumaran, M. N. B. Ahmad, M. F. Jamlos et al., "Transparent with wide band gap InZnO nano thin film: preparation and characterizations," *Optical Materials*, vol. 49, pp. 348–356, 2015.
- [12] H. C. Wu and C. H. Chien, "Highly Transparent, high-performance IGZO-TFTs using the selective formation of IGZO source and drain electrodes," *IEEE Electron Device Letters*, vol. 35, no. 6, pp. 645–647, 2014.
- [13] K. Nomura, H. Ohta, A. Takagi, T. Kamiya, M. Hirano, and H. Hosono, "Room-temperature fabrication of transparent flexible thin-film transistors using amorphous oxide semiconductors," *Nature*, vol. 432, no. 7016, pp. 488–492, 2004.
- [14] J. Jeong, G. J. Lee, J. Kim, and B. Choi, "Electrical characterization of a-InGaZnO thin-film transistors with Cu source/drain electrodes," *Applied Physics Letters*, vol. 100, no. 11, article 112109, 2012.
- [15] E. Fortunato, P. Barquinha, and R. Martins, "Oxide semiconductor thin-film transistors: a review of recent advances," *Advanced Materials*, vol. 24, no. 22, pp. 2945–2986, 2012.
- [16] M. Suche, S. Christoulakis, M. Katharakis, N. Katsarakis, and G. Kiriakidis, "Surface characterization of ZnO transparent thin films," *Journal of Physics: Conference Series*, vol. 10, pp. 147–150, 2005.

- [17] C. M. Hsu, W. C. Tzou, C. F. Yang, and Y. J. Liou, "Investigation of the high mobility IGZO thin films by using co-sputtering method," *Materials*, vol. 8, no. 5, pp. 2769–2781, 2015.
- [18] Y. Zhang, L.-X. Qian, Z. Wu, and X. Liu, "Amorphous InGaMgO ultraviolet photo-TFT with ultrahigh photosensitivity and extremely large responsivity," *Materials*, vol. 10, no. 2, p. 168, 2017.
- [19] A. F. A. Razak, S. Devadason, C. Sanjeeviraja, and V. Swaminathan, "Effect of annealing on structural and optical properties of ZnO thin films by sol gel technique," *Chalcogenide Letters*, vol. 8, pp. 511–519, 2011.
- [20] K. Nomura, A. Takagi, T. Kamiya, H. Ohta, M. Hirano, and H. Hosono, "Amorphous oxide semiconductors for high-performance flexible thin-film transistors," *Japanese Journal of Applied Physics*, vol. 45, no. 5B, pp. 4303–4308, 2006.
- [21] H. Arora, P. E. Malinowski, A. Chasin et al., "Amorphous indium-gallium-zinc-oxide as electron transport layer in organic photodetectors," *Applied Physics Letters*, vol. 106, no. 14, article 143301, 2015.
- [22] G. Wakimura, Y. Yamauchi, and Y. Kamakura, "Simulation and modeling of off-leakage current in InGaZnO thin-film transistors," *Journal of Advanced Simulation in Science and Engineering*, vol. 2, no. 1, pp. 201–210, 2015.
- [23] S.-M. Peng, Y.-K. Su, L.-W. Ji et al., "Transparent ZnO nanowire-network ultraviolet photosensor," *IEEE Transactions on Electron Devices*, vol. 58, no. 7, pp. 2036–2040, 2011.
- [24] Z.-H. Wang, H.-C. Yu, C.-C. Yang, H.-T. Yeh, and Y.-K. Su, "Low-frequency noise performance of Al-doped ZnO nanorod photosensors by a low-temperature hydrothermal method," *IEEE Transactions on Electron Devices*, vol. 64, no. 8, pp. 3206–3212, 2017.
- [25] W. S. Shih, S. J. Young, L. W. Ji, W. Water, T. H. Meen, and H. W. Shiu, "Effect of oxygen plasma treatment on characteristics of TiO_2 photodetectors," *IEEE Sensors Journal*, vol. 11, no. 11, pp. 3031–3035, 2011.

Research Article

Development of Detection Equipment for a Polymerase Chain Reaction with a Loop-Mediated Isothermal Amplification Reaction

Wei-Chien Weng  and Yu-Cheng Lin 

Department of Engineering Science, National Cheng Kung University, Tainan, Taiwan

Correspondence should be addressed to Yu-Cheng Lin; yuclin@mail.ncku.edu.tw

Received 6 January 2021; Revised 3 March 2021; Accepted 17 March 2021; Published 30 March 2021

Academic Editor: Sheng-Joue Young

Copyright © 2021 Wei-Chien Weng and Yu-Cheng Lin. This is an open access article distributed under the Creative Commons Attribution License, which permits unrestricted use, distribution, and reproduction in any medium, provided the original work is properly cited.

In this research, low-cost detection equipment intended to carry out a polymerase chain reaction (PCR) through a loop-mediated isothermal amplification (LAMP) reaction is presented. We designed the internal structure with SolidWorks and AutoCAD. The equipment comprised a Raspberry Pi development board, a temperature control module, and a fluorescent optical detection module. The main program, temperature control, fluorescent signal processing, signal analysis, and screen display were programmed with Java. We applied the digital temperature controller module to obtain precise temperature control of the equipment. The experimental results showed that the heating rate of the testing equipment could reach 65°C within 4 minutes and could be accurately controlled to within 1°C. The duration of the LAMP PCR experiment was found to be significantly shorter than that of the conventional PCR. The results also revealed that with LAMP PCR, the temperature could be accurately controlled within a specific range, and the designed heating tasks could be completed within 15 minutes to one hour, depending on the specimen. The equipment could also correctly read both the positive and negative reactions with fluorescent signals. Thus, the proposed LAMP PCR detection equipment is more sensitive, more stable, and more cost-effective than other conventional alternatives and can be used in numerous clinical applications.

1. Introduction

The detection of many infectious diseases including tuberculosis, AIDS, bacterial and viral infections, genetic diseases, foodborne diseases, SARS, MERS, and COVID-19 mostly depends on a specific detection technique—a polymerase chain reaction (PCR). A PCR is a relatively simple, inexpensive tool that can be used to focus on a DNA segment in order to duplicate the specified segment many times [1–4]. Loop-mediated isothermal amplification (LAMP) PCR is a nucleic acid amplification technology developed by Japanese scientist Notomi and his team in 2000 [5, 6]. This DNA amplification method can react at a constant temperature and form a circular loop. Different from the conventional PCR, LAMP PCR does not require multistage temperature control. It only requires a constant temperature environment within a range

of 60–65°C, which can be provided by a water bath or a drying hot plate environment.

Because there are as many as three pairs of primers employed in LAMP PCR, its specificity and sensitivity are higher than ordinary PCRs. Furthermore, the number of molecules can be increased to 1E10 after LAMP PCR is completed and that quantity is even 1E4 times more than the quantity of 1E6 molecules generated by conventional PCR. Moreover, in the amplification process, the enzyme used in LAMP PCR will generate pyrophosphoric acid, which will then combine with magnesium ions and generate a large amount of white precipitate visible to the naked eye. Thus, there is no need to employ agarose gel electrophoresis and UV light to detect and interpret the analyte.

After pure DNA is extracted from an organism, the most common analytical method used to separate and

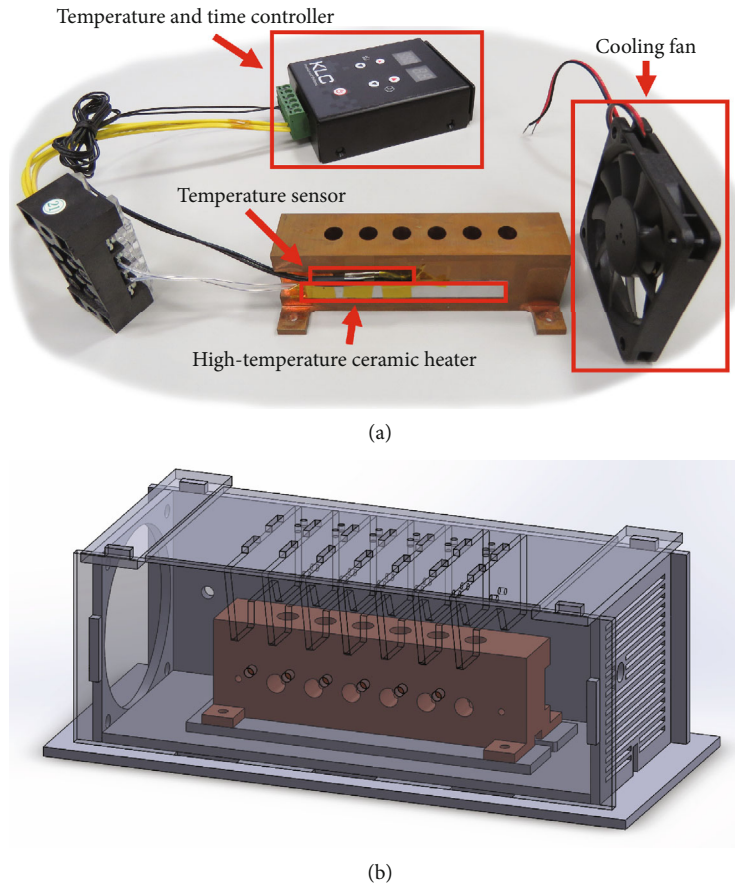


FIGURE 1: Temperature control: (a) exploded photo of the components of the temperature control system and (b) perspective of the combination of the optical detection subsystem, the copper block, and the optical detection dark box.

analyze macromolecules and their fragments based on their size and charge is a gel electrophoresis analysis. There are two types of gel electrophoresis commonly used to analyze DNA: agarose gel electrophoresis (AGE) and polyacrylamide gel electrophoresis (PAGE) [7].

PCR can also be used in many other ways, including for diagnosing diseases, identifying bacteria and viruses [8–12], and matching criminals with crime scenes. However, most PCR detection operations are time consuming, so developing more effective and faster LAMP PCR detection equipment is, thus, essential.

This research is aimed at developing LAMP PCR detection equipment intended to establish the proper temperature conditions for the reaction of detected specimens and to use a precise temperature control technology to shorten the reaction time for conventional PCR. After the reaction is completed, photoresistors are used to detect the fluorescent signals and the results are shown on a screen.

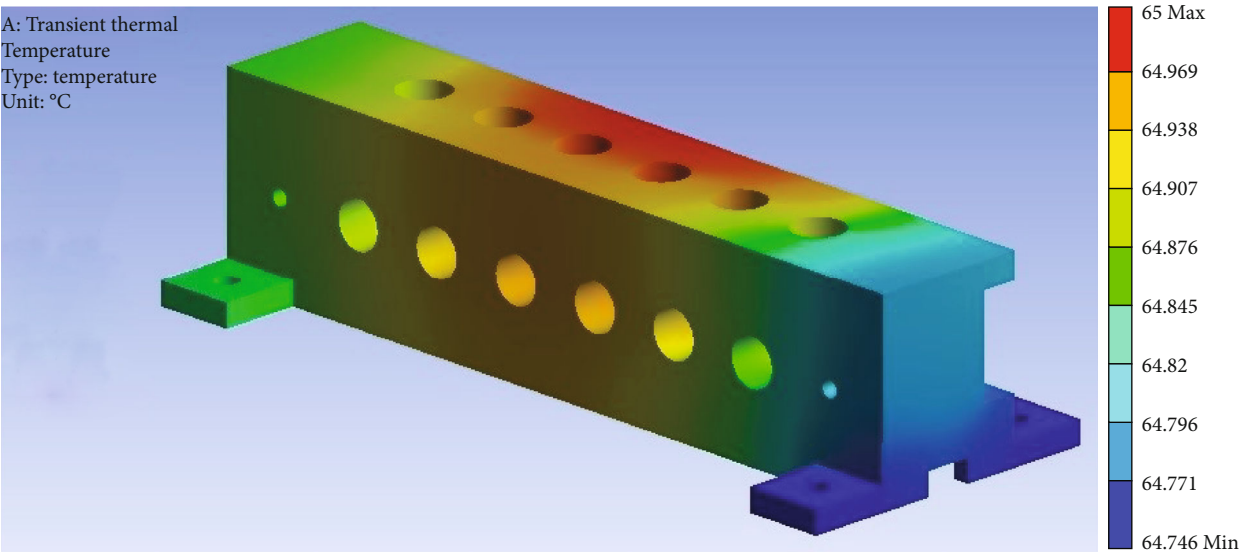
In 2000, Yasuda et al. applied infrared laser beams and noncontact heating methods to the PCR thermal cycle and successfully detected the results of PCR with fluorescence detection [13]. In 2009, Sappat et al. used a light-dependent resistor (LDR) to detect the white precipitate from magnesium pyrophosphate ($\text{Mg}_2\text{P}_2\text{O}_7$) produced by

the reverse transcription loop-mediated isothermal amplification (RT-LAMP) method for the detection of the Taura syndrome virus (TSV) in Thai shrimp [14]. In 2015, Zhou et al. used LAMP PCR for 15 different strains and then used three detection methods to verify them, including SYBR Green I fluorescence detection, colloidal electrophoresis analysis, and turbidity detection. Finally, it was verified that LAMP PCR is simpler, faster, and more sensitive than conventional PCR [15].

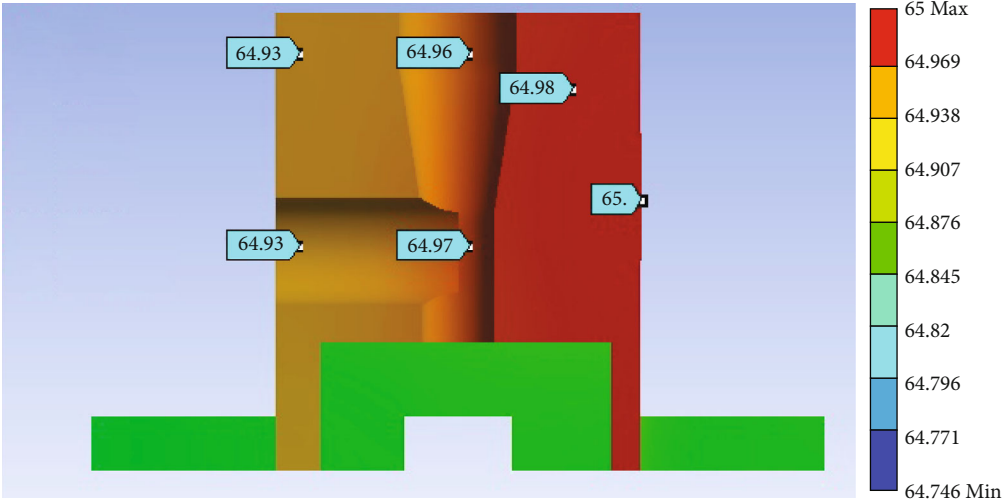
In March 2020, due to the SARS-CoV-2 (COVID-19) pandemic, Kashir and Yaqinuddin used LAMP PCR to reduce the cost of coronavirus detection. The results showed the sensitivity using LAMP assay to be 100-fold higher than that of conventional RT-PCR methods [16]. Furthermore, Rödel et al. used reverse transcription-LAMP (RT-LAMP) for rapid diagnosis of the severe acute respiratory syndrome Coronavirus-2 (SARS-CoV-2) because of the ease of operation and the option to bypass RNA extraction. Combining the RT-PCR and RT-LAMP increased the diagnostic sensitivity to 92–100% [17].

2. Materials and Methods

The LAMP PCR detection equipment developed in this work consisted of a Raspberry Pi small single-board



(a)



(b)

FIGURE 2: Simulation of the temperature distribution of the metal heating block: (a) overall temperature distribution and (b) a cross-sectional view of the temperature distribution.

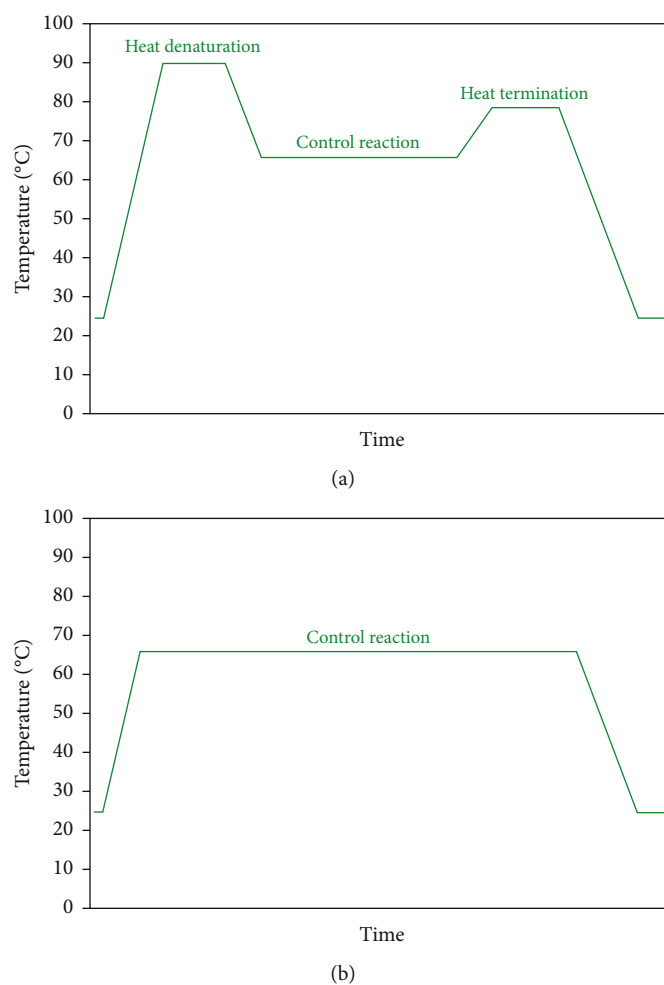


FIGURE 3: Illustration of the differences in heating control between LAMP PCR and traditional PCR, (a) Traditional PCR requires shifting between three temperatures and as many as 25 repeated temperature shift operations. (b) LAMP PCR simply requires fixing at one temperature.

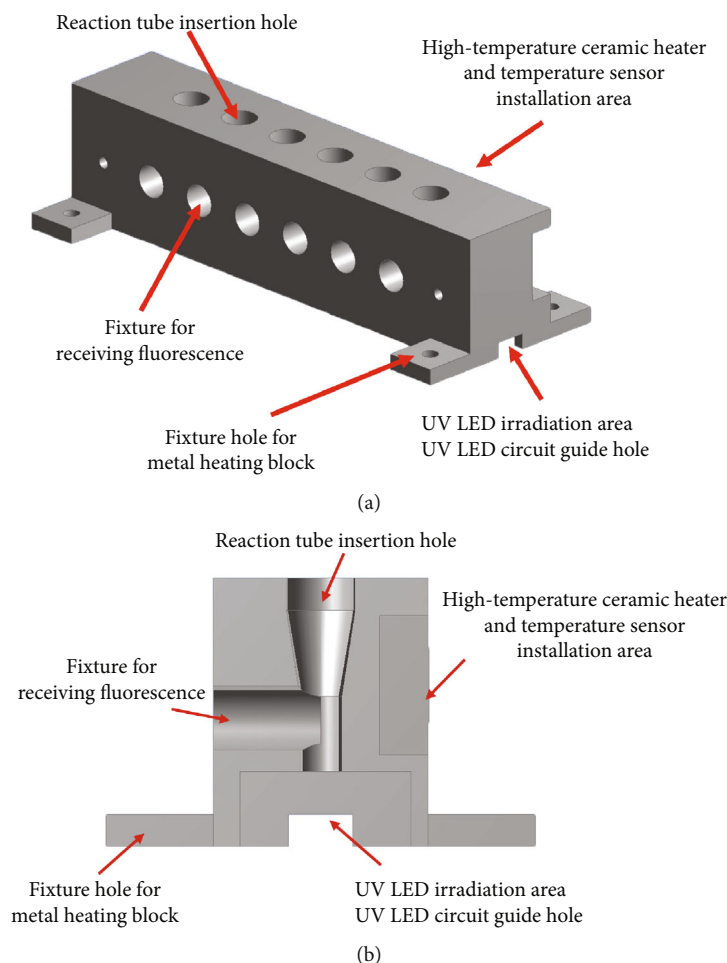


FIGURE 4: Design of the metal heating block: (a) external view of the metal heating block and its compartments and (b) a cross-sectional view of the metal heating block and its compartments.

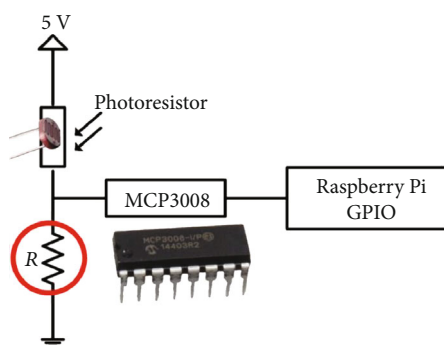


FIGURE 5: The detection circuit with a photoresistor.

computer, a power supply, a temperature controller, and a fluorescent signal detector. The equipment case was designed with SolidWorks and AutoCAD. The total size of the unit, including the temperature control system, the fluorescent signal detecting system, and a copper block, was $18.6\text{ cm} \times 8.0\text{ cm} \times 6.6\text{ cm}$. The temperature control system comprised a thin high-temperature ceramic heater, a temperature sensor, a digital temperature time controller, and a cooling fan, as shown in Figure 1(a). We used a

GCC C180II laser engraver to cut the PMMA plates and then combined the assembled optical detection dark box with the copper block and the temperature control system. The combination is shown in Figure 1(b).

The Raspberry Pi was the core piece of hardware, which was used for the output calculation of the temperature controller to operate the heating, control the photoresistors used to capture the fluorescent signals, analyze the fluorescent signals, and store the results, which were displayed on the screen.

The software used in the LAMP PCR detection equipment, including the main program, the stable temperature control, and the fluorescent signal detection, was programmed with Java. For the LAMP PCR heating system, we used the time and temperature controller to shorten the experimental time and improve the heating efficiency and stability. To enhance the heating efficiency, a high-temperature ceramic heater was used. With the help of a heating device, the copper block could rapidly increase the temperature to the target temperature and keep it constant. The temperature distribution of the metal block was simulated using ANSYS software. Figure 2(a) shows that the overall temperature difference was less than 0.3°C .

TABLE 1: Relationship between the resistance value of resistor R and the voltage of the photoresistor when the photoresistor was not illuminated with UV light.

Resistor R (Ω)	Voltage of the photoresistor (V)			Average (V)	STDEV	CV
	1st	2nd	3rd			
10 k	0.18	0.22	0.23	0.210	0.02160	10.287%
30 k	0.57	0.58	0.69	0.613	0.05437	8.864%
50 k	0.58	0.55	0.67	0.600	0.05099	8.498%
100 k	0.91	0.99	0.93	0.943	0.03399	3.604%
150 k	1.19	1.21	1.27	1.223	0.03399	2.779%
200 k	1.53	1.62	1.49	1.547	0.05437	3.515%
250 k	2.48	2.2	2.25	2.310	0.12193	5.278%
300 k	2.49	2.41	2.55	2.483	0.05735	2.309%

TABLE 2: Relationship between the resistance value of resistor R and the voltage of the photoresistor when the photoresistor was illuminated with UV light.

Resistor R (Ω)	Voltage of the photoresistor (V)			Average (V)	STDEV	CV
	1st	2nd	3rd			
10 k	1.27	1.25	1.24	1.253	0.01247	0.995%
30 k	2.49	2.5	2.54	2.510	0.02160	0.861%
50 k	3.31	3.33	3.35	3.330	0.01633	0.490%
100 k	4.04	4.04	4.05	4.043	0.00471	0.117%
150 k	4.33	4.34	4.34	4.337	0.00471	0.109%
200 k	4.48	4.49	4.49	4.487	0.00471	0.105%
250 k	4.59	4.57	4.59	4.583	0.00943	0.206%
300 k	4.66	4.67	4.67	4.667	0.00471	0.101%

TABLE 3: Results for LAMP PCR heating and the optical detection experiment.

Time (min)	Positive (V)	Negative (V)
0	2.702	3.499
5	2.778	3.570
10	2.755	3.627
15	2.718	3.582
20	2.729	3.550
25	2.843	3.476
30	2.787	3.467
35	2.864	3.432
40	2.882	3.591
45	3.013	3.585
50	3.043	3.529
55	3.015	3.554
60	3.153	3.540

The cross-sectional temperature distribution in Figure 2(b) also shows that the temperature difference between the reaction tube placement area and the high-temperature

ceramic heater was within 0.1°C . Since the temperature in the chamber during LAMP PCR only had to be kept between 60 and 65°C , it was much easier to control the temperature with LAMP PCR than with conventional PCR, which requires adjusting the thermal cycling control more than 25 times to shift between three different temperatures. Therefore, LAMP PCR can greatly reduce the costs of hardware development and production. The differences in the LAMP PCR and conventional PCR heating processes are shown in Figure 3.

For the experiment, we used three chemicals produced by Eiken Chemical Co., Ltd., Japan: a DNA amplification kit, a fluorescent detection reagent, and the DNA control set. In terms of fluorescent signals, we first used 365 nm ultraviolet light-emitting diodes to excite the specimens. The specimens then emitted fluorescent signals. All of these signals could be detected with photoresistors, for which the detection process is illustrated in Figure 4. MCP3008 IC is an 8-channel, 10-bit analog-to-digital converter (ADC), as shown in Figure 5. The analog signals are transformed into digital signals and transmitted to the Raspberry Pi for the detection data analysis. The detection circuit with a photoresistor is illustrated in Figure 5.

This LAMP PCR detection equipment employs photoresistors to read the fluorescent signals emitted from an amplified DNA sample excited with a 365 nm UV light. When the fluorescent signal is brighter, the voltage value of the photoresistor will be higher. A photoresistor has to be in series with a fixed resistor R , highlighted as a red circle in Figure 5, to be able to measure the voltage variances across the photoresistor. However, the resistance value of resistor R will affect the photoresistor voltage variances. Therefore, we had to obtain the optimal resistance value of the connected resistor R . The relationship between the photoresistor and resistor R was measured before and after the photoresistor was excited with UV light, for which the recorded data are shown in Tables 1 and 2, respectively. Both tables indicate that a 150 k Ω resistor resistance in series exhibits good stability based on the data performance before and after the photoresistor was excited with UV light.

3. Results and Discussion

After completing the entire 60-minute heating reaction, we used UV LEDs to excite the specimens in order to produce fluorescent signals. Then, the positive and negative control specimens were detected using photoresistors to detect the emitted fluorescent signals. The data are shown in Table 3 and Figure 6.

As shown in Figure 6, the emitted fluorescent signals for the positive control specimen after amplification were brighter than that of the unamplified original sample, and the photoresistor voltage signal of the amplified one was 0.145 V higher than the unamplified original sample after a reaction time of 25 minutes, which means that amplified DNA successfully began to bond with fluorescent detection reagent and produced a clone. Furthermore, after reacting for 60 minutes, the brightness of the signal

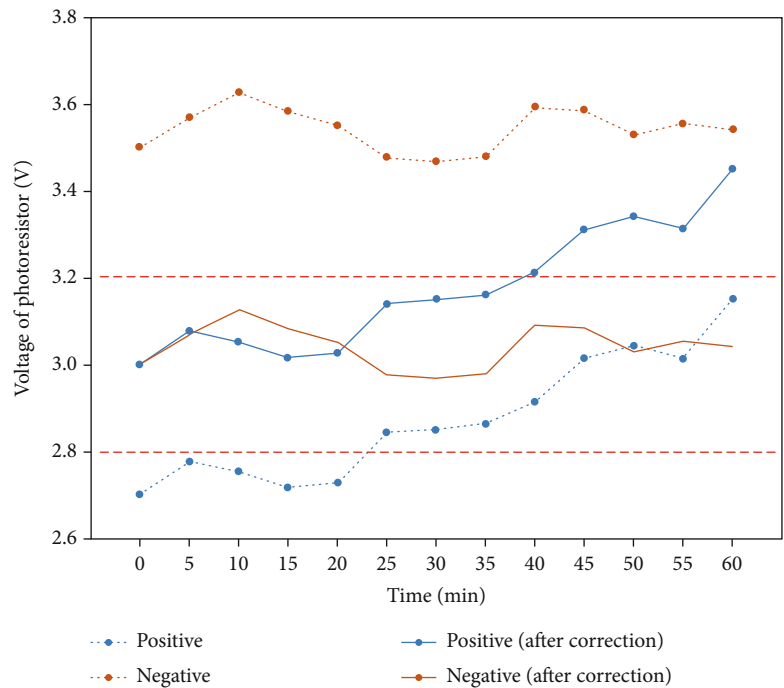


FIGURE 6: Optical detection graph of the LAMP PCR heating process.

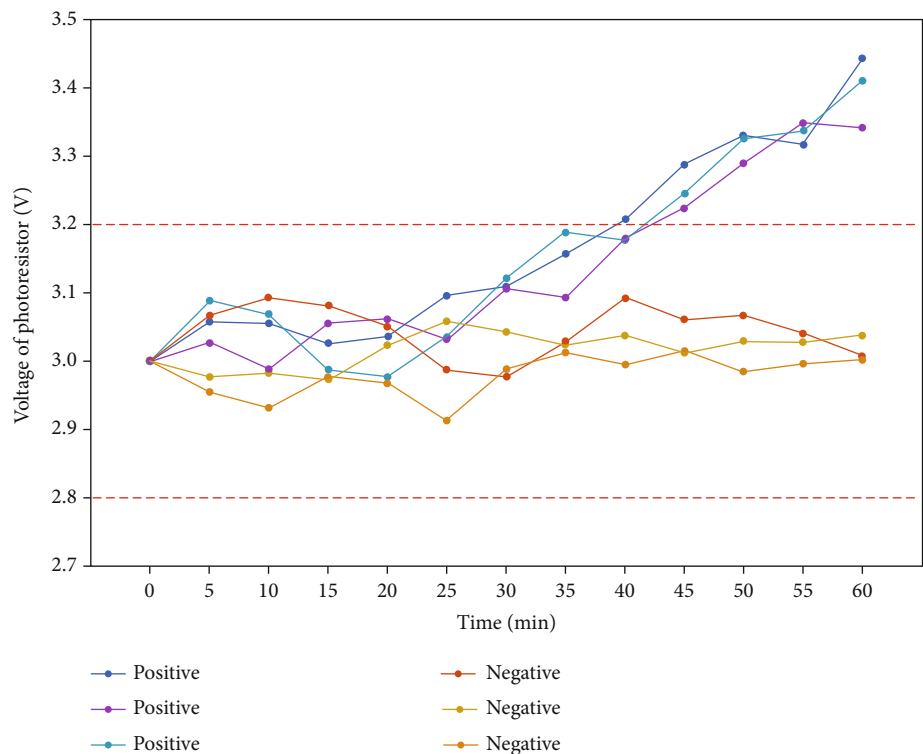


FIGURE 7: Data performance for multiple tubes of samples testing negative/positive simultaneously during LAMP PCR.

for the positive control specimen was obviously brighter than that of the negative control specimen. And the voltage signal detection value of the photoresistor of the positive control specimen was higher than negative control specimen by 0.41 V. We conducted a test by randomly

inserting three tubes of positive samples and three tubes of negative samples in the insertion holes of the reaction tube. The data in Figure 7 clearly show that the detection system could clearly distinguish between the positive and negative samples.

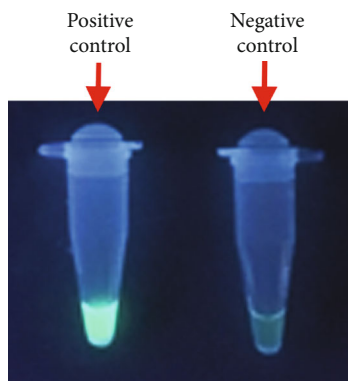


FIGURE 8: The florescence of the positive control is brighter than that of the negative control after the successful amplification.

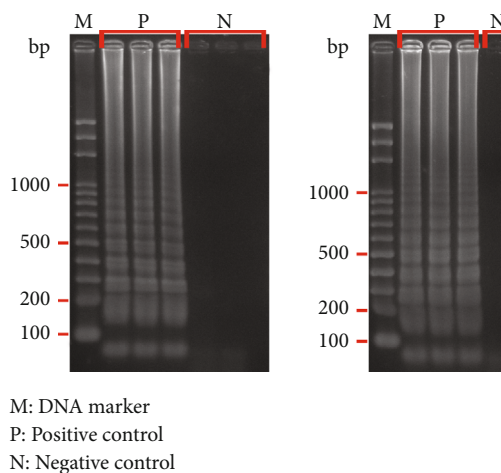


FIGURE 9: LAMP PCR results using an electrophoresis technology analysis.

By the end of the experiment, both the positive and the negative control specimens were directly excited by the 365 nm UV LED wavelengths. From the image shown in Figure 8, it can be observed that after amplification, the positive control specimen produced a very bright fluorescent signal with a wavelength of 515 nm. This result indicates the developed LAMP PCR can amplify the DNA successfully.

In this experiment, a gel electrophoresis analysis was conducted to verify whether the developed LAMP PCR equipment and the LAMP PCR designed specimens would have actual reactions. A gel electrophoresis analysis is a process of separating large molecules from their fragments in order to correctly analyze them. The negatively charged nucleic acid molecules pass through the gel grid influenced by an electric field. This separates the nucleic acid molecules [18]. After the LAMP PCR, the amplified DNA from the positive control specimen produced several different DNA fragments, whereas the negative control specimen did not, as shown in Figure 9.

4. Conclusion

This paper presents LAMP PCR detection equipment. The hardware included a metal heating block designed with SolidWorks and manufactured by a computer numerical

control machine and a fluorescent light detection system based on an optical detection dark box designed with AutoCAD and processed with a laser engraver. The software included an internal control and testing programs written in Java, including the main program and programs used to stabilize the temperature and detect fluorescent signals. After the integration of the detection equipment with the programs, the equipment activated the heating system of the polymerase chain reaction in a period ranging from 15 minutes to one hour. The signals from the fluorescent sample were detected accurately in the optical detection subsystem, where the brightness signals of the positive and negative samples had a difference of 0.41 V. Therefore, compared with current commercial detection products, the developed equipment costs less and works more efficiently. Furthermore, it has more applications. The detection equipment can be used in clinical testing in the future to improve the efficiency of disease screening. Hence, patients with infections can receive proper treatment rapidly, thereby greatly reducing mortality rates.

Data Availability

The data used to support the findings of this study are available from the corresponding author upon request.

Conflicts of Interest

The authors declare no conflict of interest.

Acknowledgments

This research was supported by the Southern Taiwan Science Park Bureau, Taiwan under grant AY-12-03-20-109.

References

- [1] H. A. Erlich, "Polymerase chain reaction," *Journal of Clinical Immunology*, vol. 9, no. 6, pp. 437–447, 1989.
- [2] Y.-C. Lin, M.-Y. Huang, K.-C. Young, T.-T. Chang, and C.-Y. Wu, "A rapid micro-polymerase chain reaction system for hepatitis C virus amplification," *Sensors and Actuators B: Chemical*, vol. 71, no. 1–2, pp. 2–8, 2000.
- [3] M. Li, "Enhancing the efficiency of a PCR using gold nanoparticles," *Nucleic Acids Research*, vol. 33, no. 21, p. e184, 2005.
- [4] Q. Zhao, "Design and numerical analysis of a joule-heating-induced continuous-flow polymerase chain reaction microchip," *Journal of Micro/ Nanolithography, MEMS, and MOEMS*, vol. 8, no. 2, p. 021102, 2009.
- [5] T. Notomi, "Loop-mediated isothermal amplification of DNA," *Nucleic Acids Research*, vol. 28, no. 12, pp. 63e–663, 2000.
- [6] T. Kono, R. Savan, M. Sakai, and T. Itami, "Detection of white spot syndrome virus in shrimp by loop-mediated isothermal amplification," *Journal of Virological Methods*, vol. 115, no. 1, pp. 59–65, 2004.
- [7] S. H. Zarkesh-Esfahani, M. T. Kardi, and M. Edalati, "Hepatitis C virus genotype frequency in Isfahan province of Iran: a descriptive cross-sectional study," *Virology Journal*, vol. 7, no. 1, 2010.
- [8] S. Fukuta, T. Iida, Y. Mizukami et al., "Detection of Japanese yam mosaic virus by RT-LAMP," *Archives of Virology*, vol. 148, no. 9, pp. 1713–1720, 2003.
- [9] S. Fukuta, S. Kato, K. Yoshida et al., "Detection of tomato yellow leaf curl virus by loop-mediated isothermal amplification reaction," *Journal of Virological Methods*, vol. 112, no. 1–2, pp. 35–40, 2003.
- [10] M. Ihira, T. Yoshikawa, Y. Enomoto et al., "Rapid diagnosis of human herpesvirus 6 infection by a novel DNA amplification method, loop-mediated isothermal amplification," *Journal of Clinical Microbiology*, vol. 42, no. 1, pp. 140–145, 2004.
- [11] C. H. Wang, K. Y. Lien, J. J. Wu, and G. B. Lee, "A magnetic bead-based assay for the rapid detection of methicillin-resistant *Staphylococcus aureus* by using a microfluidic system with integrated loop-mediated isothermal amplification," *Lab on a Chip*, vol. 11, no. 8, pp. 1521–1531, 2011.
- [12] L. L. M. Poon, C. S. W. Leung, M. Tashiro et al., "Rapid detection of the severe acute respiratory syndrome (SARS) coronavirus by a loop-mediated isothermal amplification assay," *Clinical Chemistry*, vol. 50, no. 6, pp. 1050–1052, 2004.
- [13] K. Yasuda, K. Okano, and S. Ishiwata, "Focal extraction of surface-bound DNA from a microchip using photo-thermal denaturation," *BioTechniques*, vol. 28, no. 5, pp. 1006–1011, 2000.
- [14] A. Sappat, S. Mongpraneet, T. Lomas, and A. Tuantranont, "Multi-channel turbidity detection of shrimp virus by loop-mediated isothermal amplification reaction," in *IEEE SENSORS 2009 Conference*, New Zealand, 2009.
- [15] J. Zhou, Y. Liao, H. Li et al., "Development of a loop-mediated isothermal amplification assay for rapid detection of *Trichosporon asahii* in experimental and clinical samples," *BioMed Research International*, vol. 2015, Article ID 732573, 9 pages, 2015.
- [16] J. Kashir and A. Yaqinuddin, "Loop mediated isothermal amplification (LAMP) assays as a rapid diagnostic for COVID-19," *Medical Hypotheses*, vol. 141, no. 109786, p. 109786, 2020.
- [17] J. Rödel, R. Egerer, A. Suleyman et al., "Use of the variplex™ SARS-CoV-2 RT-LAMP as a rapid molecular assay to complement RT-PCR for COVID-19 diagnosis," *Journal of Clinical Virology*, vol. 132, no. 104616, p. 104616, 2020.
- [18] C. Aaij and P. Borst, "The gel electrophoresis of DNA," *Biochimica et Biophysica Acta (BBA)-Nucleic Acids and Protein Synthesis*, vol. 269, no. 2, pp. 192–200, 1972.

Research Article

Biosynthesis of Zinc Oxide Nanoparticles Using Aqueous *Piper betle* Leaf Extract and Its Application in Surgical Sutures

Quynh Mai Thi Tran,¹ Hong Anh Thi Nguyen ,² Van-Dat Doan ,¹ Quang-Hieu Tran,³ and Van Cuong Nguyen ¹

¹Faculty of Chemical Engineering, Industrial University of Ho Chi Minh City, 12 Nguyen Van Bao, Go Vap, Ho Chi Minh City 70000, Vietnam

²Faculty of Chemical Engineering, Ho Chi Minh City University of Food Industry, 140 Le Trong Tan St, Ho Chi Minh City, Vietnam

³Department of Chemistry, Basic Sciences Department, Saigon Technology University, Ho Chi Minh City, Vietnam

Correspondence should be addressed to Van Cuong Nguyen; nvc@iuh.edu.vn

Quynh Mai Thi Tran and Hong Anh Thi Nguyen contributed equally to this work.

Received 29 August 2020; Revised 3 January 2021; Accepted 13 January 2021; Published 13 February 2021

Academic Editor: Sheng-Joue Young

Copyright © 2021 Quynh Mai Thi Tran et al. This is an open access article distributed under the Creative Commons Attribution License, which permits unrestricted use, distribution, and reproduction in any medium, provided the original work is properly cited.

Surgical site infection (SSI), mainly caused by *Staphylococcus aureus* (*S. aureus*) and *Escherichia coli* (*E. coli*), is considered the most frequent complication in a surgical patient. Globally, surgical site infection accounts for 2.5%-41.9% and even higher rates in developing countries. SSI affects not only the patient's health but also the development of society. Like previous reports, a surgical suture increases the hazard of SSI due to its structure. The antibacterial suture is the most effective solution to decrease the SSI. Due to some unique properties, nano-zinc oxide (ZnO NPs) is one of the promising antibacterial agents for coating on the suture. In this study, we aim to synthesize the ZnO NPs using *Piper betle* leaf extract and used it to coat the suture. The effect of synthesis parameters on the size and morphology of ZnO NPs was studied as well. The UV-Vis spectrum indicated the formation of ZnO NPs with λ_{\max} at around 370 nm. The volume of leaf extract plays a role in controlling the size and morphology of zinc oxide nanoparticles. The average particle size of as-synthesized ZnO NPs was around 112 nm with a hexagonal and spherical shape. Other than that, the results proved that ZnO NPs performed a high antibacterial activity against *S. aureus* and *E. coli* with its antibacterial effectiveness up to 5 days. The ZnO NP-coated sutures also exhibited a high performance on bacterial inactivation. With key findings, this study made a tremendous contribution to lowering the burden on medical services in terms of medical treatment cost in developing countries.

1. Introduction

Surgical site infections (SSIs) are one of the most common healthcare-associated infections (HAI) in developing countries, with up to 30 days of infection after surgery (or up to one year in patients receiving implants) [1–5]. SSIs are usually caused by *Staphylococcus aureus* (*S. aureus*) and *Escherichia coli* (*E. coli*) [3, 4]. These bacteria can be found from a patient's own body (endogenous infection) or from the external environment (exogenous infection) during the surgery or after that. Almost all SSIs are due to the invasion

of bacteria during surgery, leading to more serious consequences within 5–7 days after surgery.

Although hospitals have been implementing preventions strictly, there is no significant effect. It is reported that the invasion of external bacteria from surgical sutures, especially braided multifilament sutures, is one of the factors to increase rates of surgical infection [6–10]. Braided multifilament sutures provide a larger surface area than monofilament sutures, resulting in greater bacterial adherence.

To reduce bacterial colonization, scientists and manufacturers have introduced a coating that contains antiseptic

agents such as triclosan (TC), chlorhexidine, polyhexamethylene biguanide (PHMB), and octenidine. The TC-coated surgical suture has been approved by the Food and Drug Administration (FDA) as an effective antibacterial surgical suture [8–11] and commercialised since 2002. However, there are arguments about the impact of TC on human health. Triclosan affects immune responses, ROS production, and cardiovascular functions which were reported somewhere [12].

The development of nanotechnology has distributed astonishing progress in industry, computing, medicine, etc., and even in the health care system. Silver nanoparticles (Ag NPs) have been widely used as an effective antimicrobial agent coating on wound dressing, catheter, etc. [13]. Nevertheless, there is no regulation which is clear enough for risk management of silver nanoparticles in implant medical devices. On the other hand, the human body is not able to discrete silver or silver ions, resulting in an accumulation of silver as well as destruction of DNA and red blood cells [14–16].

Unlike other metals or metal oxides, zinc oxide (ZnO) or zinc oxide nanoparticle (ZnO NP) is approved by FDA due to its biodegradability, low toxicity, and economy so it has been used in an increasing number of industrial products such as paint, coating, cosmetic, and biomedicine in the past two decades, especially in the discipline of anticancer or antibacterial fields [17, 18]. Nowadays, increasing studies demonstrate the good antibacterial properties and biocompatibility of ZnO NPs [19–27]. Because of the limitation of chemical reagents as well as their residue after reaction, physical and chemical methods are not the priority for ZnO NP preparation in the medical field. The development of green chemistry has attracted increasing attention since it is believed to be nontoxic, eco-friendly, and biocompatible. Recently, many reviews on green technology-based synthesis of nanoparticles have shown that they are promising methods for large-scale production of metal nanoparticles for biomedical applications. A wide variety of plant extracts are used for the biosynthesis of ZnO NPs, and the results proved that ZnO NPs are safe for human use alternative to Ag NPs or other metal nanoparticles [28–34]. *Piper betle* L. known as a traditional herbal medicinal plant is associated with the control of caries and periodontal disease, inflammation, antimicrobial activity, etc. [35–42]. Recently, *Piper betle* L. has been used as a reductant and capping agent in metal nanoparticles such as Ag NPs, gold nanoparticles (Au NPs), and copper oxide nanoparticles (CuO NPs) [43–45] owing to organic compounds in *Piper betle* extract (hereinafter called as ET) [35]. Until now, there are only a few studies using *Piper betle* L. extract to fabricate the ZnO NPs and evaluate its biocompatibility *in vitro* such as those by Song and Yang and Shubha et al. [28, 46]. From the aspect of medical implants, we aim to synthesize ZnO NPs using *Piper betle* leaf extract and investigate the effect of parameters on the ZnO NP formation. Then, the antibacterial activity of as-prepared ZnO NPs was investigated against *E. coli* and *S. aureus*. Finally, ZnO NPs were coated on the braided multifilament surgical suture.

As mentioned above, Song and Yang [28] evaluated the cytotoxicity towards human osteoarthritic chondrocytes of

ZnO NPs using *Piper betle* leaf extract. Zinc nitrate (ZnNO_3) and aqueous *Piper betle* leaf extract were used as precursors. In this study, water was used as a solvent during extraction instead of other solvents. It was explained that water is favourable for extracting polyphenols contained in *Piper betle* leaves. Besides, water is known as a green solvent, so it is safe for human use. The result showed that the plant extract is of negligible cytotoxicity, indicating that the cytotoxicity is due to the ZnO NPs. The NPs exhibited concentration-dependent cytotoxicity, but even at high concentrations (80–100 ppm), biocompatibility of ZnO NPs was still proved. In 2018, Shubha and his colleagues [46] also studied ZnO NPs synthesized by using aqueous *Piper betle* leaf extract against dental pathogens. As a result, ZnO NPs with smaller size (~69 nm) exhibited more potent antibacterial activity to bacteria, namely, *Streptococcus mutans* (*S. mutans*) and *Lactobacillus acidophilus* (*L. acidophilus*).

Based on these references, water and ZnNO_3 were chosen as extracting solvents and precursors, respectively. Although previous studies showed good to excellent antimicrobial activity, the effectiveness of ZnO NPs which plays an important role in the prevention of surgical site infection was still unknown. Therefore, this property is investigated in this study as well.

2. Materials and Methods

2.1. Materials. Zinc nitrate hexahydrate (CAS 10196-18-6, AR Grade) and ethanol absolute (CAS 64-17-5, AR Grade) were purchased from TCI, Japan. *Piper betle* leaves were purchased from the local market and cleaned with deionized water, followed by drying under sunlight. The dry leaves were then crushed into powder and stored in air-tight containers.

2.2. Preparation of *Piper betle* Leaf Extract (ET). This study is aimed at finding out the optimum parameters for the extraction of components from *Piper betle* leaf using deionized water (18.2 mΩ·cm resistivity) [28, 42, 46–48]. The optimum conditions were selected based on the extract yield by varying parameters: (1) ratio between material amount (g) and solvent volume (ml) (1 : 5, 1 : 10, and 1 : 15, *w/v*), (2) extraction temperature (70, 80, and 90°C), and (3) extraction time (15, 30, and 60 minutes). Briefly, a given amount of powder (2, 1, and 0.67 g) was mixed with deionized water to obtain the ratio 1 : 5, 1 : 10, and 1 : 15 (*w/v*). The mixture was then boiled for a specific time (15, 30, and 60 minutes) at different temperatures (70, 80, and 90°C). After cooling, the solution was filtered through a 0.45 μm filter membrane (Whatman filter paper). The extract was freeze-dried for 48 h to obtain the solid extract. The extract was weighed and recorded. The dried and solution extract was stored in a refrigerator for further use.

2.3. Biosynthesis of Zinc Oxide Nanoparticles. In brief, a measured volume of leaf extract was dropped-wise into 100 ml of zinc nitrate solution at different concentrations under ultrasonic bath, obtaining the ratio between volume of extract and Zn^{2+} solution as 1 : 1, 1 : 5, and 1 : 10. The aqueous reaction solution was then sonicated until a pale yellow

precipitate was observed. The precipitate was centrifuged and washed several times with double distilled water and absolute ethanol before drying and annealing at 600°C to obtain a white powder of ZnO NPs.

According to previous reports, the concentration of zinc salt, volume of extract, and pH affect the formation of ZnO NPs [30, 49–51]. It was noted that the ZnO NPs were formed only at pH 5–7 or pH 8 [49, 52]. While a total reduction of zinc nitrate to zinc oxide nanoparticles occurred at pH 8, an aggregation of zinc oxide nanoparticles to form larger nanoparticles was proceeded at pH 5–7. The pH of the extract is usually about 6–6.5, so it is necessary to use more chemical reagents to reach pH 8, leading to probable cytotoxicity as mentioned in Shubha et al.'s study [46]. Therefore, pH 5–7 was chosen in this study.

Nagarajan and Kuppusamy [52] concluded that the formation of ZnO NPs starts since the concentration of zinc ion (Zn^{2+}) is 1 mM. When the concentration of Zn^{2+} goes up to 0.01 M, a pale precipitate appears. This could be explained due to more nanoparticles formed, leading to the aggregation of the larger size of nanoparticles [53, 54]. Hence, the concentration of Zn^{2+} in this study was 0.001, 0.01, and 0.1 M, respectively.

The particle size of ZnO NPs depends on the volume of plant extract [50, 51]; the more volume of plant extract, the smaller the size of ZnO NPs. The size dependence was evaluated through the ratio between volume of extract and volume of Zn^{2+} . The ratios 1:1, 1:5, and 1:10 were selected in this study.

2.4. Characterization. The optical absorbance of samples was analysed using a UV-Vis spectrophotometer (UV-1900, Shimadzu, Japan). Morphology of ZnO NPs was determined using a Scanning Electron Microscope (SEM) at Saigon Hi-tech Park Laboratory (SHTP Lab), Ho Chi Minh, Viet Nam (HiTachi S-4800, Tokyo, Japan). The crystal structures of ZnO NPs were analysed using XRD (LabX XRD-6100, Shimadzu, Japan) from 10° to 80° in 2 θ steps using Cu K_{α} radiation. FT-IR spectroscopy instrument (Tensor 27, Bruker, Germany, 4000–400 cm^{-1}) was used to measure the surface capping groups on NPs. A small amount of sample was mixed with KBr and finely ground; then, this mixture was pressed to get a homogeneous and transparent film. The size distribution of ZnO NPs was determined using a DLS instrument (SZ 100, Horiba, Japan).

2.5. Bacteriological Studies. The antibacterial activity and its effectiveness were determined using the agar disk diffusion method [46, 55]. In order to identify how the extract influences the antibacterial ability of the material, both extract and ZnO NPs were used. Agar plates were inoculated with bacteria (*E. coli* ATCC 25922 or *S. aureus* ATCC 25923) or control (gentamicin antibiotic 10 μg). Then, filter paper disks (about 6 mm in diameter), containing ZnO NP solution or extract, were placed on the agar surface. The Petri dishes were then incubated at 37°C for 24 h and observed for growth or inhibition. The sample positions are illustrated in Figure 1.

After investigating the bactericidal ability, the antibacterial effectiveness was conducted. The agar diffusion method

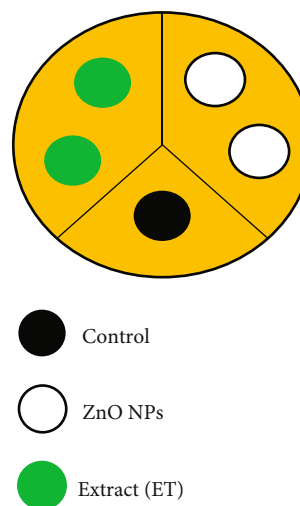


FIGURE 1: Illustration of sample position on the agar disk in bactericidal ability test.

was also used. The results were recorded after 48 (2 days), 72 (3 days), and 120 (5 days) hours of incubation. Figure 2 exhibits the sample position on the disk.

For the coated surgical suture, the AATTC Test Method 147-2004 Parallel Streak Method was applied. Specimens of the test suture (about 5 cm in length) including the corresponding untreated suture of the same material (control) were placed in intimate contact with the agar surface which has been previously streaked with inoculums of bacteria (*E. coli* ATCC 25922 or *S. aureus* ATCC 25923) (Figure 3). After incubation at 37°C for 24 h, the zone of inhibition (ZOI) was observed.

The ZOI is calculated using the following equation:

$$W = \frac{(T - D)}{2}, \quad (1)$$

in which W is the width of ZOI (mm), T is the total diameter of the test specimen and ZOI (mm), and D is the diameter of the test specimen (mm).

2.6. Statistical Analysis. Experiments were performed in triplicate for each parameter. Differences between the mean values were analysed using one-way analysis of variance (ANOVA) with $p < 0.05$.

3. Results and Discussion

3.1. Preparation of Piper betle Leaf Extract. As reported, the extraction yield was affected by various parameters such as the ratio of solid to liquid (w/v), extraction time, and extracted temperatures. In 2015, Foo and his colleagues [48] revealed that the yield of extraction of aqueous-based solvent *Piper betle* extract was higher than that of ethanol-based solvent extract. Therefore, water was used as a solvent in this study.

As shown in Figure 4, the color of the filtrated solution was transparent yellow and changed to brown powder after solvent evaporation. Figure 5 exhibits the optical absorption

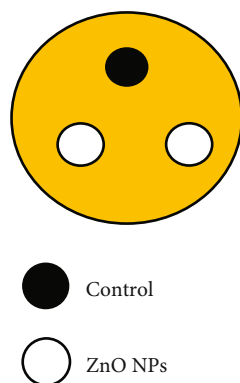


FIGURE 2: Illustration of sample position on the agar disk in antibacterial effectiveness test.

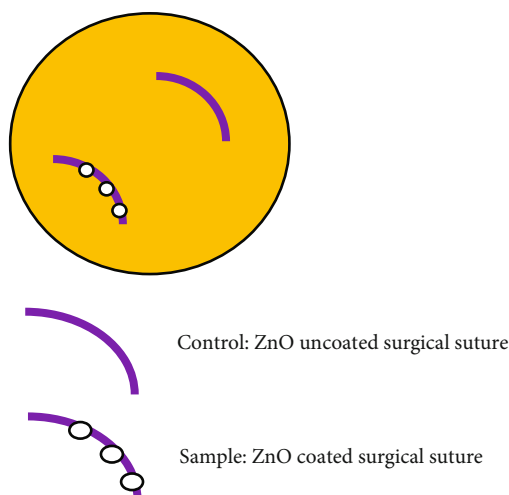


FIGURE 3: Illustration of sample position of surgical sutures on the agar disk in antibacterial test.

peak of ET at 280 and 325 nm as a previous report [28]. After freeze-drying, a brown powder was observed (Figure 4(c)), and the mass extraction and corresponding yield (%) are assumed in Table 1.

3.2. Effect of Parameters on the Extraction Yield. Various parameters ((1) ratio of solid-liquid (1:5, 1:10, and 1:15) (w/v), (2) extraction temperature (70–90°C), and (3) extraction time (15–60 minutes)) were investigated to obtain the maximum percentage of the extract (ET).

3.2.1. Effect of Ratio of Solid-Liquid and Time. To evaluate the effect of the ratio of solid-liquid on extraction yield, the temperature was kept constant at 90°C due to the higher solubility of polyphenols in water for a short time [28].

As seen in Figure 6, the yield of extraction increased when the ratio of solid-liquid decreased and reached to maximum after 30-minute extraction. Then, the yield started decreasing. It could be due to the competition of interaction between the solvents and material and/or because of the solvent evaporation during extraction.

It was noted that when the material mass was 2 grams per 10 ml (equilibrating to a ratio of 1:5), it was difficult for the solvent to assess the material which resulted in the low efficiency of extraction.

Last but not least, when the ratio of solid to liquid was 1:10 (1 gram per 10 ml), the yield was likely unchanged after 30-minute extraction which was chosen for further experiments.

3.2.2. Effect of Temperature. To investigate the effect of temperature on the yield extraction, the ratio 1:10 and time of 30 minutes were kept constant. The results from Table 2 and Figure 7 exhibited that the extraction yield increases with the increase of temperature. In a short period, the yield of extraction mainly depended on the temperature. It has been observed that the higher the temperature, the higher the yield of extraction. It could be because the temperature promotes the solubility of organic compounds in water [28].

From the point of view of the production scale, the optimal extraction conditions corresponded to the ratio between solid and liquid, temperature, and time which are 1:10, 90°C, and 30 min, respectively.

3.3. Biosynthesis of Zinc Oxide Nanoparticles. The formation of ZnO NPs was confirmed by the appearance of precipitate (Figure 8(a)). This precipitate was in brown powder after freeze-drying (Figure 10(a)) due to the coverage of phytochemicals in the extract, which evaporated under high-temperature calcination leaving the white powder (Figure 8(c)). The UV-Vis spectrum showed sharp absorption peaks at 358, 368, and 378 nm (Figure 9), indicating the presence of as-prepared ZnO NPs. This result was in agreement with other references [46].

3.3.1. Effect of Zinc Salt Concentration on the Formation of ZnO NPs. Various parameters were selected to investigate their effect on ZnO NP formation. The experimental parameters are summarized in Table 3. The results in Figure 10 confirmed the statement that ZnO NPs started to form since the concentration of Zn^{2+} is 0.001 M, and the precipitate was observed when the concentration of Zn^{2+} was equal to or larger than 0.01 M.

Particle size measurement was conducted by using the DLS technique. Table 3 summarizes the average particle size of as-prepared ZnO NPs. When the concentration of zinc salt was less than 0.1 M, zinc ions acted as a controller of nucleation; the particles distributed from 100 to 200 nm with average size (Z-average) of 112.9 nm. Besides, its polydispersity index (PDI) was in the average range ($0.3 < \text{PDI} < 0.5$) (Figure 11). Once the concentration reached 0.1 M, PDI increased ($\text{PDI} > 1$), resulting in the aggregation of smaller particles to form bigger particles. For this reason, the DLS technique was not appropriate.

It has been established earlier that larger size nanoparticles of ZnO showed comparatively lower toxicity [46]. Other than that, the storage of the solid state was more favourable in comparison with the liquid state. Therefore, the concentration of 0.1 M of Zn^{2+} was selected for further experiments.

3.3.2. Effect of Liquid to Liquid Ratio on the Size and Morphology of ZnO NPs. To understand how the extract

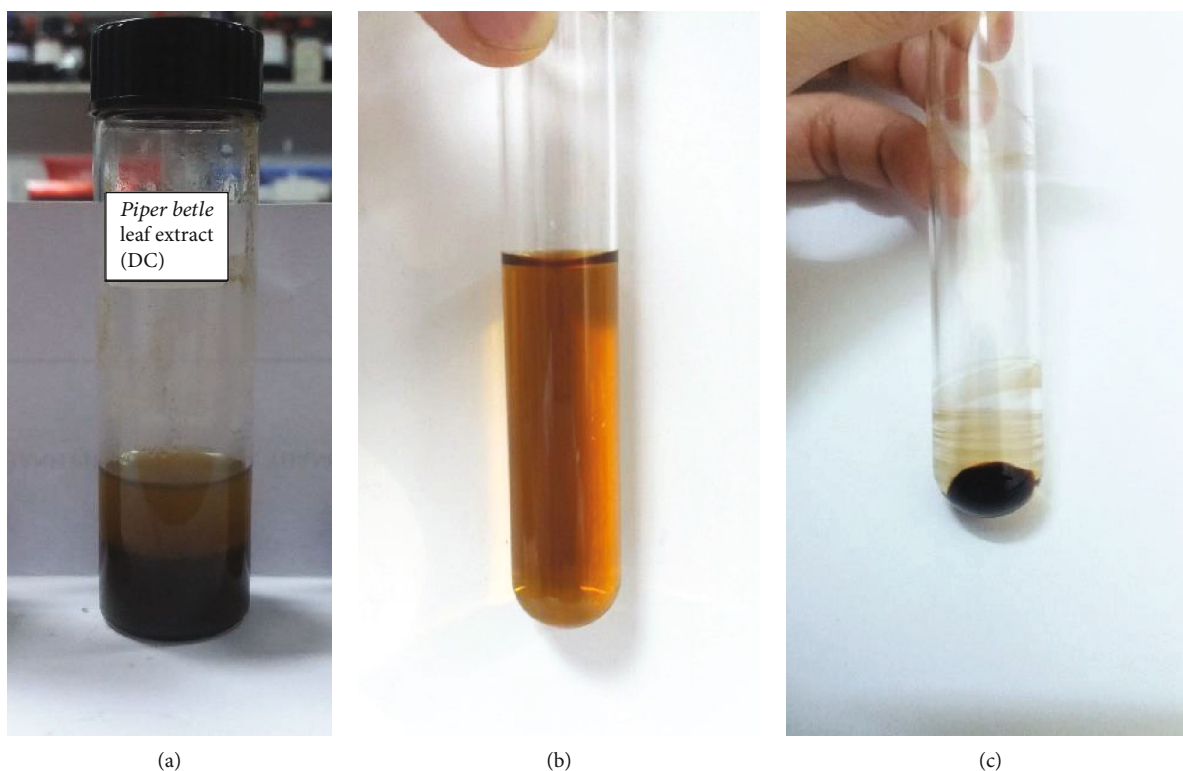


FIGURE 4: The color change of *Piper betle* extract: (a) color of extract before filtration, (b) color of extract after filtration, and (c) color of dried extract.

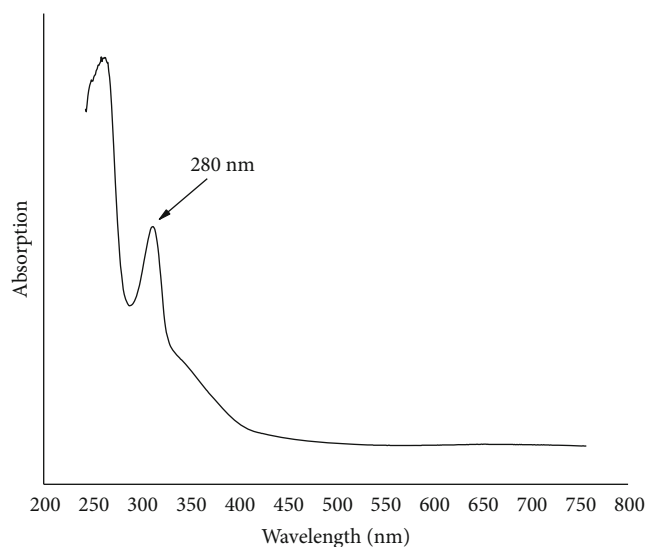


FIGURE 5: UV-Vis spectrum of *Piper betle* leaf extract.

volume affects the size and the morphology of ZnO NPs, 10, 20, and 100 ml of extract were added to 100 ml of aqueous Zn^{2+} solution under ultrasonic bath for 4 hours. The weights of dried ZnO NPs and sintered ZnO NPs are summarized in Table 4. It was clear that the product weight increases when the volume of extract increases. Hence, the ratio 1 : 1 was chosen to maximize the product quantity.

As shown in SEM results, the volume of extract played a role in controlling the size and morphology of ZnO NPs (Figure 12). When the volume of ET increased from 10 to 100 ml, the size of particles reduced and specific morphology was formed [50, 51]. Besides, the aggregation due to the pH at 5-7 was clearly observed. Figure 13 exhibits the morphology of ZnO NPs sintered at a higher temperature (600°C).

TABLE 1: Experimental results for preparation of *Piper betle* leaf extract using water solvent.

No.	Code	Material quantity (g)	Extraction time (min)	Mass of extract (g)	Yield (%)
1	ET1	2	15	0.23	11.5
2	ET2	2	30	0.3	15
3	ET3	2	60	0.13	6.5
4	ET4	1	15	0.21	21
5	ET5	1	30	0.24	24
6	ET6	1	60	0.23	23
7	ET7	0.67	15	0.15	22.4
8	ET8	0.67	30	0.2	29.9
9	ET9	0.67	60	0.17	25.4

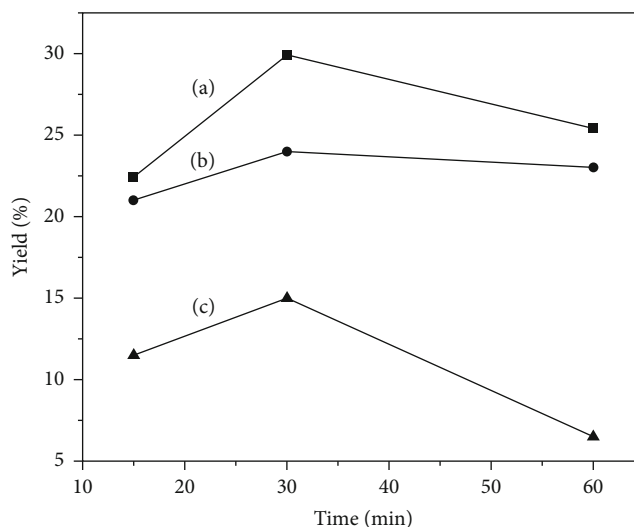


FIGURE 6: Effect of material quantity on extraction yield (a) ratio of 1 : 15, (b) ratio of 1 : 10, and (c) ratio of 1 : 5.

TABLE 2: Effectiveness of temperature on yield extract.

No.	Code	Extraction temperature (°C)	Mass of extract (g)	Yield (%)
1	ET10	70	0.12	12
2	ET11	80	0.21	21
3	ET12	90	0.24	24

ZnO NPs had a nearly hexagonal shape and spherical shape which could be explained by the functional group of compounds in the extract [30, 49].

FT-IR analysis was used to measure the functional groups in ET and ZnO NPs. Figure 14(a) confirms the presence of organic compounds such as amines, carboxylic acids, alkanes, esters, and alkenes with the absorption peaks at 3477.51, 2888.25, and 1637.27 cm^{-1} , ranging from 1416.62 to 956.62 cm^{-1} . In the spectrum of ZnO NPs (Figure 14(b)), the absence of peaks from 1416.62 to 956.62 cm^{-1} demonstrated the removal of almost all organic compounds after sintering. It is noted that the presence of a peak at 463.92 cm^{-1} contributed to the formation of ZnO NPs which

complies with the color change of product after calcination (Figure 8).

Diffraction peaks of ZnO NPs were observed at 2θ values of 33.6°, 34.5°, 35.2°, 56.8°, 62.6°, 69.5°, and 70.2° corresponding to lattice planes (100), (002), (101), (103), (200), (112), and (201), respectively (Figure 15). The peaks are attributed to the hexagonal phase of ZnO (JCPDS 36-1451). There were still some impurity peaks due to the plant extract residues. Crystallite size (D) of NPs calculated by Scherrer's equation was 6.87 nm.

3.4. Bacteriological Studies

3.4.1. Role of ET and ZnO NPs in the Bacterial Ability. The antibacterial activity of ZnO NPs and its effectiveness was assayed against two major bacteria *E. coli* and *S. aureus*, respectively, by the agar disk diffusion method. The minimum inhibitory concentration for zinc oxide nanoparticles was 0.41 mg/ml for *E. coli* and 0.81 mg/ml for *S. aureus*, respectively. The minimum bactericidal concentration was 0.81 mg/ml for *E. coli* and 1.62 mg/ml for *S. aureus*, respectively. The ZOI of ZnO NPs was determined and calculated from equation (1) with the diameter of filter paper being

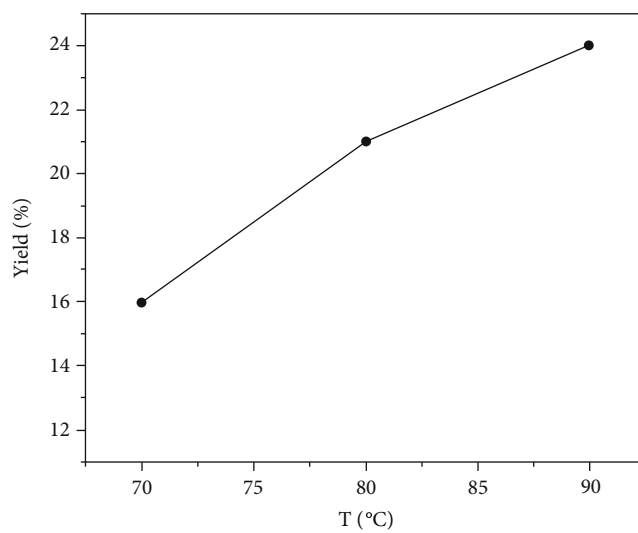


FIGURE 7: Effect of temperature on extraction yield.

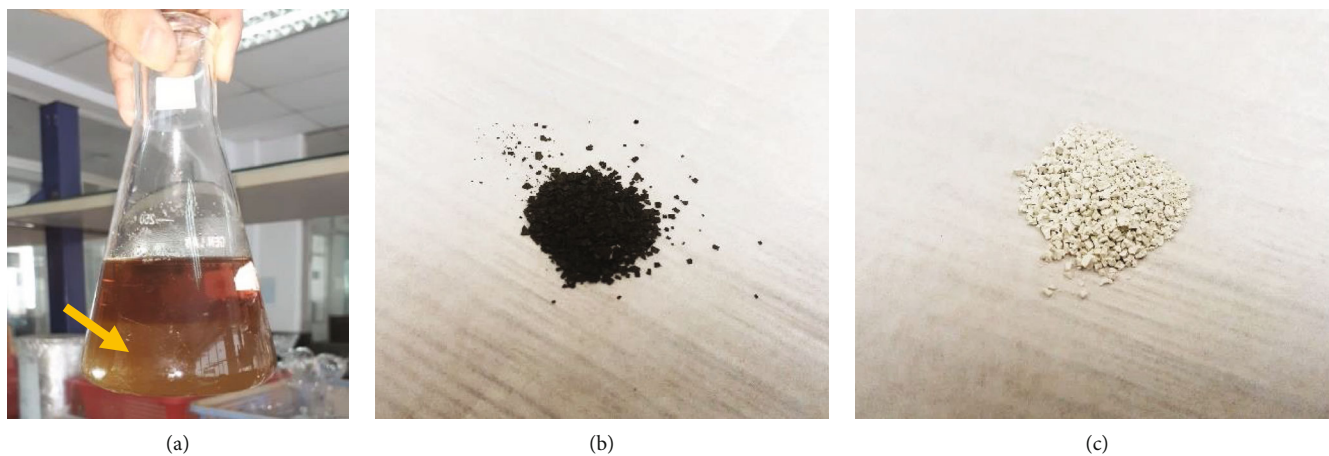


FIGURE 8: (a) The presence of as-synthesized ZnO NPs; (b) color of ZnO NPs before calcination; (c) color of ZnO NPs before calcination.

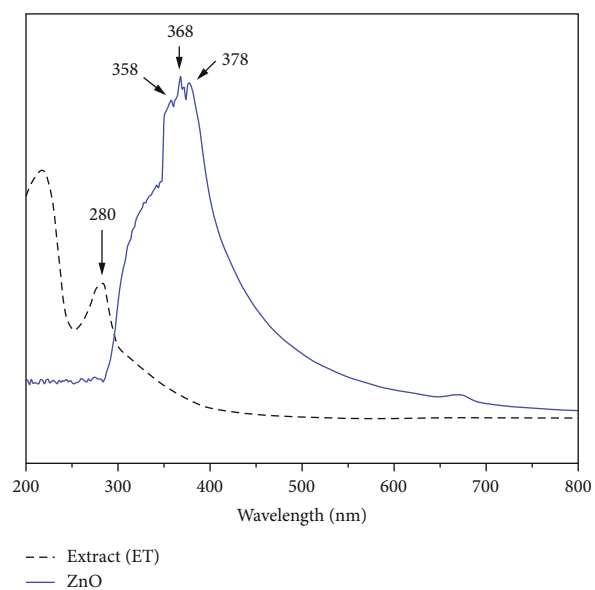
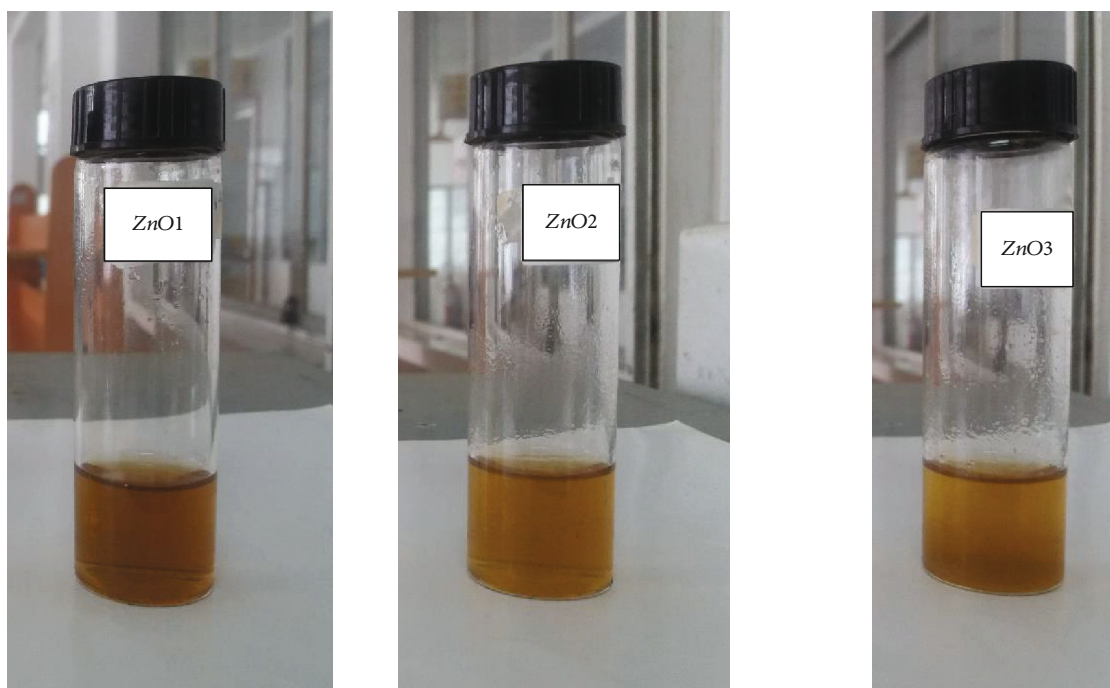


FIGURE 9: UV-Vis spectra of ET and ZnO NPs.



(a) ZnO NPs 1: transparent solution (b) ZnO NPs 2: precipitate starts to be observed (c) ZnO NPs 3: precipitate was observed clearly

FIGURE 10: Effectiveness of zinc ion concentration on ZnO NP formation.

TABLE 3: Experimental parameters used in ZnO NP synthesis.

No.	Code	$[Zn^{2+}]$ (M)	$\frac{V_{ET}}{V_{Zn^{2+}}}$	Reaction time (h)	(Z-average) (nm)	PDI
1	ZnO NPs 1	0.001	1 : 1	4	112.9	0.330
2	ZnO NPs 2	0.01	1 : 1	4	3640.2	1.018
3	ZnO NPs 3	0.1	1 : 1	4	3791.8	5.161

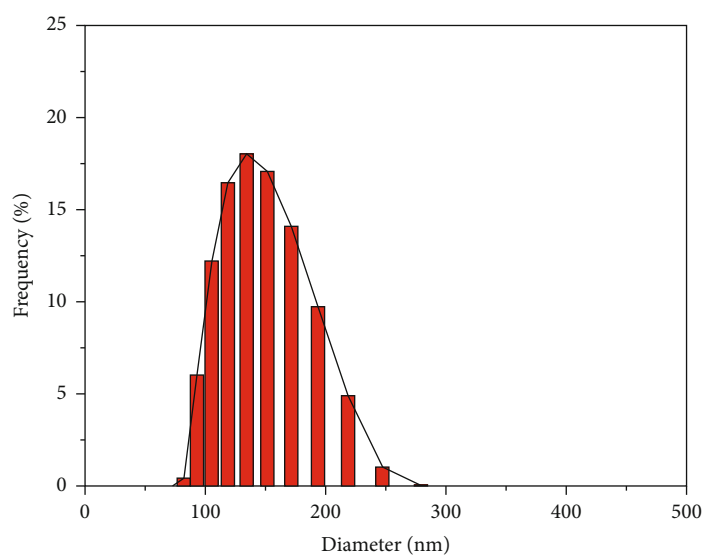


FIGURE 11: Dynamic light scattering (DLS) of ZnO NPs at a concentration of 0.001 M.

TABLE 4: The experiment results of ZnO NP synthesis using various volumes of ET and time.

No.	Code	[Zn ²⁺] (M)	V _{ET} (ml)	$\frac{V_{ET}}{V_{Zn^{2+}}}$	Reaction time (h)	Mass of dried ZnO NPs (g)	Mass of sintered ZnO NPs (g)
1	ZnO NPs 4	0.1	10	1 : 10	4	0.005	0.003
2	ZnO NPs 5	0.1	20	1 : 5	4	0.030	0.010
3	ZnO NPs 6	0.1	100	1 : 1	4	1.158	0.080

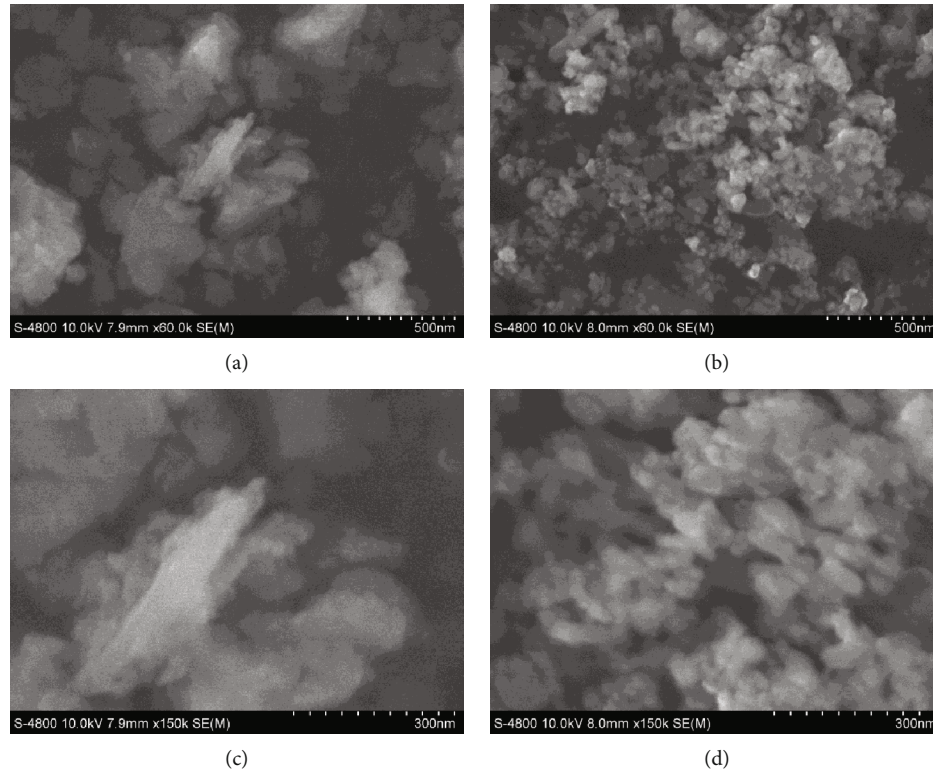


FIGURE 12: SEM images of synthesized ZnO NPs using different volumes of ET. SEM images of ZNO NPs using 10 ml of ET at magnification of (a) 60k and (c) 150k. SEM images of ZNO NPs using 100 ml of ET at magnification of (b) 60k and (d) 150k.

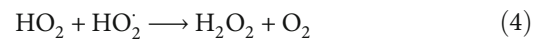
6 mm and that of suture (USP 1) being 0.4 mm. As seen in Figure 16, the bactericidal properties were due to ZnO NPs. The extract only played a role as reductants and capping agents and morphology controller.

As a result in Table 5, the ZOI of ZnO NPs on *E. coli* after 24 h incubation were quite small; it could be because of differences in the structure of bacteria [50]. In this study, the particle size of ZnO was bigger than 10 nm so the particles had adhered to the outer layer of bacteria plasma membranes, increased the surface tension, and inhibited the polarization of the membrane, allowing ZnO NP molecules to internalize into the cell. However, the cell membrane of *E. coli* has an additional outer plasma membrane, leading to slower diffusion of nanoparticles into the cell structure compared with the *S. aureus*. Therefore, the number of ZnO NPs that entered *E. coli* was less than that of *S. aureus* in 24 h.

3.4.2. Antibacterial Effectiveness of ZnO NPs. As seen in Figure 17, the bactericidal effectiveness of ZnO NPs could reach five days on both *E. coli* and *S. aureus*. The ZOI of nanoparticles increased after 48 h of incubation and maintained until five days (Table 5). This result met our require-

ment expectation that ZnO NPs could reduce the SSI within 5-7 days after surgery. It was noted that the ZOI of ZnO NPs after 48, 72, and 120 h of incubation on *E. coli* was better than that of the first 24 h. It might be explained as follows.

As the peptidoglycan of *E. coli* is thinner compared with that of *S. aureus*, ZnO NPs passed through the outer membrane of the bacteria cell easier. Here, the nanoparticles generate free electrons, which react with oxygen inside the bacteria cell. As a result, reagent oxygen species (ROS) are formed according to equations (2)–(4). These ROS will destroy protein structures and DNA structure leading to cell death. ROS was considered the antibacterial mechanism in this study:



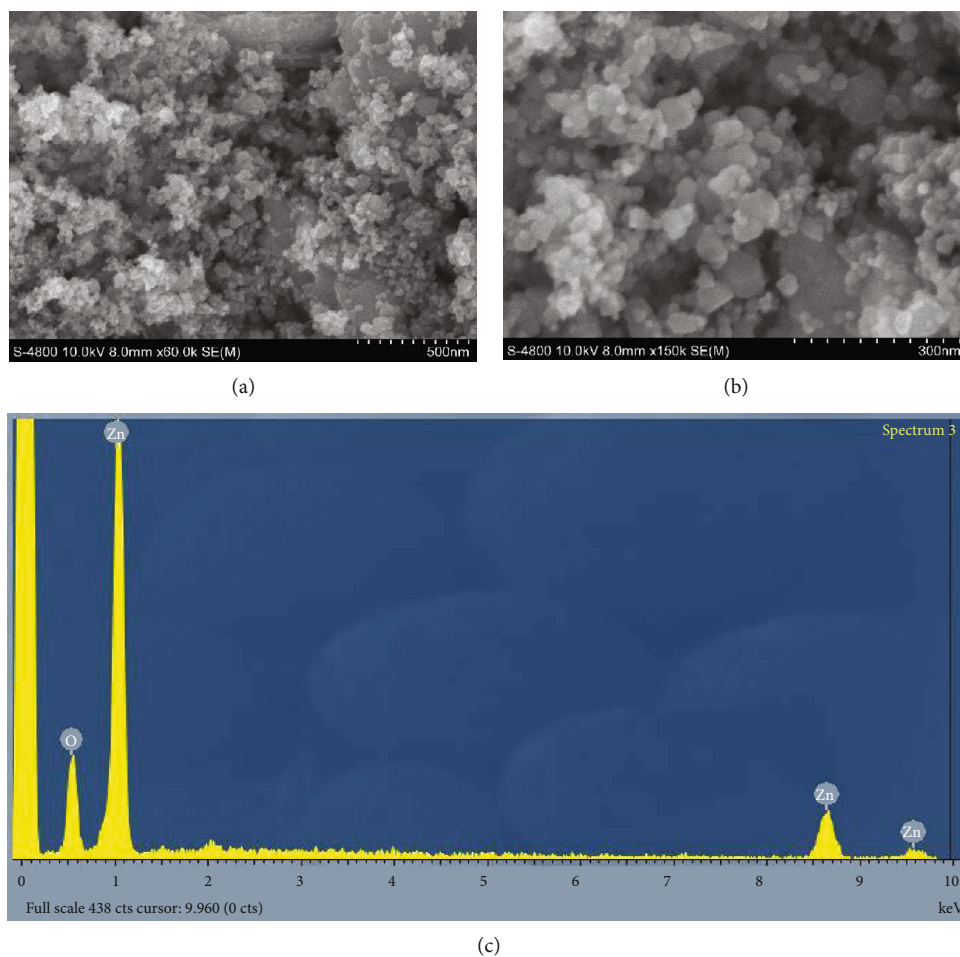


FIGURE 13: The morphology of ZnO NPs under SEM spectroscopy at a magnification of (a) 60 k và (b) 150 k; (c) EDX spectrum.

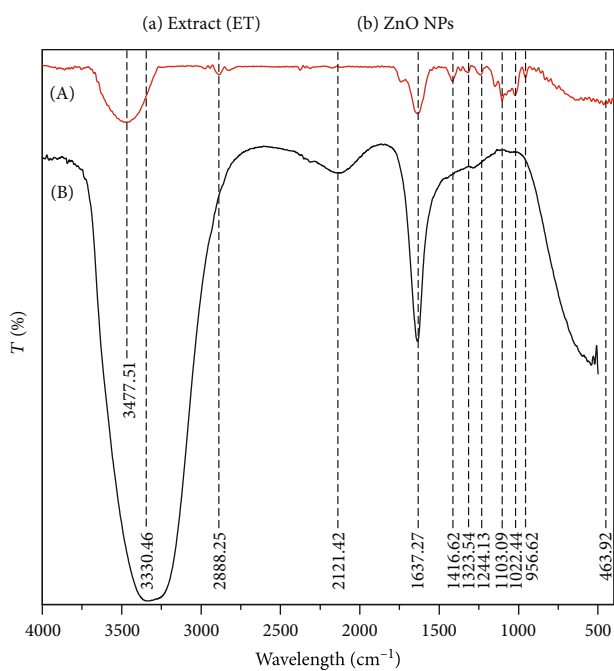


FIGURE 14: FT-IR spectra of (a) dry extract and (b) ZnO NPs.

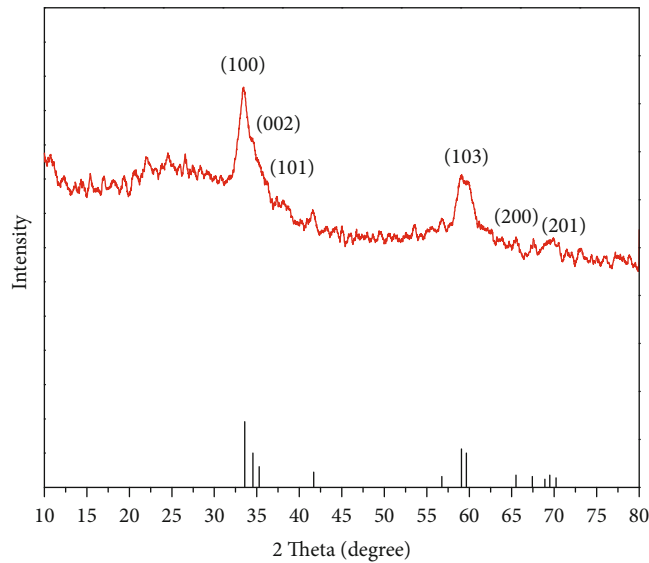


FIGURE 15: XRD pattern of ZnO NPs.

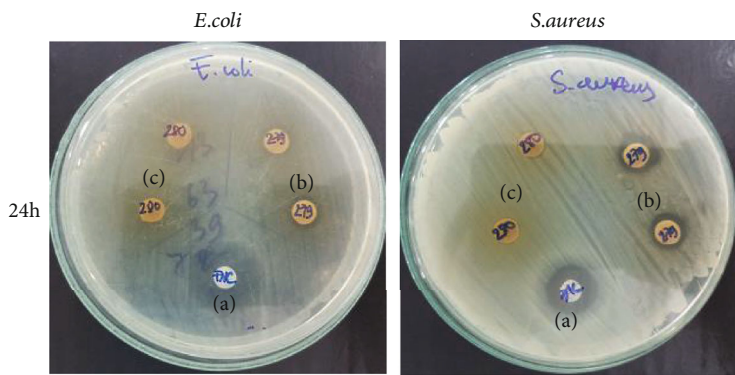


FIGURE 16: Antibacterial result of ET and ZnO NPs: (a) control, (b) ZnO NPs, and (c) extract.

TABLE 5: Zone of inhibition of ZnO NPs and ZnO NP-coated surgical sutures (hereinafter referred to as plus suture).

Bacteria	ZOI of ZnO NPs (mm)			
	24 h	48 h	72 h	120 h
<i>E. coli</i>	1	4	4	4
<i>S. aureus</i>	2	3	3	3

3.4.3. Bactericidal Test of ZnO NPs Coated on Surgical Sutures. Figure 18 exhibits that the ZnO-coated surgical suture has antibacterial ability compared with the control even after coating one time. This promising result proved that ZnO NPs are able to be applied in the medical device category.

4. Conclusions

In this study, a simple, low-cost method for the preparation of ZnO NPs using *Piper betle* leaf extract has been successfully achieved. There have been some evidences suggesting that green synthesis of ZnO NPs has enhanced the use in implan-

tation. High-tech analysis has been used to demonstrate the formation of ZnO NPs. Apart from that, this study evaluated the size and morphology control based on the volume of *Piper betle* leaf extract. The ZnO NPs showed good antibacterial performance on *E. coli* and *S. aureus*, which are the main reasons for surgical site infection. The antibacterial effectiveness of ZnO NPs was observed up to 5 days, which is able to reduce the rate of SSI significantly. The results from bacteriological studies also confirmed that the antibacterial property of the ZnO NP-coated suture is better than that of the uncoated one, which is promising for applying ZnO NPs in the medical category.

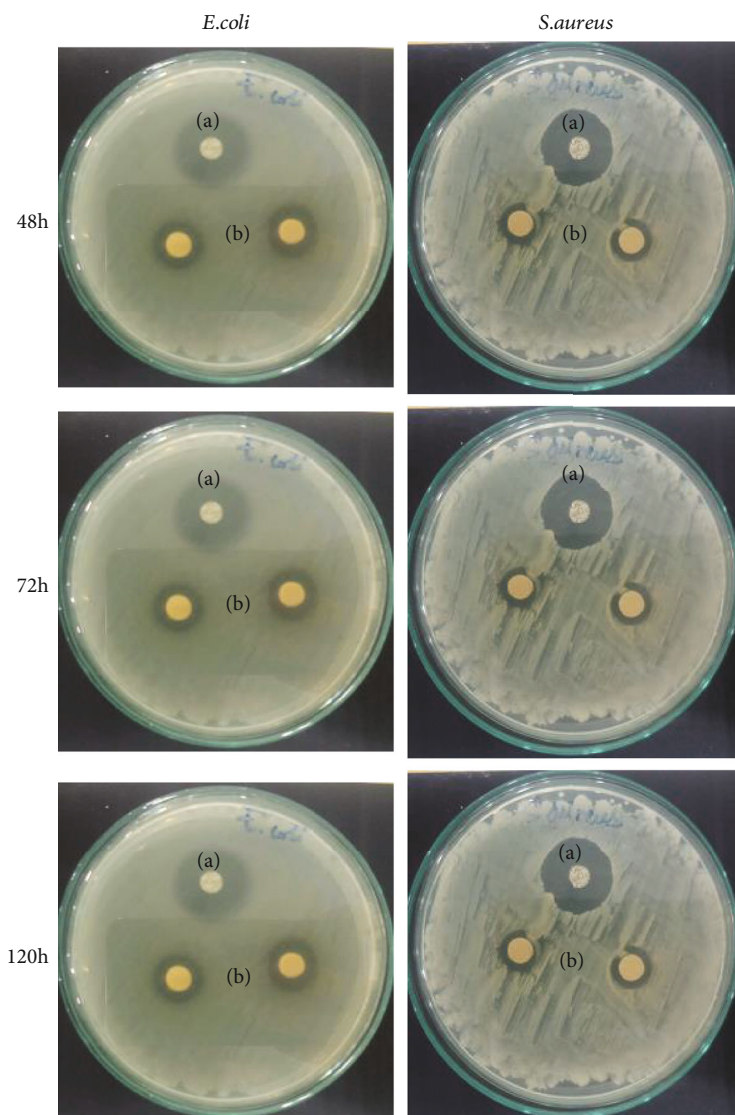


FIGURE 17: Zone of inhibition of ZnO NPs on *E. coli* and *S. aureus* at different times: (a) control and (b) ZnO NPs.

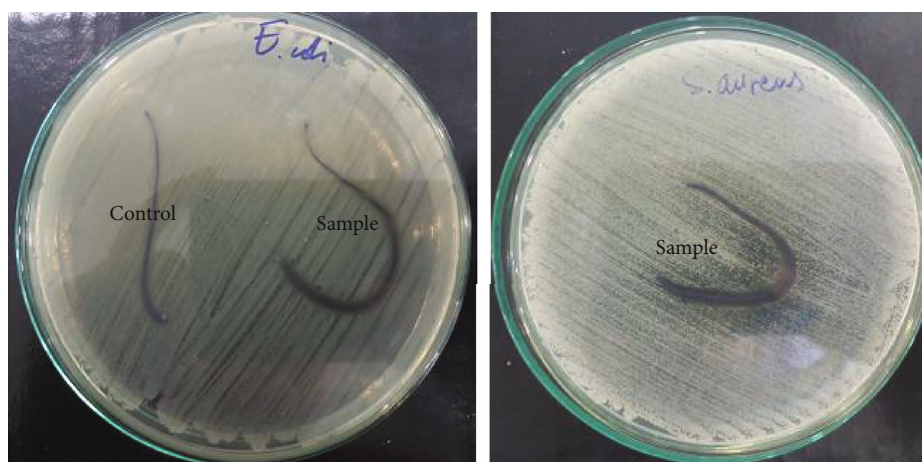


FIGURE 18: Zone of inhibition of control (ZnO-uncoated suture) and sample (ZnO-coated suture).

Data Availability

Raw data were generated at the faculty of chemical engineering, Industrial University of Ho Chi Minh City, Vietnam. Derived data supporting the findings of this study are available from the corresponding author on request.

Conflicts of Interest

The authors declare that there is no conflict of interest regarding the publication of this paper.

Authors' Contributions

Quynh Mai Thi Tran and Hong Anh Thi Nguyen contributed equally to the work.

Acknowledgments

This study is supported by the Industrial University of Ho Chi Minh City and Ho Chi Minh City University of Food Industry, Vietnam, for financial support.

References

- [1] J. M. Badia, A. L. Casey, N. Petrosillo, P. M. Hudson, S. A. Mitchell, and C. Crosby, "Impact of surgical site infection on healthcare costs and patient outcomes: a systematic review in six European countries," *Journal of Hospital Infection*, vol. 96, no. 1, pp. 1–15, 2017.
- [2] G. de Lissoy, K. Fraeman, V. Hutchins, D. Murphy, D. Song, and B. B. Vaughn, "Surgical site infection: incidence and impact on hospital utilization and treatment costs," *American Journal of Infection Control*, vol. 37, no. 5, pp. 387–397, 2009.
- [3] D. Gould, "Causes, prevention and management of surgical site infection," *Nursing Standard*, vol. 26, no. 47, pp. 47–56, 2012.
- [4] C. D. Owens and K. Stoessel, "Surgical site infections: epidemiology, microbiology and prevention," *Journal of Hospital Infection*, vol. 70, Supplement 2, pp. 3–10, 2008.
- [5] D. E. Fry, "Surgical site infection: pathogenesis and prevention," 2003, <https://www.medscape.org/viewarticle/448981>.
- [6] A. M. Spagnolo, G. Ottria, D. Amicizia, F. Perdeli, and M. L. Cristina, "Operating theatre quality and prevention of surgical site infections," *Journal of Preventive Medicine and Hygiene*, vol. 54, no. 3, pp. 131–137, 2013.
- [7] S. Morrison, A. Singh, J. Rousseau, and J. S. Weese, "Adherence of methicillin-resistant *Staphylococcus pseudintermedius* to suture materials commonly used in small animal surgery," *American Journal of Veterinary Research*, vol. 77, no. 2, pp. 194–198, 2016.
- [8] K. R. Brown, C. P. Johnson, M. P. Goheen et al., "Bacterial adherence to surgical sutures: can antibacterial-coated sutures reduce the risk of microbial contamination?," *Journal of the American College of Surgeons*, vol. 203, no. 4, pp. 481–489, 2006.
- [9] J. Dhom, D. A. Bloes, A. Peschel, and U. K. Hofmann, "Bacterial adhesion to suture material in a contaminated wound model: comparison of monofilament, braided, and barbed sutures," *Journal of Orthopaedic Research*, vol. 35, no. 4, pp. 925–933, 2017.
- [10] J. R. Fowler, T. A. Perkins, B. A. Buttarro, and A. L. Truant, "Bacteria adhere less to barbed monofilament than braided sutures in a contaminated wound model," *Clinical Orthopaedics & Related Research*, vol. 471, no. 2, pp. 665–671, 2013.
- [11] C. Mingmalairak, "Antimicrobial sutures: new strategy in surgical site infections," *Science against Microbial Pathogens: Communicating Current Research and Technological Advances: Formatex Research Center*, vol. 13, no. 23, pp. 313–323, 2011.
- [12] A. Morad Asaad and S. Ahmad Badr, "Surgical site infections in developing countries: current burden and future challenges," *Clinical Microbiology: Open Access*, vol. 5, no. 6, 2016.
- [13] M. Konop, T. Damps, A. Misicka, and L. Rudnicka, "Certain aspects of silver and silver nanoparticles in wound care: a minireview," *Journal of Nanomaterials*, vol. 2016, Article ID 7614753, 10 pages, 2016.
- [14] L. Q. Chen, L. Fang, J. Ling, C. Z. Ding, B. Kang, and C. Z. Huang, "Nanotoxicity of silver nanoparticles to red blood cells: size dependent adsorption, uptake, and hemolytic activity," *Chemical Research in Toxicology*, vol. 28, no. 3, pp. 501–509, 2015.
- [15] Z. Ferdous and A. Nemmar, "Health impact of silver nanoparticles: a review of the biodistribution and toxicity following various routes of exposure," *International Journal of Molecular Sciences*, vol. 21, no. 7, p. 2375, 2020.
- [16] A. R. Gliga, S. Skoglund, I. O. Wallinder, B. Fadeel, and H. L. Karlsson, "Size-dependent cytotoxicity of silver nanoparticles in human lung cells: the role of cellular uptake, agglomeration and ag release," *Particle and Fibre Toxicology*, vol. 11, no. 1, p. 11, 2014.
- [17] Y. Zhang, T. Nayak, H. Hong, and W. Cai, "Biomedical applications of zinc oxide nanomaterials," *Current Molecular Medicine*, vol. 13, no. 10, pp. 1633–1645, 2013.
- [18] V. Parihar, M. Raja, and R. Paulose, "A brief review of structural, electrical and electrochemical properties of zinc oxide nanoparticles," *Reviews on Advanced Materials Science*, vol. 53, no. 2, pp. 119–130, 2018.
- [19] Y. Gutha, J. L. Pathak, W. Zhang, Y. Zhang, and X. Jiao, "Antibacterial and wound healing properties of chitosan/poly(vinyl alcohol)/zinc oxide beads (CS/PVA/ZnO)," *International Journal of Biological Macromolecules*, vol. 103, pp. 234–241, 2017.
- [20] E. Ozkan, E. Allan, and I. P. Parkin, "White-light-activated antibacterial surfaces generated by synergy between zinc oxide nanoparticles and crystal violet," *ACS Omega*, vol. 3, no. 3, pp. 3190–3199, 2018.
- [21] R. Rajendra, C. Balakumar, H. A. M. Ahammed, S. Jayakumar, K. Vaideki, and E. Rajesh, "Use of zinc oxide nano particles for production of antimicrobial textiles," *International Journal of Engineering, Science and Technology*, vol. 2, no. 1, 2010.
- [22] J. Jiang, J. Pi, and J. Cai, "The advancing of zinc oxide nanoparticles for biomedical applications," *Bioinorganic Chemistry and Applications*, vol. 2018, Article ID 1062562, 18 pages, 2018.
- [23] A. A. Tayel, W. F. El-Tras, S. Moussa et al., "Antibacterial action of zinc oxide nanoparticles against foodborne pathogens," *Journal of Food Safety*, vol. 31, no. 2, pp. 211–218, 2011.
- [24] A. A. Mostafa, "Antibacterial activity of zinc oxide nanoparticles against toxigenic *Bacillus cereus* and *Staphylococcus aureus* isolated from some Egyptian food," *International*

- Journal of Microbiological Research*, vol. 6, no. 2, pp. 145–154, 2015.
- [25] L. Esteban-Tejeda, C. Prado, B. Cabal, J. Sanz, R. Torrecillas, and J. S. Moya, “Antibacterial and antifungal activity of ZnO containing glasses,” *PLoS One*, vol. 10, no. 7, article e0132709, 2015.
 - [26] C. Rode, M. Zieger, R. Wyrwa et al., “Antibacterial zinc oxide nanoparticle coating of polyester fabrics,” *Journal of Textile Science and Technology*, vol. 1, no. 2, pp. 65–74, 2015.
 - [27] A. S. Hameed, “A new coating for non-resorbable surgical suture,” *Journal of University of Babylon for Pure and Applied Sciences*, vol. 26, no. 1, pp. 301–307, 2018.
 - [28] Y. Song and J. Yang, “Preparation and in-vitro cytotoxicity of zinc oxide nanoparticles against osteoarthritic chondrocytes,” *Tropical Journal of Pharmaceutical Research*, vol. 15, no. 11, pp. 2321–2327, 2016.
 - [29] Y. Qian, J. Yao, M. Russel, K. Chen, and X. Wang, “Characterization of green synthesized nano-formulation (ZnO-A. vera) and their antibacterial activity against pathogens,” *Environmental Toxicology and Pharmacology*, vol. 39, no. 2, pp. 736–746, 2015.
 - [30] K. Elumalai and S. Velmurugan, “Green synthesis, characterization and antimicrobial activities of zinc oxide nanoparticles from the leaf extract of *Azadirachta indica* (L.),” *Applied Surface Science*, vol. 345, pp. 329–336, 2015.
 - [31] K. Ali, S. Dwivedi, A. Azam et al., “Aloe vera extract functionalized zinc oxide nanoparticles as nanoantibiotics against multi-drug resistant clinical bacterial isolates,” *Journal of Colloid and Interface Science*, vol. 427, pp. 145–156, 2016.
 - [32] V. G. Reshma and P. V. Mohanan, “Cellular interactions of zinc oxide nanoparticles with human embryonic kidney (HEK 293) cells,” *Colloids and Surfaces B: Biointerfaces*, vol. 157, pp. 182–190, 2017.
 - [33] K. Schilling, B. Bradford, D. Castelli et al., “Human safety review of ‘nano’ titanium dioxide and zinc oxide,” *Photochemical & Photobiological Sciences*, vol. 9, no. 4, pp. 495–509, 2010.
 - [34] W. Ji, D. Zhu, Y. Chen, J. Hu, and F. Li, “In-vitro cytotoxicity of biosynthesized zinc oxide nanoparticles towards cardiac cell lines of *Catla catla*,” *Biomedical Research*, vol. 28, no. 5, 2017.
 - [35] M. Madhumita, P. Guha, and A. Nag, “Bio-actives of betel leaf (*Piper betle* L.): a comprehensive review on extraction, isolation, characterization, and biological activity,” *Phytotherapy Research*, vol. 34, no. 10, pp. 2609–2627, 2020.
 - [36] A. Budiman, D. W. Rusnawan, and A. Yuliana, “Antibacterial activity of *Piper betle* L. extract in cream dosage forms against *Staphylococcus aureus* and *propionibacterium acne*,” *Journal of Pharmaceutical Sciences and Research*, vol. 10, no. 3, pp. 493–496, 2018.
 - [37] T. Nalina and Z. Rahim, “The crude aqueous extract of *Piper betle* L. and its antibacterial effect towards *Streptococcus mutans*,” *American Journal of Biotechnology and Biochemistry*, vol. 3, no. 1, pp. 10–15, 2007.
 - [38] R. Subashkumar, M. Sureshkumar, S. Babu, and T. Thayumanavan, “Antibacterial effect of crude aqueous extract of *Piper betle* L. against pathogenic bacteria,” *International Journal of Research in Pharmaceutical and Biomedical Sciences*, vol. 4, no. 1, pp. 42–46, 2013.
 - [39] C. Sarma, P. Rasane, S. Kaur et al., “Antioxidant and antimicrobial potential of selected varieties of *Piper betle* L. (betel leaf),” *Anais da Academia Brasileira de Ciências*, vol. 90, no. 4, pp. 3871–3878, 2018.
 - [40] B. Patra, M. T. Das, and S. K. Dey, “A review on *Piper betle* L. nature’s,” *Journal of Medicinal Plants Studies*, vol. 4, no. 6, pp. 185–192, 2016.
 - [41] S. Saini, “*Piper betle* L.: a review of phytochemical and pharmacological profile,” *International Education & Research Journal*, vol. 2, no. 2, pp. 81–83, 2016.
 - [42] U. Taukooorah, N. Lall, and F. Mahomoodally, “*Piper betle* L. (betel quid) shows bacteriostatic, additive, and synergistic antimicrobial action when combined with conventional antibiotics,” *South African Journal of Botany*, vol. 105, pp. 133–140, 2016.
 - [43] M. A. Rahman, M. T. Hossain, and M. A. Hamid, “Antibacterial activity of polyaniline coated silver nanoparticles synthesized from *Piper betle* leaves extract,” *Iranian Journal of Pharmaceutical Research*, vol. 15, no. 2, pp. 591–597, 2016.
 - [44] D. Ananda, S. T. Babu, C. G. Joshi, and M. Shantaram, “Synthesis of gold and silver nanoparticles from fermented and non fermented betel leaf,” *Internasional Journal of Nanomaterials and Biostructures*, vol. 5, no. 1, pp. 20–23, 2015.
 - [45] P. S. Praba, J. Jeyasundari, and Y. B. A. Jacob, “Synthesis of silver nano particles using *Piper betle* and its antibacterial activity,” *European Chemical Bulletin*, vol. 3, no. 10, pp. 1014–1016, 2014.
 - [46] S. P. Rao, K. Byrappa, N. Keerthiraj, J. Chatterjee, and M. S. Mustak, “Phyto-fabrication of ZnO nanoparticles using *Piper betle* aqueous extract and evaluation of its applicability in dentistry,” *Pharmaceutical Nanotechnology*, vol. 6, no. 3, pp. 201–208, 2018.
 - [47] L. Muruganandam, A. Krishna, J. Reddy, and G. S. Nirmala, “Optimization studies on extraction of phytochemicals from betel leaves,” *Resource-Efficient Technologies*, vol. 3, pp. 385–393, 2017.
 - [48] L. W. Foo, E. Salleh, and S. N. H. Mamat, “Extraction and qualitative analysis of *Piper betle* leaves for antimicrobial activities,” *International Journal of Engineering Technology Science and Research*, vol. 2, pp. 1–8, 2015.
 - [49] T. C. Sumon Das, “A review on green synthesis of Ag NPs and ZnO NPs from different plants extract and their antibacterial activity against multi-drug resistant bacteria,” *Journal of Innovations in Pharmaceutical and Biological Sciences*, vol. 5, no. 4, pp. 63–67, 2018.
 - [50] H. Agarwal, S. Venkat Kumar, and S. Rajeshkumar, “A review on green synthesis of zinc oxide nanoparticles - an eco-friendly approach,” *Resource-Efficient Technologies*, vol. 3, no. 4, pp. 406–413, 2017.
 - [51] M. Anbuvaran, M. Ramesh, G. Viruthagiri, N. Shanmugam, and N. Kannadasan, “*Anisochilus carnosus* leaf extract mediated synthesis of zinc oxide nanoparticles for antibacterial and photocatalytic activities,” *Materials Science in Semiconductor Processing*, vol. 39, pp. 621–628, 2015.
 - [52] S. Nagarajan and K. A. Kuppusamy, “Extracellular synthesis of zinc oxide nanoparticle using seaweeds of gulf of Mannar, India,” *Journal of Nanobiotechnology*, vol. 11, no. 1, pp. 1–11, 2013.
 - [53] M. Alavi, N. Karimi, and I. Salimikia, “Phytosynthesis of zinc oxide nanoparticles and its antibacterial, anti-quorum sensing, antimotility, and antioxidant capacities against multidrug resistant bacteria,” *Journal of Industrial and Engineering Chemistry*, vol. 72, pp. 457–473, 2019.

- [54] M. Alavi, N. Karimi, and T. Valadbeigi, "Antibacterial, anti-biofilm, antiquorum sensing, antimotility, and antioxidant activities of green fabricated Ag, Cu, TiO₂, ZnO, and Fe₃O₄NPs via *Protoparmeliopsis muralis* Lichen aqueous extract against multi-drug-resistant bacteria," *ACS Biomaterials Science and Engineering*, vol. 5, no. 9, pp. 4228–4243, 2019.
- [55] M. Balouiri, M. Sadiki, and S. K. Ibnsouda, "Methods for *in vitro* evaluating antimicrobial activity: a review," *Journal of Pharmaceutical Analysis*, vol. 6, no. 2, pp. 71–79, 2016.

Research Article

Determination of the Immunoglobulin G Spectrum by Surface-Enhanced Raman Spectroscopy Using Quasispherical Gold Nanoparticles

Alejandra Ortiz-Dosal ¹, Elizabeth Loredo-García,² Ana Gabriela Álvarez-Contreras,² Juan Manuel Núñez-Leyva,^{1,2} Luis Carlos Ortiz-Dosal,³ and Eleazar Samuel Kolosovas-Machuca ^{1,2}

¹Doctorado Institucional en Ingeniería y Ciencia de Materiales (DICIM-UASLP), Universidad Autónoma de San Luis Potosí, 550 Sierra Leona Ave., 78210 San Luis Potosí, SLP, Mexico

²Coordinación para la Innovación y Aplicación de la Ciencia y la Tecnología, Universidad Autónoma de San Luis Potosí, 550 Sierra Leona Ave., 78210 San Luis Potosí, SLP, Mexico

³Maestría en Ciencia e Ingeniería de los Materiales (MCIM-UAZ), Universidad Autónoma de Zacatecas, 801 López Velarde St., 9800 Zacatecas, Zac, Mexico

Correspondence should be addressed to Eleazar Samuel Kolosovas-Machuca; samuel.kolosovas@uaslp.mx

Received 19 September 2020; Revised 26 December 2020; Accepted 8 January 2021; Published 19 January 2021

Academic Editor: Sheng-Joue Young

Copyright © 2021 Alejandra Ortiz-Dosal et al. This is an open access article distributed under the Creative Commons Attribution License, which permits unrestricted use, distribution, and reproduction in any medium, provided the original work is properly cited.

Background. Immunoglobulins (Ig) are glycoprotein molecules produced by plasma cells in response to antigenic stimuli involved in various physiological and pathological conditions. Intravenous immunoglobulin (IVIG) is a compound whose composition corresponds to Ig concentrations in human plasma, predominantly IgG. It is used as a replacement treatment in immunodeficiencies and as an immunomodulator in inflammatory and autoimmune diseases. The determination of IgG concentrations is useful in the diagnosis of these immunodeficiencies. Surface-enhanced Raman spectroscopy (SERS) is a technique that allows protein quantification in a fast and straightforward way. **Objective.** This study is aimed at determining the Raman spectrum of IgG at physiological concentrations using quasispherical gold nanoparticles as a SERS substrate. **Methods.** We initially determined the Raman spectrum of IVIG at 5%. Subsequently, for SERS' characterization, decreasing dilutions of the protein were made by adding deionized water and an equal volume of the 5 nm gold quasispherical nanoparticle colloid. For each protein concentration, the Raman spectrum was determined using a 10x objective; we focused the 532 and 785 nm laser on the sample surface, in a range of 500-1800 cm⁻¹, with five acquisitions and an acquisition time of 30 seconds. **Results.** We obtained the IVIG spectrum using SERS up to a concentration of 75 mg/dl. The Raman bands correspond to aromatic amino acid side chains and the characteristic beta-sheet structure of IgG. **Conclusion.** The use of 5 nm quasispherical gold nanoparticles as a SERS substrate allows for detecting the Raman spectrum of IVIG at physiological concentrations.

1. Introduction

Immunoglobulins (Ig), also known as antibodies, are glycoprotein molecules produced by plasma cells in response to antigenic stimuli involved in various physiological and pathological conditions. The primary function of immunoglobulins corresponds to the adaptive immune response. They are subdivided, depending on the structure of the heavy

chains they contain, into several classes: IgM, IgG, IgD, IgA, and IgE. IgG is also subdivided into IgG1, IgG2, IgG3, IgG4 (decreasing order of abundance), and IgA in IgA1 and IgA2. IgG is the most abundant, with a plasma concentration of 700-1600 mg/dl, and constitutes 75 to 80% of all Ig. IgA corresponds to about 15%, with a plasma concentration of 70-400 mg/dl, while IgM's plasma concentration varies from 40 to 230 mg/dl. The determination of immunoglobulin

concentrations is useful in diagnosing immunodeficiencies and evaluating the response to treatment in these patients [1, 2].

Intravenous immunoglobulin (IVIG) is an immunoglobulin concentrate derived from thousands of healthy donors (no fewer than 3500). IgG plays a fundamental role in adaptive humoral immunity. Therefore, IVIG reflects the donor population's collective exposure to the environment and is expected to contain a repertoire of multiple specific antibodies against a broad spectrum of infectious agents (bacterial and viral), self-antigens, and anti-idiotypic antibodies.

The IVIG composition corresponds to the Ig concentrations in human plasma, mainly IgG, IgA, and traces of other Ig, cytokines, and soluble receptors.

IVIG is prepared using the Cohn-Oncley fractionation procedure, precipitating donor plasma with cold ethanol to enrich the IgG fraction, followed by chromatography purification [3]. Commercial products vary concerning the presence of excipients used to stabilize proteins and prevent the aggregation of IgG (sugars such as glucose, maltose, D-sorbitol, or amino acids such as glycine or proline), as well as the levels of sodium, pH, osmolality, and the presence of another Ig [4].

IgG comprises more than 90% of the different commercial IVIG preparations and is the main component required to observe this drug's therapeutic effects [5]. IVIG treatment is aimed at providing sufficient IgG antibodies that passively neutralize or opsonize a broad spectrum of infectious pathogens and trigger the activation of cell-mediated immunity. The indications for IVIG administration can be classified according to the mechanism of action and the underlying disease: replacement therapy in immunodeficiencies, immunomodulatory therapy (in hematological and organ-specific autoimmune diseases), an anti-inflammatory agent (in rheumatic, infectious, inflammatory, and neurological conditions).

Different doses are administered according to the medical condition being treated. In general, low doses are used in replacement therapies and higher doses when an immunomodulatory or anti-inflammatory effect is required [6].

Raman spectroscopy is a nanocharacterization technique based on the inelastic dispersion of molecular systems, which are illuminated with monochromatic radiation; it changes frequency due to the energy exchange that exists with the matter [7, 8]. Raman spectroscopy provides information on the primary, secondary, and tertiary structure of proteins by identifying associated characteristic bands. By allowing the structural characterization of proteins, it can detect pathological changes in them [9]. The application of the Raman characterization technique in biomedicine is an advance in the detection of biomarkers through noninvasive methods; however, it shows limitations because the signal from various proteins is weak. Due to this, the technique of surface-enhanced Raman spectroscopy (SERS) uses nanostructured surfaces of noble metals such as gold and silver. This technique allows the standard Raman scattering signal to be amplified in a factor from 10^4 to 10^{16} [10]. It has been used to diagnose some diseases and identify contaminants and pathogens, among other applications [8, 10, 11]. It is a non-destructive characterization technique that can be used in

aqueous media [12]. SERS could be an alternative to the ELISA test, an immunological assay in which an enzyme is used as a biomarker [13]. The first protein spectra reported were the spectra of hemoglobin and cytochrome C in 1972 [14]; later, spectra of other biological molecules were reported [15].

This study is aimed at determining the Raman spectrum of IgG (IVIG) using 5 nm quasispherical gold nanoparticles as a SERS substrate.

2. Material and Methods

We purchased intravenous normal human immunoglobulin 5% (Octagam® 5%, Octapharma Pharmazeutika Produktionsgesellschaft, m.b.H. Vienna, Austria). It contains 6 g of total protein, 95% unmodified IgG, 12 g of maltose, 600 μg of octoxynol (Triton X-100), 120 μg of tri-N butyl phosphate (TNBP), and 120 ml of injectable water. The antibody content is 0.5 IU per g of immunoglobulin. We kept it at a temperature of 4°C until use. The experiments were carried out at a temperature of 24°C, maintaining a pH in the colloidal suspension of 5.5 to keep it stable and avoid the protein's aggregation. We used deionized water (AE), with a resistivity $\geq 18.2 \text{ M}\Omega\cdot\text{cm}^{-1}$ at 25°C; and quasispherical gold nanoparticles (AuNPs), 5 nm in diameter, with a concentration of 5.5×10^{13} particles/ml, 0.052 mg/ml; and citrate coating (nanoComposix, Inc., San Diego, CA). Characterization of AuNPs are shown in Supplemental Material Section A. Raman experiments were conducted in a Horiba Jobin Yvon XploRA ONE Raman spectrometer coupled to an Olympus BX41 optical microscope, using a laser source at 532 nm (green) and 785 nm (red).

We initially determined the Raman spectrum of IVIG at 5 g/100 ml (5%). Subsequently, for SERS' characterization, dilutions of the protein were made in the mentioned concentration, adding deionized water and an equal volume of the nanoparticle colloid, as discussed below. When preparing the dilutions in this way, all samples have a final concentration of AuNPs of 0.026 mg/ml, and a total concentration of IVIG decreasing from 2.5% to 0.075%.

- (1) 20 μl IVIG 5% + 20 μl AE
- (2) 20 μl IVIG 5% + 20 μl AuNP 50 nm
- (3) 20 μl IVIG 5% + 20 μl AuNP 5 nm
- (4) 20 μl IVIG 2.5% + 20 μl AuNP 5 nm
- (5) 20 μl IVIG 1.25% + 20 μl AuNP 5 nm
- (6) 20 μl IVIG 0.62% + 20 μl AuNP 5 nm
- (7) 20 μl IVIG 0.31% + 20 μl AuNP 5 nm
- (8) 20 μl IVIG 0.15% + 20 μl AuNP 5 nm

We prepared each of the dilutions and immediately carried out the measurements without requiring additional incubation time. We placed the mixtures in an aluminum cell and obtained the SERS spectrum using a 785 nm laser, in a range of $500\text{--}1800 \text{ cm}^{-1}$, with five acquisitions and an

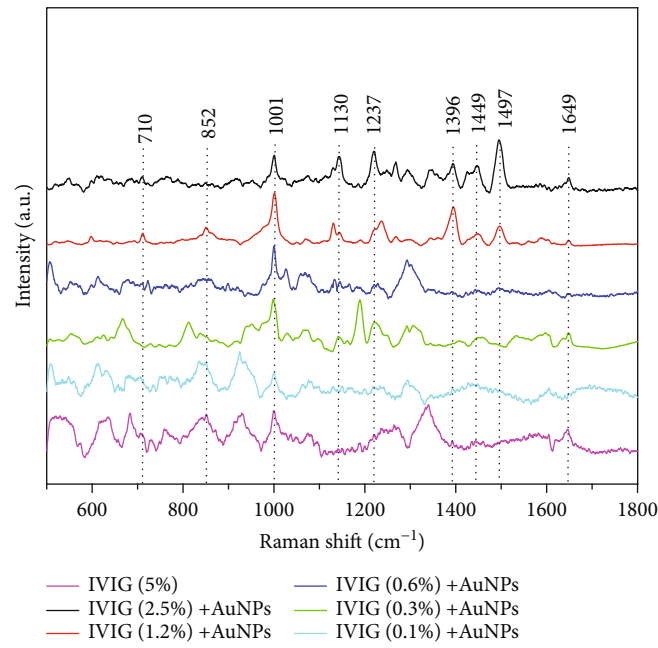


FIGURE 1: Characteristic Raman bands of the IVIG.

TABLE 1: Characteristic Raman bands of IVIG.

Raman shift (cm ⁻¹)	Proposed band assignment	Reference
710	Tyrosine (642, 640-650)	[17]
	Tryptophan (707)-in IgG-	[18]
	Carbon backbone ν (α -C, α -C β γ α -N) (870-1150)	[19]
	Glycine, alanine ν (CNC) (850-900) assigned to the symmetric CNC stretch mode	[20]
852	Tyrosine (852)-in IgG-	[21]
	Tyrosine (843) ν (ring)-in IgG-	[18]
	Tyrosine out of plane ring bending mode at 853	[22]
	Hydrogen bonding state of tyrosine	[23]
1001	Phenylalanine (1003, 1000-1010)	[17, 23]
	Symmetric breathing mode of phenylalanine (1003)	[22]
1130	Cysteine (CH bend) (1142)	[20]
	Glutamine (1122) (NH ₃ bend and rock modes)	[20]
	Amide III region (1230-1340) δ (N-H, α -H), ν (α -N)	[19]
	β -Sheet structure (1239)	[24]
1237	β -sheet structure, amide III (1230-1240)	[23]
	Glutamine (1225) (CH ₂ bend and twist)	[20]
	Tryptophan, tyrosine δ (ring) (1225)-in IgG-	[18]
	Amide III, β -sheet and random coils (1242)	[25]
1396	Histidine (1400-1420)	[17]
	Tryptophan ν ring stretching-in IgG-(1366)	[21]
	Tyrosine ν (ring) (1385)-in IgG-	[18]
	Glycine (1411) CH ₂ scissor mode	[20]
1449	Tryptophan CH ₂ scissors-in IgG-	[21]
	Tryptophan or δ (CH ₂) (1455)-in IgG-	[18]
	Glutamine (CH ₂ bend and scissors modes) (1462)	[20]
	C-H vibration (1449); CH functional groups in amino acid side chains of proteins	[25]
1497	Glycine (CH ₂ and OH bending modes) (1495)	[20]
	Tryptophan, tyrosine ν (ring) (1487)-in IgG-	[18]

δ : deformation; ν : stretching.

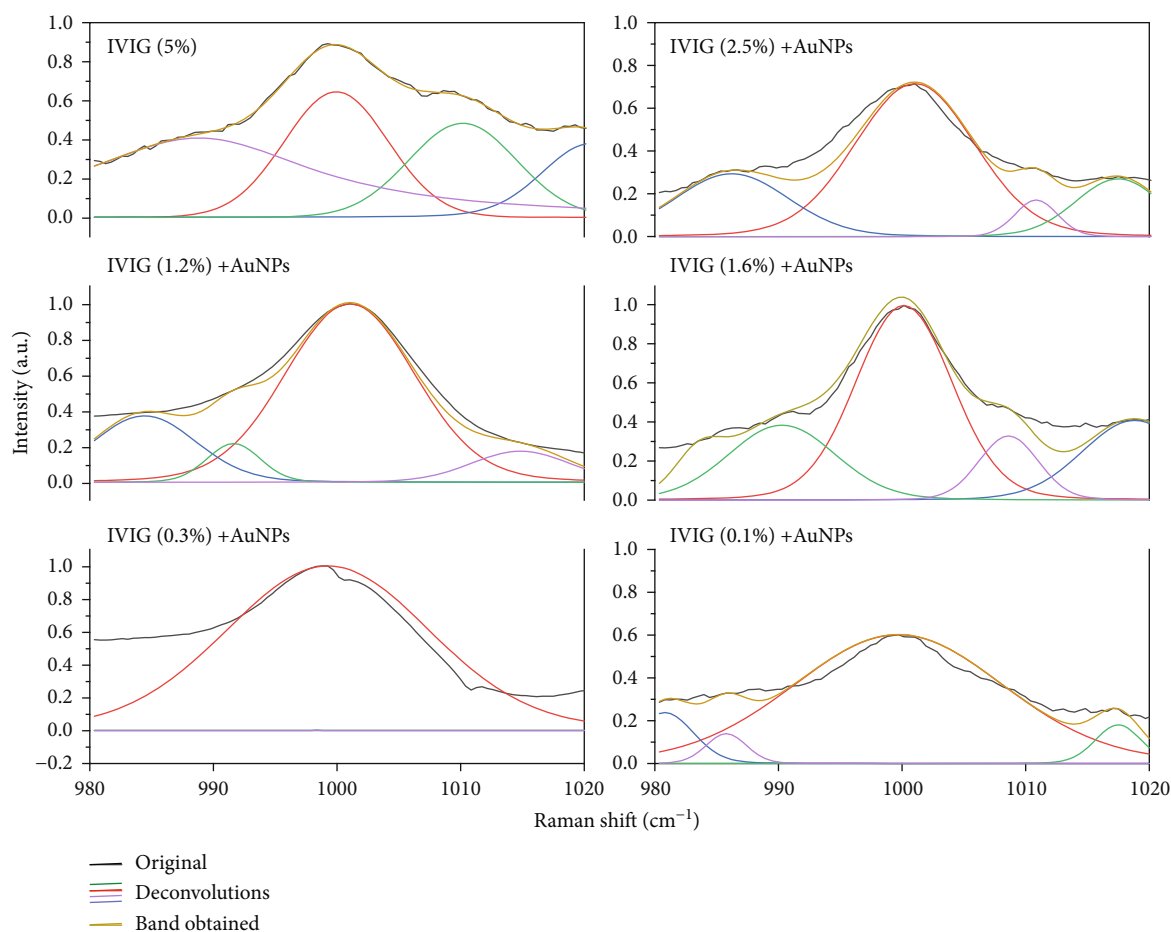


FIGURE 2: Deconvolutions of the IVIG Raman and SERS spectra were performed in the region of 980 to 1020 cm^{-1} . The band at 1001 cm^{-1} , corresponding to the phenylalanine ring, is shown in red.

acquisition time of 30 seconds. We focus the laser on the surface of the sample with a 10x objective.

We calculated the SERS enhancement factor in MatLab software using the estimation of surface-enhanced Raman spectroscopy (SERS) enhancement factor [16].

3. Results

It was possible to determine the IVIG spectrum by SERS up to a protein concentration of 0.075%, using quasispherical gold nanoparticles at 0.026 mg/ml and 785 nm laser. The characteristic Raman bands of the IVIG spectrum obtained are shown in Figure 1 and described in Table 1.

Signals from different molecules can constitute Raman bands [26]. In the spectrum, these bands may appear broadened, and therefore, the contribution of various components cannot be easily recognized, causing this to be misinterpreted as noise. In SERS, some signals that conform to the band may be more evident due to the amplification [27].

We perform a spectral truncate in the region of 980 to 1020 cm^{-1} . The band at 1001 cm^{-1} is consistent in all concentrations evaluated and corresponds to the phenylalanine ring's C-C bond. It is shown in red in Figure 2.

Using MatLab, we perform the calculation of the enhancement factor (EF). The values used are listed as follows: wavenumber (Raman Shift), Raman spectrum, SERS spectrum, characteristic Raman band (1001 cm^{-1}), the wavelength of the incident laser (785 nm), molecular weight of the molecule under test (150 g/mol), the density of the molecule (0.05 g/cm^3), the numerical aperture of the objective (0.471), and surface area of the molecule under test (27.7 nm). This calculation results in an $\text{EF} = 2.3726 \times 10^5$ (Supplemental Material Section B).

4. Discussion

The vibrations of the peptide structure in proteins are generally associated with three main regions in the Raman spectrum: (1) the region of carbon backbone (870-1150 cm^{-1}), comprising the narrowing corresponding to $\text{C}\alpha\text{-C}$, $\text{C}\alpha\text{-C}\beta$, and $\text{C}\alpha\text{-N}$, (2) the extended amide III region (1230-1340 cm^{-1}), which mainly involves the interface combination of the deformation in the NH plane and the narrowing of $\text{C}\alpha\text{-N}$, as well as a mixture between the deformations of NH and $\text{C}\alpha\text{-H}$, and (3) the amide I region (1630-1700 cm^{-1}) causes the C=O narrowing [20]. Aromatic amino acids are the dominant characteristics in the Raman spectrum of peptides and

proteins [22]. In fact, in previous work [18, 21], the spectrum of immunoglobulin G on silver surfaces was represented only by the side chains of aromatic amino acids; this is probably because, in the absence of carboxylate bonds, aromatic amino acids have a higher affinity for the metal surface than nonaromatic amino acids. In contrast, under our experimental conditions and using AuNPs as SERS substrate, it was possible to obtain Raman bands corresponding to the β -sheet conformation (1237 cm^{-1}), characteristics of the IgG protein secondary structure. Using Raman spectroscopy and amplifying the signal with 5 nm gold quasispherical nanoparticles, it was possible to determine the IVIG spectrum at a concentration of 0.075%, 75 mg/dl (normal range in healthy subjects 700–1600 mg/dl) [28]. So, it is possible to propose the use of SERS in the diagnosis of certain immunodeficiencies, for example, severe hypogammaglobulinemia (a condition in which IgG levels are less than or equal to 150 mg/dl and there is a lack of antibody response to vaccination), as well as in the evaluation of treatment after IVIG administration [29].

5. Limitations

This study has several limitations. We are determining the spectrum of purified IgG in an aqueous solution. For the SERS technique to be used in clinical laboratories, it will be necessary for the spectrum to be determined in complex mixtures, such as those found in human serum. Another limitation is that when found in serum, IgG could be associated with other molecules. These interactions may modify the spectrum of the protein when trying to obtain it in experimental models. This mixture with other molecules could also interfere with IgG interaction and the metallic nanoparticles used to amplify the Raman spectrum. Modifying the protein corona on the nanoparticles will indeed affect the spectrum obtained. Further research on this topic is required to consider in the future the application of the SERS technique in the clinical setting.

6. Conclusion

The use of 5 nm quasispherical gold nanoparticles as a SERS substrate allows the Raman spectrum of IVIG to be detected at a concentration ten times lower than normal levels.

Data Availability

The data that support the findings of this study are available from the corresponding author upon reasonable request.

Conflicts of Interest

All authors declare that they have no conflicts of interest.

Authors' Contributions

AOD, ELG, and ESKM conceived of the presented idea. AOD, ELG, JMNL, LCOD, and AGAC wrote the first version of the manuscript with support from ESKM. JMNL and LCOD developed the theory. ELG, ESKM, and AOD designed and performed the experiments. LCOD and AGAC

verified the analytical methods. AGAC, ESKM, and LCOD analyzed the data. All authors discussed the results and contributed to the final manuscript.

Supplementary Materials

Figure 1: TEM image of AuNPs at a 50 nm scale. Figure 2: TEM image of AuNPs at a 20 nm scale. Figure 3: TEM image of AuNPs at a 10 nm scale. Figure 4: optical spectra of the colloidal AuNPs. Figure 5: the size distribution of the obtained AuNPs through the DLS technique. Figure 6: IVIG SERS enhancement factor. (*Supplementary Materials*)

References

- [1] V. B. Arumugham and A. Rayi, "Intravenous Immunoglobulin (IVIG)," in *StatPearls [Internet]*, StatPearls Publishing, Treasure Island (FL), 2020.
- [2] A. A. Justiz Vaillant, Z. Jamal, and K. Ramphul, "Immunoglobulin," in *StatPearls [Internet]*, StatPearls Publishing, Treasure Island (FL), 2020.
- [3] R. L. Wasserman, D. Garcia, B. N. Greener et al., "Manufacturing process optimization of ADMA Biologics' intravenous immunoglobulin products, BIVIGAM®, and ASCENIV™," *Immunotherapy*, vol. 11, no. 16, pp. 1423–1433, 2019.
- [4] A. F. Barahona Afonso and J. CMP, "The production processes and biological effects of intravenous immunoglobulin," *Bio-molecules*, vol. 6, no. 1, 2016.
- [5] M. Radosevich and T. Burnouf, "Intravenous immunoglobulin G: trends in production methods, quality control, and quality assurance," *Vox Sanguinis*, vol. 98, no. 1, pp. 12–28, 2010.
- [6] E. E. Perez, J. S. Orange, F. Bonilla et al., "Update on the use of immunoglobulin in human disease: a review of evidence," *Journal of Allergy and Clinical Immunology*, vol. 139, no. 3, pp. S1–S46, 2017.
- [7] P. Vandenabeele, "Raman spectroscopy," *Analytical and Bio-analytical Chemistry*, vol. 397, no. 7, pp. 2629–2630, 2010.
- [8] B. Bravo, L. Ciani, and M. D'Acunto, "Raman spectroscopy and cancer diagnosis," *Proceedings*, vol. 27, no. 1, p. 15, 2019.
- [9] A. A. Bunaciu, H. Y. Aboul-Enein, and S. Fleschin, "Vibrational spectroscopy in clinical analysis," *Applied Spectroscopy Reviews*, vol. 50, no. 2, pp. 176–191, 2015.
- [10] R. R. Jones, D. C. Hooper, L. Zhang, D. Wolverson, and V. K. Valev, "Raman techniques: fundamentals and frontiers," *Nanoscale Research Letters*, vol. 14, no. 1, p. 231, 2019.
- [11] M. Chisanga, H. Muhamadali, D. I. Ellis, and R. Goodacre, "Surface-enhanced Raman scattering (SERS) in microbiology: illumination and enhancement of the microbial world," *Applied Spectroscopy*, vol. 72, no. 7, pp. 987–1000, 2018.
- [12] C. Chen, W. Liu, S. Tian, and T. Hong, "Novel surface-enhanced Raman spectroscopy techniques for DNA, protein, and drug detection," *Sensors*, vol. 19, no. 7, p. 1712, 2019.
- [13] M. Alhaji and A. Farhana, "Enzyme-linked immunosorbent assay (ELISA)," in *StatPearls*, StatPearls Publishing, Treasure Island (FL), 2020.
- [14] T. G. Spiro, "Resonance Raman spectroscopic studies of heme proteins," *Biochimica et Biophysica Acta (BBA) - Reviews on Bioenergetics*, vol. 416, no. 2, pp. 169–189, 1975.
- [15] J. De Gelder, K. De Gussem, P. Vandenabeele, and L. Moens, "Reference database of Raman spectra of biological

- molecules,” *Journal of Raman Spectroscopy*, vol. 38, no. 9, pp. 1133–1147, 2007.
- [16] R. Cabrera-Alonso, E. Guevara, M. G. Ramírez-Elías, B. Moncada, and F. J. González, “Detection of hydroquinone by Raman spectroscopy in patients with melasma before and after treatment,” *Skin Research and Technology*, vol. 25, no. 1, pp. 20–24, 2019.
 - [17] C. Mensch and C. Johannessen, “The influence of the amino acid side chains on the Raman optical activity spectra of proteins,” *Chemphyschem*, vol. 20, no. 1, pp. 42–54, 2019.
 - [18] E. S. Grabbe and R. P. Buck, “Surface-enhanced Raman spectroscopic investigation of human immunoglobulin G adsorbed on a silver electrode,” *Journal of the American Chemical Society*, vol. 111, no. 22, pp. 8362–8366, 1989.
 - [19] E. W. Blanch, L. Hecht, and L. D. Barron, “Vibrational Raman optical activity of proteins, nucleic acids, and viruses,” *Methods*, vol. 29, no. 2, pp. 196–209, 2003.
 - [20] S. M. Rolfe, M. R. Patel, I. Gilmour, K. Olsson-Francis, and T. J. Ringrose, “Defining multiple characteristic Raman bands of α -amino acids as biomarkers for planetary missions using a statistical method,” *Origins of Life and Evolution of the Biosphere*, vol. 46, no. 2-3, pp. 323–346, 2016.
 - [21] S. Stewart and P. M. Fredericks, “Surface-enhanced Raman spectroscopy of peptides and proteins adsorbed on an electrochemically prepared silver surface,” *Spectrochimica Acta Part A: Molecular and Biomolecular Spectroscopy*, vol. 55, no. 7-8, pp. 1615–1640, 1999.
 - [22] F. Wei, D. Zhang, N. J. Halas, and J. D. Hartgerink, “Aromatic amino acids providing characteristic motifs in the Raman and SERS spectroscopy of peptides,” *The Journal of Physical Chemistry B*, vol. 112, no. 30, pp. 9158–9164, 2008.
 - [23] N. Kuhar, S. Sil, T. Verma, and S. Umapathy, “Challenges in application of Raman spectroscopy to biology and materials,” *RSC Advances*, vol. 8, no. 46, pp. 25888–25908, 2018.
 - [24] X. Dou, Y. Yamaguchi, H. Yamamoto, S. Doi, and Y. Ozaki, “NIR SERS detection of immune reaction on gold colloid particles without bound/free antigen separation,” *Journal of Raman Spectroscopy*, vol. 29, no. 8, pp. 739–742, 1998.
 - [25] Z. Movasaghi, S. Rehman, and I. U. Rehman, “Raman spectroscopy of biological tissues,” *Applied Spectroscopy Reviews*, vol. 42, no. 5, pp. 493–541, 2007.
 - [26] S. Signorelli, S. Cannistraro, and A. R. Bizzarri, “Structural characterization of the intrinsically disordered protein p 53 using Raman spectroscopy,” *Applied Spectroscopy*, vol. 71, no. 5, pp. 823–832, 2017.
 - [27] B. R. Lutz, C. E. Dentinger, L. N. Nguyen et al., “Spectral analysis of multiplex Raman probe signatures,” *ACS Nano*, vol. 2, no. 11, pp. 2306–2314, 2008.
 - [28] C. Cunningham-Rundles, “How I treat common variable immune deficiency,” *Blood*, vol. 116, no. 1, pp. 7–15, 2010.
 - [29] H. Ho and C. Cunningham-Rundles, “Non-infectious complications of common variable immunodeficiency: updated clinical spectrum, sequelae, and insights to pathogenesis,” *Frontiers in Immunology*, vol. 11, 2020.

Review Article

Design and Synthesis of Nanostructured Materials for Sensor Applications

Naumih M. Noah 

School of Pharmacy and Health Sciences, United States International University-Africa (USIU-A), P.O. Box 14634-00800, Nairobi, Kenya

Correspondence should be addressed to Naumih M. Noah; mnoah@usiu.ac.ke

Received 21 August 2020; Revised 28 September 2020; Accepted 16 October 2020; Published 31 October 2020

Academic Editor: Sheng-Joue Young

Copyright © 2020 Naumih M. Noah. This is an open access article distributed under the Creative Commons Attribution License, which permits unrestricted use, distribution, and reproduction in any medium, provided the original work is properly cited.

There has been an increasing demand for the development of sensor devices with improved characteristics such as sensitivity, low cost, faster response, reliability, rapider recovery, reduced size, in situ analysis, and simple operation. Nanostructured materials have shown great potential in improving these properties for chemical and biological sensors. There are different nanostructured materials which have been used in manufacturing nanosensors which include nanoscale wires (capability of high detection sensitivity), carbon nanotubes (very high surface area and high electron conductivity), thin films, metal and metal oxide nanoparticles, polymer, and biomaterials. This review provides different methods which have been used in the synthesis and fabrication of these nanostructured materials followed by an extensive review of the recent developments of metal, metal oxides, carbon nanotubes, and polymer nanostructured materials in sensor applications.

1. Introduction

Nanostructures are materials which have a nanometer scale sizes in one, two, or three dimensions typically between 1 and 100 nm range [1–3]. They bring forth innovative material applications due to their superior physicochemical and plasmonic properties, and as such, they have generated a great deal of interest from basic scientific research to commercial development [1]. They have obtained prominence in technological developments due to their extraordinary physicochemical properties such as their melting points, electrical and thermal conductivities, light absorption and scattering properties, optical sensitivity, catalytic activity, and wettability resulting in their significantly enhanced performance over their bulk counterparts [2, 4]. These properties have enabled new applications ranging from energy conservation and structural strength enhancement to antimicrobial characteristics and self-cleaning surfaces as well as in sensor applications [1, 4]. Generally, nanostructures are divided into surface and bulk nanostructures, where the surface nanostructures refer to nanoscale patterns created on the surface

of a substrate while bulk nanostructures refer to individual nanomaterial's or an assembly of nanomaterial's [1]. There is a wide variety of nanostructured materials with different dimensions which range from zero-dimensional (0D) nanoparticles, one-dimensional (1D) nanorods and nanowires, two-dimensional (2D) nanosheets and films, three-dimensional (3D) polycrystals and ultraporous nanostructures, and nanoscaffolds [3, 5] as illustrated in Figure 1.

The most promising features of these structures are their size-dependent properties. For example, metallic nanoparticles exhibit tunable radiation and absorption wavelength depending on their aspect ratio [6] and coating [7]. These unique properties are attributed to the phenomenon called localized surface plasmon resonance (LSPR). Each particle can effectively produce photoluminescence equivalent to a million dye molecules. Additionally, they are photo stable and do not suffer from photo bleaching [8]. Owing to their superior optical properties, they can produce better signal over ordinary dye molecules. After coating with probe molecules, the optical properties of nanostructures allow the detection of specific target molecules. Numerous physical and chemical

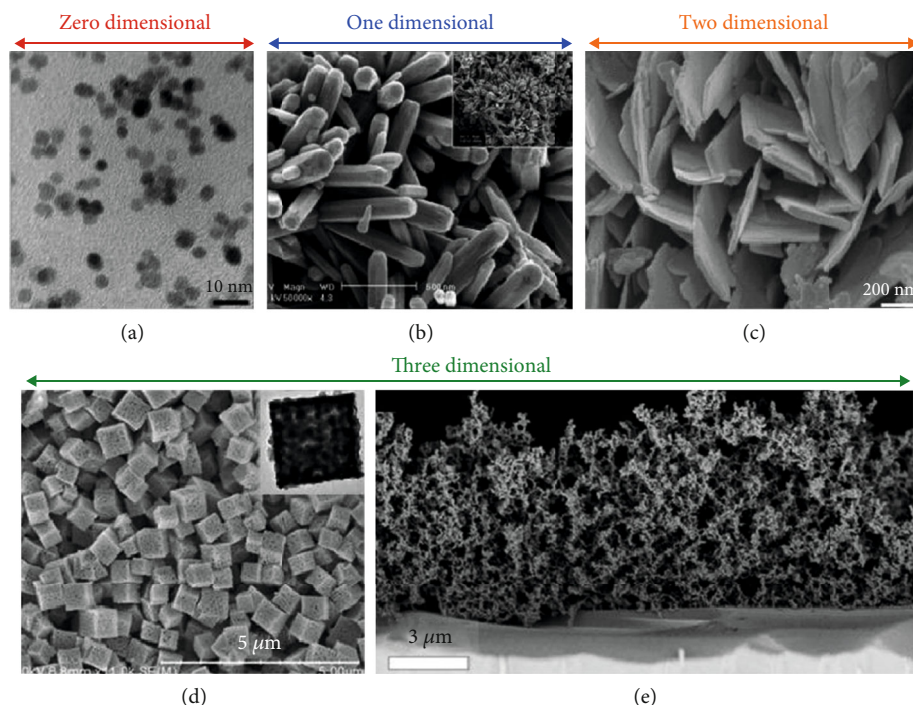


FIGURE 1: (a) Typical TEM image of ZnO quantum dots (QDs) obtained through a wet synthesis method. (b) SEM images of ZnO nanorods. (c) SEM image of ZnO nanosheets formed through a simple mixed hydrothermal synthesis method. (d) SEM images of acid-washed porous SnO_2 microcubes after calcination at 900°C for 2 h. Inset: TEM image of the as-prepared porous SnO_2 microcubes. (e) ZnO ultra porous film made by flame spray pyrolysis. Adapted from [5], an open access article.

methods have been developed for the fabrication of nanostructured materials [9–12], and they are described in the next section.

2. Fabrication of Nanostructured Materials

Various syntheses and processing techniques have been established for the fabrication of nanostructured materials with a higher degree tailored specifically to the material to be produced which might be considered to be more restrictive than the conventional production methods [13]. Generally, the fabrication of nanostructured materials is considered to proceed via two main strategies which include the “bottom-up” and “top-down” approaches [1, 13]. The difference between these two general strategies is based on the processes involved in the construction of the nanostructures [14]. In the bottom-up approach, a structure is normally built up of small units while in top-down approach, a larger unit is reduced in size to a finished structure [1] as shown in Figure 2. While the top-down approach comprises a few viable fabrication techniques which stem from experience and technology developed in other industries, many fabrication methods use the bottom up approach where building blocks of nanoparticles or clusters are first prepared by an appropriate technique and then assembled into composites, coatings, and layers or consolidated into bulk under well-controlled conditions [13]. The fabrication of nanostructured materials can also be achieved through a combination of the two approaches which are discussed in more details below.

2.1. Top-Down Approach. In top-down approach, large materials are normally deconstructed by a chain of physical and chemical processes [1, 3, 14]. The physical top-down approach employs the use of photons, electrons, and ions while the chemical top-down strategy relies essentially on chemical reactions that are brought about by chemical etchants or by application of heat [14]. This approach can be used to fabricate a varied selection of devices with high reliability and integrity and is therefore common in the semiconductor device industry [3]. Many novel structures such as nanowires which can be used to detect biological samples without labelling have been fabricated using this approach [15]. Nanopores used to detect and measure biophysical properties of deoxyribonucleic acid (DNA), proteins, and other molecules passing through the nanopores have also been fabricated using the top-down approach [16]. The basic fabrication steps in top-down approach include (i) lithography, (ii) laser ablation, (iii) chemical etching, (iv) milling process, and (v) thermal decomposition which are described in more details below.

2.1.1. Lithography. Lithography is a physical top-down approach which employs the use of photons (optical lithography), electrons (electron beam lithography), and ions (ion beam lithography) to fabricate nanostructures [14]. It has been a method of choice for producing patterned nanostructures in the microelectronics industry since it transfers a pattern from a mask on a substrate [3, 14]. The most common method is optical lithography which uses ultraviolet light to transfer the desired pattern from a mask to a light-sensitive

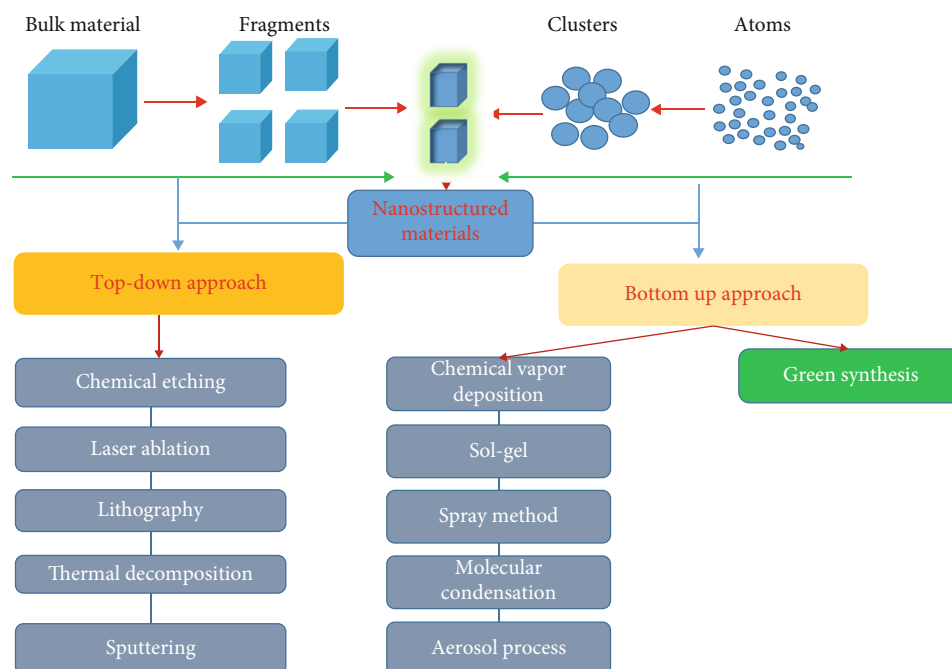


FIGURE 2: A schematic representation of the top-down and bottom-up approaches for the fabrication of nanostructures.

material known as photoresist that coats the semiconductor substrate [3, 14]. The substrate undergoes changes in chemical composition when exposed to a specific wavelength of light through the mask to create a pattern which is subsequently transferred to the substrate often by etching [1, 3, 14] as illustrated in Figure 3. Electron beam lithography on the other hand uses electrons instead of photons to achieve nanostructures at a resolution beyond the diffraction limit of light [14, 17]. It is a maskless techniques which generates the pattern directly using a tightly focused beam of accelerated electrons to scan the substrate coated with an electron-reactive resist [14]. The ion beam lithography [18] and laser writing [19] are also maskless approaches which use a focused beam of high energy ions and multiphoton absorption-induced photochemical transformation of the photoresist, respectively.

2.1.2. Chemical/Template Etching. This is a subtractive chemical top-down nanofabrication technique that selectively removes materials from a substrate. It uses a template to direct the chemical etching of a substrate resulting to a nano-scale pattern crafted on the substrate surface. The etching can be done in dry or wet conditions [3, 14]. For example, a silicon substrate as shown in Figure 4 [20] has been fabricated using a block of copolymer template prepared by spin coating a solution of a copolymer consisting of a poly-(4-vinylpyridine) core and a polystyrene corona prepared in toluene on the silicon substrate [14, 20]. Upon spin coating, the amphiphilic polymer micelles of the copolymer spontaneously self-assembled into a monolayer of pseudohexagonal array on the substrate surface, forming the template [14, 20]. The nano-scale pattern of the polymer template is then transferred to the underlying substrate by selective etching with an aqueous solution of hydrofluoric acid (HF) [14, 20]. Fluoride-based

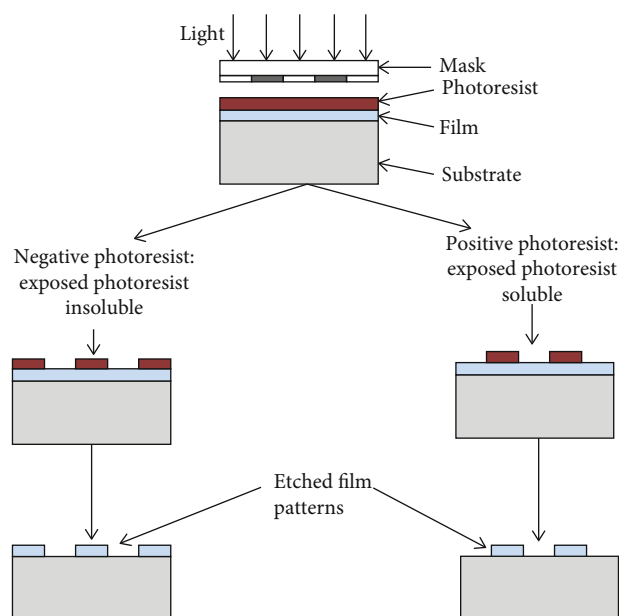


FIGURE 3: A schematic representation of optical lithography using negative and positive photoresist [3].

etching of the silicon surface takes place exclusively beneath the poly-(4-vinylpyridine) cores due to the protonation of the pyridyl groups by HF that results in selective localization of fluoride ions within the micellar cores [14, 20]. The silicon etch pit array is finally obtained after removal of the polymer template through ultrasonication in toluene [20]. The resulting etched features on the silicon surface can be functionalized with other materials (e.g., gold nanoparticles), allowing for the generation of more complex architectures [20, 21].

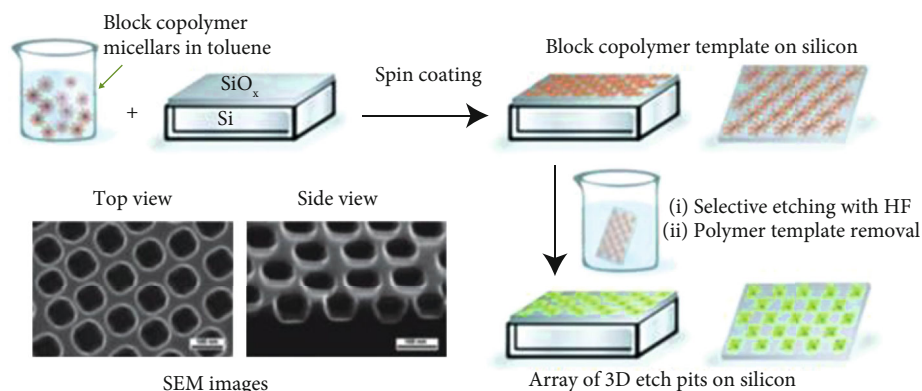


FIGURE 4: A schematic diagram representing the fabrication of a 3D etch pit array on silicon using a block copolymer as a template and an aqueous solution of hydrofluoric acid (HF) as an etchant. SEM images displaying the etch pit arrays on silicon are also shown (scale bar = 100 nm). Adapted with permission from ref. [20]. Copyright © 2007, American Chemical Society.

2.1.3. Thermal Decomposition. Thermal decomposition also known as thermolysis is a process where heat is used to separate chemical bonds in a compound [14]. This process provides a simple one-step strategy to fabricate nanostructures with controlled porosity which is an advantage as compared to other methods. This method was demonstrated by Yu and team where they used it to fabricate nanoporous cadmium oxide (CdO) from cadmium carbonate (CdCO_3) microcrystals [22]. In their work, high-quality CdCO_3 microcrystals were transformed as they were continuously heat treated at 500°C for 30 minutes. This led to a decomposition process which began at the sharp edges and corners and continued to the flat surfaces of the crystals resulting in a core-shell microstructure wherein the newly formed CdO densely coated the partially decomposed CdCO_3 crystals releasing carbon dioxide (CO_2) [22] as illustrated in Figure 5. As thermolysis continued, more and more CO_2 molecules accumulated inside the microstructure until the pressure was high enough that tiny pores nucleated to allow the escape of the trapped gas. These tiny pores eventually grew into continuous channels as the decomposition of CdCO_3 went to completion [22].

2.1.4. Selective Dealloying. Selective dealloying normally produces nanoporous metals by utilizing chemical or electrochemical reactions to remove the most chemically active metal in the alloy. As the less noble metal is removed, atoms of the more noble metal reorganize into a 3D network of pores/channels and ligaments [14].

2.1.5. Mechanical Milling. A mechanical milling technique has been utilized to produce amorphous and nanocrystalline alloys as well as metal/nonmetal nanocomposite materials by milling and post annealing, of elemental or compound powders in an inert atmosphere [23]. It is a nonequilibrium processing technique whereby different elemental powders are milled in an inert atmosphere to create one mixed powder with the same composition as the constituents [23]. Mechanical milling has been utilized to synthesize various nanoalloys and many nanocomposites in very high yield. The mechanical milling has been utilized for the synthesis of nanomater-

ials either by milling and postannealing or by mechanical activation and then applying some other process on these activated materials [23].

2.2. Bottom-Up Approach. The bottom-up approach involves the assembly of the building blocks (atoms or molecules) into nanostructured arrays due to attractive forces [1, 3, 24]. This approach has the potential to generate functional multicomponent devices by self-assembly of the atoms and molecules without wasting them or the need for eliminating parts of the system [17]. The assembly of the elementary building blocks is usually manipulated by either physical aggregation, chemical reaction, or use of templates [3, 24] where controlled chemical reactions manipulate the building blocks to self-assemble and make nanostructures such as nanotubes, nanoribbons, and quantum dots [1, 25, 26]. This approach has the potential to assemble nanostructured materials where the top-down approach fails though one of its major challenges is to ensure predefined structures with precise shapes and sizes [3]. Some of the most common bottom-up nanofabrication methods are described below.

2.2.1. Chemical Vapor Deposition. Chemical vapor deposition (CVD) is a process where a substrate is exposed to one or more volatile precursors, which react and/or decompose on the surface of the substrate to produce a thin film deposit [27, 28]. By changing various experimental conditions such as the substrate material, substrate temperature, and composition of the reaction gas mixture, total pressure gas flows and other materials with a wide range of physical, tribological, and chemical properties can be produced [27, 28] as illustrated in Figure 6 [29]. All chemical vapour deposition reactions involve a number of steps. The main steps are as follows: precursor, generation of active gaseous reactant species; transport, delivering the precursor into the reaction chamber; adsorption of the precursor onto the hot surface; decomposition of the precursor to give the atom needed for the film and organic waste; migration of atoms to a strong binding site; nucleation that leads to the growth of the thin film; desorption of unwanted side products; and removal of unwanted products [30, 31]. However, it is possible to

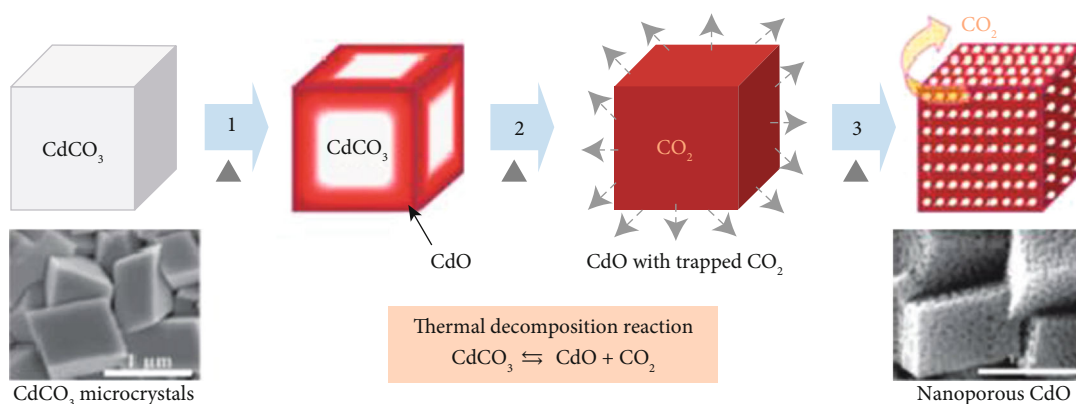


FIGURE 5: A schematic illustration of the mechanism of formation of nanoporous CdO upon thermal decomposition of high-quality CdCO₃ microcrystals at 500°C for 30 min. Also shown are the SEM images of the starting CdCO₃ microcrystals and the resulting nanoporous CdO (scale bar = 1 mm). Reproduced with permission from ref. [22]. Copyright © 2007, American Chemical Society.

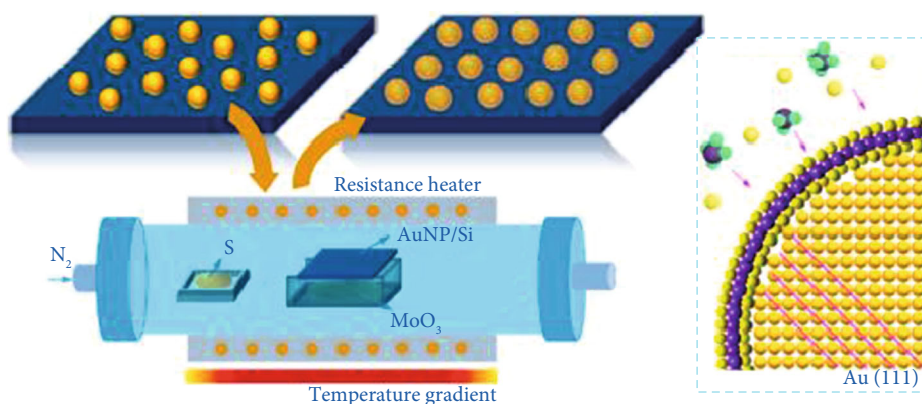


FIGURE 6: A schematic representation of CVD process of MoS₂ shell growth on Au nanoparticles. Reproduced with permission from [29]. Copyright © 2020, American Chemical Society.

achieve this in two steps especially using rotary chemical vapor deposition (RCVP) [32]. This method has an excellent throwing power which enables the production of coatings of uniform thickness and properties with a low porosity [26, 27]. This method is also capable to offer localized, or selective deposition, on patterned substrates [27, 28]. CVD processes are employed in many thin film applications, such as dielectrics, conductors, passivation layers, oxidation barriers, conductive oxides, tribological and corrosion-resistant coatings, heat-resistant coatings, and epitaxial layers for microelectronics [27]. They are also used in the preparation of high-temperature materials (tungsten, ceramics, etc.) and the production of solar cells, high-temperature fiber composites, and particles of well-defined sizes [26, 27]. CVD techniques have been developed to produce 2D nanosheets, such as graphene [33], h-BN nanosheets [34], metal carbides [35], and borophenes [36] among others.

2.2.2. Sol-gel Nanofabrication. Sol-gel is a wet-chemical process that involves the formation of an inorganic colloidal suspension (sol) and gelation of the sol in a continuous liquid phase (gel) to form a three-dimensional network structure [37]. In sol-gel nanofabrication, a metal precursor in solution is deposited on suitable substrates and then heat treated to

cause oxidation and/or sintering of the final products [17] as illustrated in Figure 7 [38]. It has been widely used for the fabrication of nanostructured functional metal oxide materials and alloys because it is cost effective and it offers the superiority of chemical reaction at molecular level, which is favorable to improve the chemical homogeneity of the final products [17, 39–42]. This process allows for the synthesis of pure and homogenous ceramic materials by means of preparation techniques different from the traditional process of fusion of oxides [43] which makes this method to stand out. By capping the particles with appropriate ligands, the dispersion can be stabilized in this liquid phase synthesis. For example, Moncada and coworkers reported the preparation of hybrid layered aluminosilicate nanoparticles (NPs) containing octadecyl amine (ODA) as the organic part and SiO₂ NPs with spherical morphology containing ODA or without ODA by the sol-gel method and used for the formation of nanocomposites with polypropylene [43, 44].

2.2.3. Laser Pyrolysis Synthesis. Laser pyrolysis involves resonant energy transfer between laser photons and a gaseous species, reactant, or sensitizer [45]. This technique is commonly categorized as a vapor-phase synthesis process utilized for producing a nanomaterials (NMs) [43, 46]. In a typical

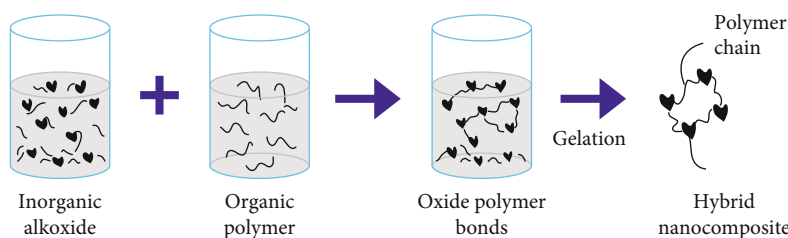


FIGURE 7: A schematic representation of sol-gel synthesis [38].

laser pyrolysis process, the gaseous-phase precursors are introduced to a chamber by a carrier gas (e.g., argon) where the gaseous-phase precursors meet the laser beam. The high-power laser beam (e.g., 2400 W) generates elevated localized temperatures which trigger the nucleation and growth of nanoparticles [43, 45]. The nanoparticles are then collected by a catcher equipped with a filter.

2.2.4. Green Synthesis. Green synthesis uses reducing agents obtained from plant extracts to reduce aqueous species of the metal in solution. An example is the reduction of Ag^+ from an aqueous solution of AgNO_3 using plant extracts such as *Clitoria ternatea*, plants (green tea (*Camellia sinensis*), alfalfa (*Medicago sativa*), lemongrass (*Cymbopogon flexuosus*), and geranium (*Pelargonium graveolens*)) [47], Citrus paradisi (Grapefruit red) [48], and *Solanum nigrum* as reducing agents [49]. Other biological agents such as bacteria (*Pseudomonas stutzeri* AG259, *Lactobacillus* strains, etc.), fungi (*Fusarium oxysporum*, *Aspergillus flavus*), and algae (*Lyngbya majuscula*, *Spirulina subsalsa*, *Rhizoclonium hieroglyphicum*, and *Chlorella vulgaris*) may also be used as reducing agents for silver [47]. These agents present cost-effective and environmentally friendly pathways for nanoparticle synthesis. Silver nanoparticles, like magnesium oxide nanoparticles, exhibit antimicrobial properties [50]. The antimicrobial activity results from the interaction of silver ions with sulphuric groups in the cell membranes of bacteria and other microorganism [51]. Pure silver nanoparticles are characterized by high toxicity and low stability, an aspect that limits their antimicrobial activity and consequently their application in water purification systems. For this reason, synthesis of silver nanoparticles for water filtration is designed in such a way that they are stabilized through surface engineering, impregnated with other materials placed on substrates [52]. Some of the substrates that support silver nanoparticles include sand, zeolites [53], fiberglass [54], activated carbon [55], blotter paper [56], cellulose filters [57], ceramic filters [58], or polyurethane foams [59] among others. Materials used for impregnation of silver nanoparticles include polyamide-66 [60] and chitosan [48] among others. Some stabilizing agents are amine functionalized hydrosoluble silicone wax [60], chitosan, gelatin hydrogel [61], or dithiocarbamate ligands [62].

3. Characterization of Nanostructures

The most common characterization of nanostructures is in terms of shape and morphology and due to their exceedingly

small size, dedicated tools and special techniques are usually required [1]. This information is usually obtained by various imaging techniques. For example, X-ray diffraction spectroscopy is usually used to give information on the crystalline structure of the nanostructured material synthesized and to determine the particle size. It therefore presents a suitable technique for studying size modulation of nanoparticles as a function of changes in dopants, temperature, and synthesis time among other parameters [63]. Further, changes in the crystallinity of synthesized nanostructures with changing degree of doping can be studied using Raman spectroscopy. This is inferred from changes in the vibration modes of the nanomaterial as a result of structural distortions (surface defects) caused by various dopant compositions. The changes may include signal resolution, broadening, or shifting [64]. Likewise, transmission electron microscopy (TEM) and scanning electron microscopy (SEM) can provide microstructural elucidation with varying dopant percentages and also give an estimate of the particle sizes [65]. Furthermore, both TEM and SEM can offer information on the level of aggregation or nonaggregation of the synthesized nanostructures. For instance, it is found that synthesized MnFe_2O_4 form aggregates but when coated with a Mn-Co oxide layer, the nanoparticles become nonaggregated [66].

X-ray photoelectron spectroscopy (XPS) is another technique used in the characterization of nanostructures to provide their atomic composition. Since the properties of nanomaterials can significantly be modified by altering atomic composition of the core material or the dopant, the use of XPS can enable one to optimize the respective ratios of each species in the nanomaterial. A further understanding of inner architectural properties of nanocomposites is important since they determine the amount of adsorption sites available. These can be inferred from the study of microporosity and specific surface areas using suitable adsorption isotherms such as the Langmuir adsorption isotherm, Freundlich adsorption models, or Brunauer-Denig-Denig-Teller [63, 65]. To probe the interaction between nanostructures and bacteria, atomic force microscopy (AFM), transmission electron microscopy (TEM), and laser confocal microscopy (LCM) are used. This is confirmed by observing changes in the integrity of the cell membranes, resulting in the death of the bacteria. Inductively coupled plasma mass spectrometry (ICP-MS) may be used to quantify the concentration of silver ions leached from the nanocomposite matrix after a specified contact time with water samples containing the target microorganism [60]. Fourier transform infrared (FTIR) is also used to study the chemical interaction of various

functional groups during synthesis and also to confirm successful surface modification of the nanocomposites [67].

4. Application of Nanostructures in Sensors

A sensor is a device which can detect variable quantities, usually electronically, and converts the measurement into specific signals [68, 69]. The most important requirements of sensors are diversity, sensitivity, accuracy of information extracted, selectivity, and stability [68] which can enable us to monitor the environment around us and to use that information for different purposes [69]. There has been an increasing demand for the development of new sensor devices with specific characteristics such as improved sensitivity, low cost, faster response, reliability, rapider recovery, reduced size, in situ analysis, and simple operation [70] [71, 72]. Nanostructured materials have shown great potential in improving these properties for chemical and biological sensors [73]. Various nanostructured materials have been used in manufacturing nanosensors. For example, nanoscale wires (capability of high detection sensitivity), carbon nanotubes (very high surface area and high electron conductivity), thin films, metal and metal oxide nanoparticles, polymer, and biomaterials [74]. Since very many nanostructured materials have been used in sensors, in the next section, we provide an extensive review of the recent developments of metal, metal oxides, carbon nanotubes, and polymer nanostructured materials in sensors.

4.1. Metal Nanostructures in Sensors. Metal nanoparticles are known to have unique physical and chemical properties which make them extremely suitable for designing new and improved sensing devices especially electrochemical sensors and biosensors [75, 76]. Various metal nanoparticles such as gold (Au), silver (Ag), platinum (Pt), palladium (Pd), copper (Cu), and cobalt (Co), including rare earth metals, have been used in fabricating electrochemical sensors and biosensors, and they normally play different roles in diverse sensing systems [75]. The importance of these roles includes the immobilization of biomolecules, the catalysis of electrochemical reactions, and the enhancement of electron transfer between electrode surfaces and proteins, labeling biomolecules as well as acting as a reactant [75]. Metal nanoparticles can be used as analytical transducers in various sensing principles as well as signal amplification elements [77]. The combination of greatly resourceful nanoparticle sensing principles with recognition elements has resulted in bioassays with fast responses and visual outcome, appropriate for use in resource constrained environments [77]. For example, silver and gold nanoparticles have been used in the development of biosensors for point of care disease diagnosis [12].

The interparticle plasmon coupling of the nanoparticles leads to color changes which have been widely used in biosensors based on aggregation of the nanoparticles. For example, small gold nanoparticles are red and well dispersed but turn blue or purple on aggregation [78] while silver nanoparticles are yellowish brownish when dispersed but turn black when they aggregate [79]. The fundamental property of these nanoparticles has been used in the development of colorimetric sensor arrays with the potential of rapidity of analysis,

which are cost effective and easy to use since they can provide naked eye observations [80]. A number of biosensors based on this predictable color changes such as biosensors for detection of α -1-fetoprotein [81], antihepatitis B virus antibodies in human serum [82], breast cancer biomarkers [83], mycobacterial of the *Mycobacterium tuberculosis* complex [84], human immunodeficiency virus type 1 DNA [85], toxic metal pollutants [86], and organochlorine endosulfan pesticide (ESP) [87] as shown in Figure 8 have been developed.

Graphene sheets which were decorated with green synthesized gold nanoparticles have been reported for label-free electrochemical impedance hybridization sensing of biomolecules such as HCG hormone in pregnant women due to their plasmon resonance [88–90]. By mixing 500 μ l of biosynthesized gold nanoparticle solution with the same volume of the test sample and testing the solution using a pregnancy test strip, the authors found that the gold nanoparticles changed color into pink when pregnancy was positive and gray when negative. They further claimed that the method was 100% accurate for pregnancy diagnosis and can be used as an alternative method for a urine pregnancy test [89, 90].

Gold nanoparticles synthesized from patuletin isolated from *Tagetes patula* which was used as a capping and reducing agent as reported by Muhammad et al. were used as a chemosensor for piroxicam. In their work, they conjugated the gold nanoparticles with the patuletin, and the conjugate was found to be 63.2 by weight. They then examined the conjugate as a potential chemosensor with different drugs, but only one drug, piroxicam, was found to quench luminescence which followed Beer's law in a concentration range of 20–60 μ M. The quenching was also found to be stable at different pH, elevated temperatures, or addition of other drugs, and hence, they concluded that it could be important for molecular recognition applications [91].

Green synthesized silver nanoparticles from the aqueous solution of polysaccharide of guar gum (*Cyamopsis tetragoloba*) plants displayed exceptional optical property towards ammonia with a very short response time of between 2 and 3 seconds and a detection limit of 1 ppm at room temperature [92, 93], and hence, this optical property towards ammonia at can be used as a sensor for the detection of ammonia level in biological fluids such as plasma, saliva, cerebrospinal liquid, and sweat [92, 93]. Silver nanoparticles embedded in polymers have also been used in sensors as reported in a study by Kariuki and coworkers [94] where they embedded silver nanoparticles in poly (amic) acid (PAA) polymer matrix (PAA-Ag NPs) for the detection of nitrobenzene. They found that the PAA-Ag nanoparticles based sensor showed a detection limit of 1.68 mM with a wide linear range of 10–600 mM and a high sensitivity of 7.88 mA mM⁻¹ with low interference on structurally similar nitroaromatic compounds [94].

Silver nanoparticles can also enable sensing of various analytes by tagging them with the nanoparticles. In a study reported by Sepunaru et al. [95], silver nanoparticles were used to tag influenza virus which led to efficient electrochemical detection of the virus since the magnitude and frequency

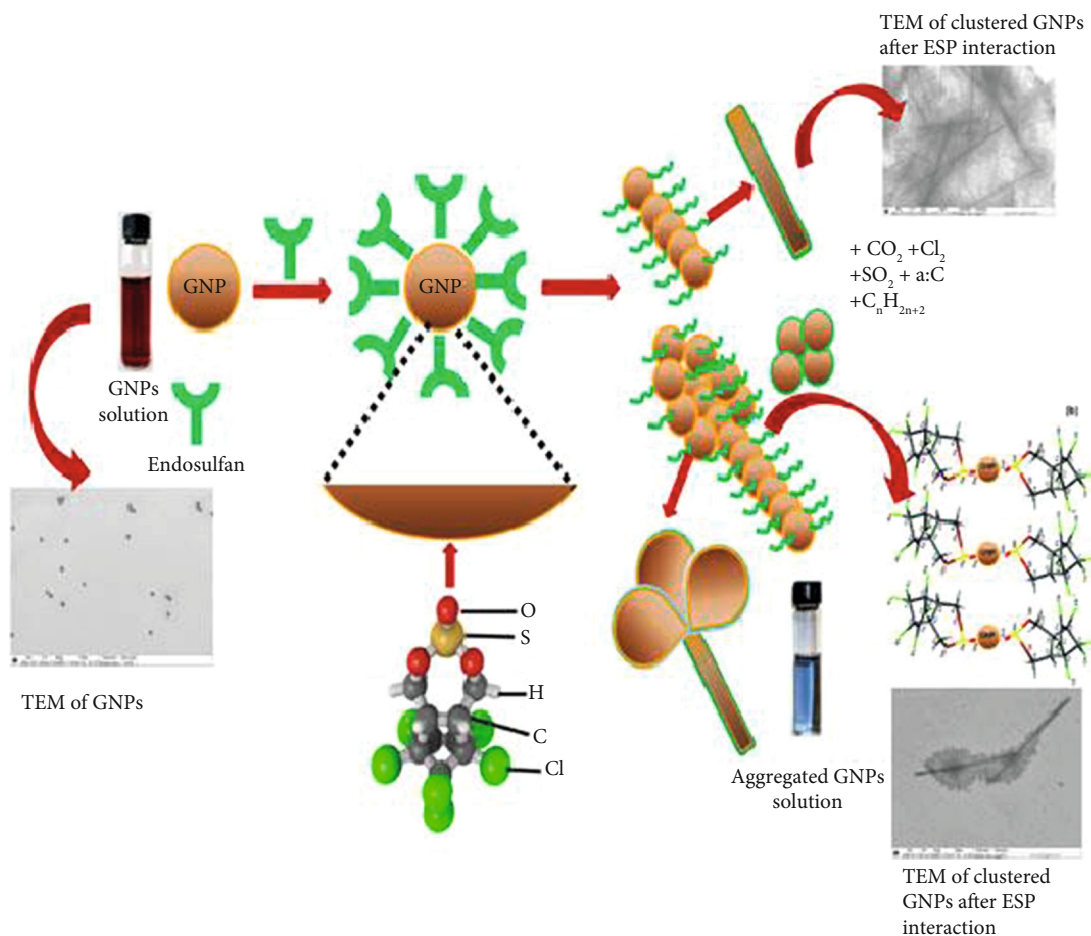


FIGURE 8: A diagram showing gold nanoparticles (GNPs) of ~8 nm in diameter used for the detection of organochlorine endosulfan pesticide (ESP) as colorimetric sensor and the design of GNP-based chemical sensor for its quantitative estimation has also been proposed. The original wine red color of GNPs changes into various shades of blue after the addition of different concentrations of ESP solutions. A GNP-based sensing electrode has been used for designing of ESP detection chemical sensor at ambient temperature. Adapted with permission from [87]. Copyright © Materials Research Society 2018.

of the current increased linearly with the increasing virus concentration as well as the increasing surface coverage of the silver nanoparticles [95].

Platinum nanoparticles usually reveal good catalytic properties and have also been used in sensors or various analytes. For example, they have been used in sensors developed for the detection of hydrogen peroxide [96–99], cholesterol [100], mercury ions [101], and hydrogen [102].

Palladium nanoparticles are also characterized by their extensive catalytic properties and hence have found sensor applications towards gases, biomolecules, and hazardous toxic molecules [74]. Palladium nanoparticle-based materials are said to exhibit high electrocatalytic activity towards different target analytes. Palladium is also abundant over other noble metals such as platinum and gold, and this is making it a cheaper substitute for developing a number of electrochemical sensors [74]. Palladium in combination with other materials such as graphene forms nanocomposites which have been found to improve the mass diffusion of analytes. The nanocomposites normally offer electron tunneling which enables electron transfer between the active site and the elec-

trode hence leading to effective electrochemical sensing performance [74]. A nanocomposite of pd and pt has been used to develop a sensor for nitrite [103, 104]. Another study reported a nanocomposite of palladium nanoparticles with polypyrrole which was used to develop a sensor for the detection of nitrates [105], while another study reported a nanocomposite of palladium nanoparticle with polyvinylpyrrolidone to detect hydrogen peroxide [106].

Copper is also another metal which has fascinated many researchers as an ideal material for use in sensors since it has good stability, outstanding electrical conductivity, electrocatalytic properties, and low cost when compared with noble metal such as platinum, gold, and silver [74]. Copper-based nanostructured materials have very many exceptional properties which include high mass-transport rate, high surface to volume ratio, and the improved signal-to-noise ratio in electroanalytical measurements [74]. For example, copper nanoclusters prepared via a simple one-step electrodeposition process on platinum electrode were used to determine nitrates [107]. Also, cetyltrimethylammonium bromide-(CTAB-) capped copper nanoparticles (CTAB-Cups) have

been used as a colorimetric probe for the detection of dithiocarbamate pesticides [108]. Another study reports colorimetric copper-based sensors for the detection of mercury(II) ions [109].

4.2. Metal Oxide Nanostructures in Sensors. Semiconductor metal oxide-based nanostructured materials have been expansively used as sensors in numerous applications since they can enhance the sensor's performance due to their small crystallite size [110]. Semiconducting metal oxide- (SMOX-) based sensors are small, robust, inexpensive, and sensitive and easy to produce, making them highly attractive for handheld portable medical diagnostic detectors [110, 111]. They have been used to produce highly sensitive gas sensors mainly because of their good chemical reliability, real-time monitoring, and easy fabrication [112]. For example, a 3D nanoheterojunction layout of nickel oxide-zinc oxide (NiO-Zn) p-n semiconductors with a grain size of ≈ 20 nm nanometers and a porosity of $\approx 98\%$ for the rapid room temperature chemical sensing of volatile organic compounds has been reported by Chen and coworkers [113]. In their work, they observed the sensor response was increased by more than four times, while the limit of detection was improved by decorating the ZnO nanoparticle networks with NiO. Under solar light irradiation, the optimal NiO-ZnO nanoheterojunction networks demonstrated a strong and selective room temperature response to two important volatile organic compounds utilized for breath analysis. Likewise, ZnO/graphene oxide (GO) nanosheets, synthesized using the wet-chemical method with an additional calcining treatment, for the tremendous sensing of acetone as a target gas have been reported [114]. The excellent sensing performance was ascribed to the synergistic effects between ZnO nanosheets and GO, which included a unique 2D structure, large specific surface area, suitable particle size, and abundant in-plane mesopores [114]. A ZnO/ In_2O_3 heterostructure-based sensor for ethanol gas at 240°C has been reported [115]. The sensor was found to exhibit a response as high as 170 toward 50 ppm of ethanol, which is about 3.3 times higher than that of pure In_2O_3 -based sensor as well as excellent selectivity, good long-term stability, and moderate response and recovery speed (35/46 s) toward ethanol [115].

Tungsten trioxide (WO_3), the second most commonly used semiconducting metal oxide in gas sensors, has been reported to show high sensor responses to several biomarkers found in breath, e.g., acetone, ammonia, carbon monoxide, hydrogen sulfide, toluene, and nitric oxide since the modern material science allows WO_3 samples to be tailored to address certain sensing needs [111]. For example, Pt-functionalized WO_3 hemitubes and graphene-functionalized WO_3 hemitubes for the detection of acetone (CH_3COCH_3) and hydrogen sulfide (H_2S) which are biomarkers for the diagnosis of diabetes and halitosis have been reported [116, 117]. Both studies reported remarkable selectivity, enhanced sensitivity, and low detection limits offering a potential platform for application in diabetes and halitosis diagnosis. These superior sensing properties were ascribed to the electronic sensitization of graphene and platinum-based materials by modulating space-charged layers at the interfaces between

n-type WO_3 hemitubes and p-type graphene-based materials, as identified by Kelvin Probe Force Microscopy (KPFM). The rapid response and superior sensitivity of the proposed sensing materials was found to follow cyclic thermal aging which demonstrated a good potential for real-time exhaled breath diagnosis of diseases [116, 117].

Graphene-functionalized tin oxide (SnO_2) nanofibers (NF)/nanosheets (NS) have also been reported in the detection of acetone and hydrogen sulfide levels in exhaled human breath as biomarkers for diabetes and halitosis [118] as well as for the detection of formaldehyde (HCHO) [119, 120]. The sensors exhibited high sensitivity and low detection limits which was ascribed to the high specific area, suitable electron transfer channels, and the synergistic effect of the SnO_2 NF/NSs and the graphene oxide network [118–120]. Another study reports a 3D hierarchical $\text{In}_2\text{O}_3@\text{SnO}_2$ core-shell nanofiber ($\text{In}_2\text{O}_3@\text{SnO}_2$) designed using vertically aligned SnO_2 nanosheets uniformly grown on the outside surface of In_2O_3 nanofibers and tested for the sensing performance of formaldehyde (HCHO) [121]. The sensing performance of the $\text{In}_2\text{O}_3@\text{SnO}_2$ nanocomposite was found to possess the highest response value, fast response/recovery speed, best selectivity, and lowest HCHO detection limit which were attributed to the synergistic effect of large specific surface areas of SnO_2 nanosheet arrays, abundant adsorbed oxygen species on the surface, unique electron transformation between core-shell heterogeneous materials, and long electronic transmission channel of SnO_2 transition layer [121].

Another study reports chromium (III) oxide nanoparticles coated with tin oxide nanofibers (Cr_2O_3 NPs. coated SnO_2 NFs.) synthesized using a sol-gel process and an electrospinning method and characterized by X-ray diffraction (XRD), scanning electron microscope (SEM), X-ray energy dispersive spectroscopy (EDS), and X-ray photoelectron spectroscopy (XPS) [112]. The Cr_2O_3 NPs. coated SnO_2 NFs were found to exhibit low optimal operating temperature, high sensing response, excellent response-recovery time, and long-term stability to C_2H_2 [112].

All the examples described above clearly show that incorporating nanostructured materials into the sensors led to improved performances in terms of increased sensitivity, selectivity, stability, and detection limits.

4.3. Carbon Nanotubes in Sensors. Carbon nanotubes (CNTs) are theoretically cylindrical fabricated rolled up graphene sheets which can be classified single walled carbon nanotubes (SWCNTs) or multiwalled carbon nanotubes (MWCNTs) [122, 123]. The SWCNTs normally consist of a single graphite sheet flawlessly wrapped into a cylindrical tube, while multiwalled carbon nanotube (MWCNTs) comprise an array of such nanotubes [124]. Although CNTs are made of carbon with similar dimension aspect ratio, they can be either metallic or semiconducting depending on the rolling up of the graphene layers [123]. They normally have a high aspect ratio which makes them suitable for functionalization through chemical or physical methods [123]. They can be produced via the chemical vapor deposition method which has the advantage to be scalable, to allow large-area deposition, and to provide CNTs that are already attached onto a substrate

and hence easy to be collected [125]. They are said to have amazing electrical, mechanical, and thermal properties as well as partial antibacterial activity due to their high aspect ratio and high surface area [126]. The high sensitivity of the electronic properties of nanotubes to molecules adsorbed on their surface and the unparalleled unit surface providing for this high sensitivity make CNT a promising starting material for the development of super miniaturized chemical and biological sensors [127, 128]. The operation of the CNT-based sensors is established on the changes in the V-I curve of the nanotube as a result of adsorption of specific molecules on their surface [127] which is one of their most promising applications in electronics. The sensors should have a high sensitivity as well as fast response and recovery [127]. Carbon nanotubes have been used in gas sensors, biosensors, photo-sensors, and pressure sensors among others. In this section, we will provide a review of the current advances of carbon nanotubes in sensor application.

4.3.1. Carbon Nanotubes in Gas Sensors. Gas sensors are chemical sensors, which have found widespread applications in industry, environmental monitoring, space exploration, biomedicine, and pharmaceuticals [129]. Highly sensitive and selective gas sensors are required to detect leakage of explosive gases such as hydrogen and also for real-time detections of lethal or pathogenic gases in industries [129]. Due to the increasing global warming, there is also a strong demand of sensitive and selective gas sensors which can monitor and control our ambient environment [129]. The most common gas sensing principle is said to be the adsorption and desorption of gas molecules on the sensing materials, and therefore, increasing the contact interfaces between analyte and the sensing material can significantly enhance the sensitivity of gas sensors [129]. The CNTs are known to possess a huge specific surface and a robust van der Waals binding energy, which can provide well-defined adsorption sites for gas molecules which enable the application of CNTs to be an adsorbent to remove some undesirable gases and a sensor to react with target gases reflected by self-changes of physiochemical properties [129, 130] as illustrated in Figure 9. Carbon nanotube-based gas sensors have been widely considered due to their prominent properties such as faster response, enhanced sensitivity, and lower operating temperature [131, 132].

The adsorption ability of the CNTs has been found to change through doping metal or nonmetals on the sidewalls [130]. When the dopant atom(s) are coupled with the carbon can cage, they constitute a mutual area which exerts a great influence on the adsorption behaviors of the as-produced CNTs for gas [130]. Sensing of gas molecules using the adsorption properties of CNTs doped with different metals such as Pt [134], Au [135], Pd [136], Ni [137], Al [138], and nonmetals such as B and N [139] has been reported. In a study reported by Zhang et al. [140] where they studied the gas-sensitive response of Pd-SWCNT sensors to five different kinds of SF_6 decomposition gases (SO_2F_2 , SOF_2 , SO_2 , H_2S , and CF_4), they found that the conductivity of the nanotube increases once exposed to adsorbed gases with SO_2 having the highest conductivity while CF_4 decreased

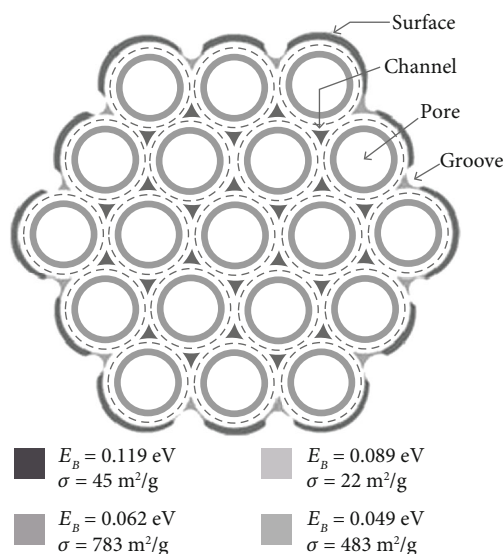


FIGURE 9: Schematic structure of a SWCNT bundle showing the available sites for gas adsorption. Dashed line indicates the nuclear skeleton of the nanotubes. Adapted from [129], an open access article. Binding energies E_B and specific surface area contributions (σ) for H_2 adsorption on these sites are as indicated in [133].

[140]. An Au-CNT-based sensor has also been shown to selectively detect H_2S and SO_2 as reported by Zhang et al. [141]. In their study, they found that Au-SWCNTs had better sensitivity than non-doped SWCNT in response to H_2S and SO_2 . They also found that the Au-SWCNT possessed a rewarding response to the two analytes where an increase in conductivity was realized in response to SO_2 since there was a plentiful electron transfer to SO_2 from the Au-SWCNTs as opposed to a decline in tube conductivity for the case of H_2S where there was an electron shift from the H_2S to the SWCNTs. These results indicated that, based on the change of the nanotube conductivity, the Au-SWCNT-based sensors can selectively SO_2 and H_2S gases.

Likewise, NiCl_2 -doped MWCNT sensors prepared by ultrasonic $\text{NiCl}_2 \cdot 6\text{H}_2\text{O}$ crystal suspension liquid of carbon nanotubes when tested for the gas response of SF_6 decomposition products have been reported [142], and the sensor was found to have a high sensitivity and fast response to SO_2F_2 and SOF_2 , compared to SO_2 . Their results also indicated that MWCNTs modified by functional groups are sensitive to H_2S , and MWCNTs modified by metal have a strong response to SO_2F_2 confirming that the selectivity of CNT-based materials in detecting such gases can be achieved [142]. Other than doping the CNTs using metals, studies have also shown that modified CNTs using the hydroxyl and carboxyl functional groups have the potential to detect H_2S as well as SO_2 [143, 144].

Nitrogen dioxide (NO_2), a highly reactive gas and used mostly as a catalyst in oxidative reactions, for manufacturing explosives, as a polymerization inhibitor, and as rocket fuel, has been detected using SWCNTs and MWCNTs. SWCNTs functionalized with poly(m-aminobenzene sulfonic acid) have been reported to detect NO_2 and ammonia NH_3 gases at low concentrations with the lowest detected concentration

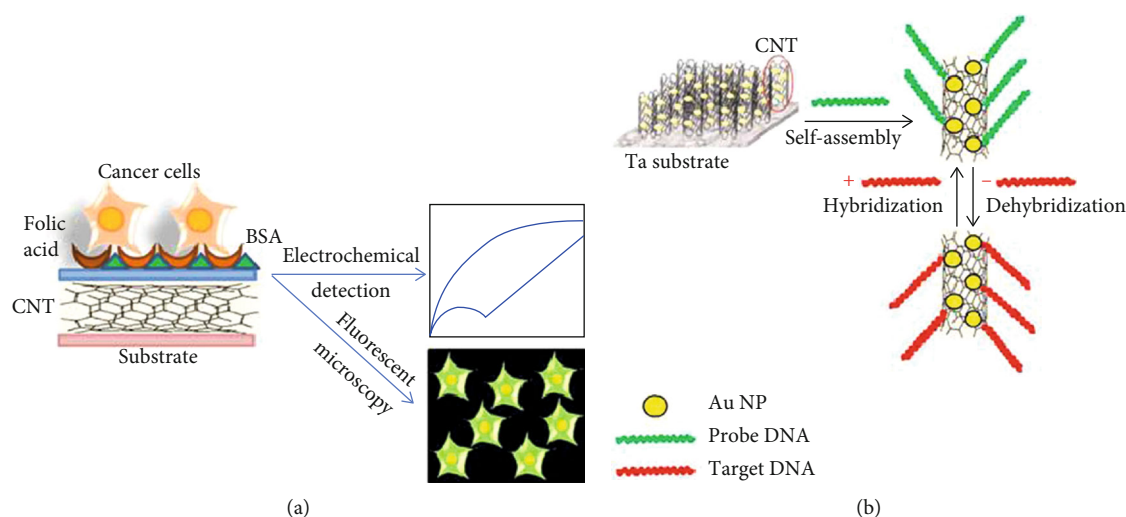


FIGURE 10: (a) Schematic illustration of carbon nanotubes immobilized on a sensor surface for an enhanced electrochemical detection of cancer cells. (b) Schematic representation of gold nanoparticles/aligned CNTs immobilized for an electrochemical DNA biosensor for cancer detection. Adapted from [163], an open access article.

for NO_2 being 20 ppb [145]. This was attributed to the functionalization of SWCNTs which was found to improve the processing capability and sensitivity of the sensors. Multi-walled carbon nanotubes (MWCNTs) have also been used to develop NO_2 gas sensors which are capable of measuring low concentration going down to 0.1 ppm [146]. Another work has reported the detection of NO_2 using a combination of SWCNTs and MWCNTs on porous silicon wafers which was done at different temperatures [147]. Their results indicated that the equal sensitivity for the two types of CNTs was achieved with higher temperatures for the SWCNTs as compared to the MWCNTs. A nanocomposite with MWCNTs using poly(thiophene-3-[2-(2-methoxyethoxy)ethoxy]-2,5-diyl) (PThME) and 3-thiopheneacetate additive has also been reported to detect NO_2 [148]. The detection range for NO and NO_2 from this study was found to be between 2 and 5 ppm while sensitivity in the response of these nanocomposite-based devices increased with the increase in temperature ranging between 25°C and 100°C [148].

Other gases which have been detected using carbon nanotubes include ammonia NH_3 [149–152] gas, carbon monoxide (CO) gas [153–157], and chlorine gas [158–160] among others.

4.3.2. Carbon Nanotubes in Biosensors. A biosensor can be defined as a device that uses biochemical reactions to detect an analyte and a physiochemical component to produce a measurable signal [161]. It is normally composed of three components, the biological element or biomolecules, transducers, and detector as illustrated in Figure 10. The biological element is responsible for detecting the analyte and generating a response signal which is then transformed into a detectable response while the detector amplifies the processes and the signals before displaying it using a display system [162]. The biological elements are normally immobilized on the sensor surface, and their interaction with the analyte of interest generates a response signal which can be either an electrochemical signal, optical signal, or colorimetric signal.

The sensitivity and selectivity of the biosensors depend on the immobilization of the biological elements. Due to their unique properties described earlier, carbon nanotubes (CNTs) can serve as platforms for immobilization of biomolecules at their surface, combining their exceptional physical, chemical, electrical, and optical characteristics which make them one of the best suited materials for the transduction of signals associated with the recognition of analytes, metabolites, or disease biomarkers [123, 163, 164] as illustrated in Figure 9 [163]. For example, CNTs have been used to develop electrochemical biosensors whose principle of action is based on oxidation and reduction reactions between the biomolecules and the analytes. Carbon nanotubes modified by redox polymers serving as a catalyst for the interaction of the biomolecules and the analyte have been reported [165]. The combination of CNTs with the polymers has been found to improve the electrical conductivity and mechanical strength of the hybrid material and hence the sensitivity of the biosensor [165]. Such combinations have been reported in biosensors for the detection of glucose, uric acid, hydrogen peroxide, ascorbic acid, dopamine, folic acid, cancer cells, and deoxyribonucleic acid (DNA) [163, 166–171].

Optical carbon nanotube-based biosensors have also been reported on the detection of cancer cells through changes in the emission of light (ultraviolet, visible, or infrared) [172, 173]. In all the applications described above, the CNTs have been used to improve the immobilization of the biological elements which in turn led to an enhanced sensitivity, selectivity, and response time of the target analytes.

4.3.3. Carbon Nanotubes in Photo Sensors. A photo sensor can be defined as an electronic component that can detect the presence of visible light, infrared transmission, and/or ultraviolet (UV) energy [174]. They consist of semiconductors with photoconductivity in which electrical conductance can vary depending on the intensity of the radiation striking the material. They can be used for integrating natural and electrical lighting [175]. Due to their optical properties,

TABLE 1: Sensors based on polymer nanocomposites.

Polymer nanocomposite (sensory material)	Analyte	Detection limit	Reference
Zinc oxide nanoparticles intercalated into polypyrrole (ZnO-PPy)	Xanthine	0.8 μM	[196]
Polypyrrole nanosheets decorated with platinum nanoparticles (PPy-Pt)	Hydrogen peroxide	0.6 μM	[197]
NiCo ₂ O ₄ -polyaniline (NiCo ₂ O ₄ -PANI)	Glucose	0.3833 μM	[198]
Graphene polyaniline nanocomposite- (GR-PANI-) modified glassy carbon electrode (GCE) (GR-PANI-GCE)	4-Aminophenol	$6.5 \times 10^{-8} \text{ M}$	[199]
Graphene-polyaniline-horseradish peroxidase (Grp-PANI-HRP)	Malaria drug Artesunate	0.012 ng mL ⁻¹	[200]
Polyaniline and zirconia nanocomposite film (PANI-ZrO ₂)	Esomeprazole	97.21 ng mL ⁻¹	[201]
Gold-polyaniline-graphene nanocomposites (Au-Grp-PANI)	Nitrite	0.01 $\mu\text{mol L}^{-1}$	[202]
Polypyrrole/graphene nanocomposite (PPy-Grp-GCE)	Adenine, guanine	0.02 μM and 0.01 μM	[203]
Polypyrrole/graphene oxide nanosheets (PPy-GrpO)	Dopamine	73.3 nM	[204]
Praphene-poly(3,4-ethylenedioxythiophene) (graphene-PEDOT) nanocomposite film with ascorbate oxidase (AO) entrapped (Grp-PEDOT-AO)	Ascorbic acid	2.0 μM	[205]
Graphene-polyaniline-Bi ₂ O ₃ (Grp-PANI-Bi ₂ O ₃) composite	Anti-inflammatory drug Etodolac	10.03 ng mL ⁻¹	[206]
Copper phosphate nanospheres, polymerized dopamine hydrochloride (Cu ₃ (PO ₄) ₂ /PDA/Ab2 GCE)	C-reactive protein	0.13 pg mL ⁻¹	[207]

CNTs have been used in photo sensors since when a high energy photon hits a semiconducting CNT, it generates an electron/hole pair within the nanostructure. A built-in potential then separates the two charge carriers enabling a photocurrent to be measured which is the concept behind CNT-based photo sensors [123].

A flexible CNTs photo sensor array for light detection has been reported [176]. In this study, the CNTs for light detection were embedded into a flexible parylene-C film and the photo sensor array fabricated using micromachining processes. Their results indicated an output photocurrent which varied linearly with the input light intensity [176]. A fabricated visible photo sensor based on the on double-walled carbon nanotube (DWCNT) film/Cu₂O nanoparticle (NP) film/TiO₂ nanotube array (TNA) heterojunctions has been reported [177]. Their results indicated an enhanced optoelectronic performance when compared to that of the heterojunctions without Cu₂O nanoparticles. Carbon nanotubes can also be used to improve the selectivity of photo sensors. For example, perovskite/carbon nanotube hybrids were used to develop a photo sensor which could distinguish between ultraviolet, visible, and infrared spectrum [178]. In this study, the authors used organo-lead halide perovskites (CH₃NH₃PbX₃) which possess remarkable optoelectronic properties and tunable optical band gaps by changing the halogens and when integrated with SWCNTs can further improve their photoresponsivity [178]. The CH₃NH₃PbCl₃-based photo sensor showed a responsivity up to 10⁵ A W⁻¹ to ultraviolet and no obvious response to visible light, which is superior to that of most ultraviolet sensors [178] while the CH₃NH₃PbBr₃-based photo sensor was found to exhibit a high responsivity to visible light [178], and therefore, by changing the halogen, the photo sensor is able to distinguish between the different electromagnetic radiations.

4.3.4. Carbon Nanotubes in Pressure Sensors. A pressure sensor is a device that can sense pressure and convert it into an

electric signal where the amount depends upon the pressure applied [179]. Freestanding films containing vertically aligned CNTs are said to exhibit supercompressible foam-like behavior [180], whereas ultralong CNT blocks can act as pressure or strain sensors, exhibiting reversible electrical conductivities and a compressive strain response [181] and therefore can be used in pressure sensors. For example, a pressure sensor based on the arrangement of vertically aligned carbon nanotubes (VACNTs) which was supported by a polydimethylsiloxane (PDMS) matrix has been reported [182]. In this study, the VACNTs embedded in the PDMS matrix were structurally flexible and were able to provide a repeated sensing operation due to the high elasticities of both the polymer and the carbon nanotubes (CNTs) [182]. To accomplish flexible functional electronics, the VACNT-based pressure sensor was incorporated into a field-effect transistor, fabricated using sprayed semiconducting carbon nanotubes on plastic substrate [182]. In another study, functionalized carbon nanotubes on nonconductive fibers coated by electrophoretic deposition (EPD) onto a backing electrode followed by film formation onto the fibers creating a conductive network have been used to develop a pressure sensor [183]. The pressure sensor displayed a large in-plane change in electrical conductivity with applied out-of-plane pressure [183] indicating resilience of the nanocomposite interphase which enabled sensing of high pressures without permanent changes to the sensor response as well as showing high repeatability [183].

4.4. Polymer Nanocomposites in Sensors. Polymer nanocomposites comprise a class of materials formed by at least finely dispersed phase with nanomaterials such as nanoparticles, nanotubes, or nanosheets [184–186]. They are superior type of tools in which the nanomaterials are spread in a polymer matrix resulting in innovative materials with unique physical and chemical properties [184, 185, 187–193]. The polymer

matrix can be made from a variety of polymers such as polyamides, polyethersulfone, polyurethanes, polyamic acid, poly(vinylidene fluoride) (PVDF), poly(vinyl alcohol) (PVA), polyacrylonitrile, or polytetrafluoroethylene (PTFE) among others [184, 194]. Polymer nanocomposites (PNCs) have electrochemical properties and can be used as transducers in the development of electrochemical sensors and biosensors since they have high electrical conductivity rate, large surface area and fast electron rate leading to high sensitivity, and selectivity and low detection limits of the sensors [195]. In addition, the interactive fillers in the PNCs facilitate ion diffusion that impacts the sensing applications through intercalation into the PNC matrices leading to better stability of active electron transfer sites and detection limits [195]. These active fillers help in reducing the layer thickness in PNC leading to ultrathin electrochemical detector technology [195]. Based on these properties of PNC, they have been used in the development of sensors for various analytes some of which are summarized in Table 1.

5. Conclusions and Future Perspectives

In this review article, we have discussed fabrication techniques of different nanostructures as well as their applications of in the field of sensors. Owing to their superior physicochemical and plasmonic properties of nanostructured materials, they have generated a great deal of interest in many sensing applications. Though the potential uses of these nanostructures in sensors applications are numerous, there are a few limitations which might hinder these applications. For example, gas sensors based on carbon nanotubes have been found to lack selectivity [123]. This lack of selectivity is a major roadblock which can hamper further usage of these CNT-based devices; though this can be mitigated by coupling of the CNTs with other materials, more work needs to be done to improve their selectivity. There are also technical difficulties of nanostructure fabrication as well as serious concerns about nanostructure toxicity which might vary depending on the physical characteristics of each new particle type. Further research is therefore required to evaluate and solve these issues. The sustainability of the nanostructured materials which is very important has not been fully investigated, and therefore, it would be important to look into their sustainability in sensor applications. If the issues can be overcome, the high sensitivity, specificity, reduced cost, portability, and reusability of nanostructures which has been described in this review will make nanostructured materials an appealing alternative to current sensors. This is however achievable since there has been a continued progress in the field of nanotechnology with increasing research in the nanoscale which can lead to enhanced performance of the existing sensors as well as the development of newer sensors based on novel mechanisms.

Data Availability

The data used to support the findings are cited within the article as figures.

Conflicts of Interest

The author declares that there are no conflicts of interest regarding the publication of this review.

Acknowledgments

The author would like to thank the School of Pharmacy and Health Sciences, United States International University-Africa, for providing a conducive environment and facilities from which this work was written.

References

- [1] X. Cheng, *10 - Nanostructures: fabrication and applications, in Nanolithography*, M. Feldman, Ed., Woodhead Publishing, 2014.
- [2] W. G. Kreyling, M. Semmler-Behnke, and Q. Chaudhry, "A complementary definition of nanomaterial," *Nano Today*, vol. 5, no. 3, pp. 165–168, 2010.
- [3] M. M. Bellah, S. M. Christensen, and S. M. Iqbal, "Nanostructures for medical diagnostics," *Journal of Nanomaterials*, vol. 2012, Article ID 486301, 21 pages, 2012.
- [4] M. Nasrollahzadeh, Z. Issaabadi, M. Sajjadi, S. M. Sajadi, and M. Atarod, "Types of Nanostructures," in *Interface Science and Technology*, pp. 29–80, Elsevier, 2019.
- [5] N. Nasiri and C. Clarke, "Nanostructured gas sensors for medical and health applications: low to high dimensional materials," *Biosensors*, vol. 9, no. 1, p. 43, 2019.
- [6] X. Huang, I. H. el-Sayed, W. Qian, and M. A. el-Sayed, "Cancer cell imaging and photothermal therapy in the near-infrared region by using gold nanorods," *Journal of the American Chemical Society*, vol. 128, no. 6, pp. 2115–2120, 2006.
- [7] P. K. Jain and M. A. El-Sayed, "Universal scaling of plasmon coupling in metal nanostructures: extension from particle pairs to nanoshells," *Nano Letters*, vol. 7, no. 9, pp. 2854–2858, 2007.
- [8] P. K. Jain, X. Huang, I. H. el-Sayed, and M. A. el-Sayed, "Noble metals on the nanoscale: optical and photothermal properties and some applications in imaging, sensing, biology, and medicine," *Accounts of Chemical Research*, vol. 41, no. 12, pp. 1578–1586, 2008.
- [9] P. Logeswari, S. Silambarasan, and J. Abraham, "Ecofriendly synthesis of silver nanoparticles from commercially available plant powders and their antibacterial properties," *Scientia Iranica*, vol. 20, no. 3, pp. 1049–1054, 2013.
- [10] V. V. Makarov, A. J. Love, O. V. Sinitsyna et al., "'Green' nanotechnologies: synthesis of metal nanoparticles using plants," *Acta Naturae*, vol. 6, no. 1, pp. 35–44, 2014.
- [11] A. Verma and M. S. Mehata, "Controllable synthesis of silver nanoparticles using Neem leaves and their antimicrobial activity," *Journal of Radiation Research and Applied Sciences*, vol. 9, no. 1, pp. 109–115, 2019.
- [12] N. Noah, *Green synthesis: characterization and applications of silver and gold nanoparticles, in Green Synthesis, Characterization and Applications of Nanoparticles*, S. Holt, Ed., Elsevier Publishers, 2018.
- [13] M. Muhammed, "Engineering of nanostructured materials," in *In Nanostructures: Synthesis, Functional Properties and Applications. NATO Science Series (Series II: Mathematics*,

- Physics and Chemistry*), Springer Netherlands, Dordrecht, 2003.
- [14] H.-D. Yu, M. D. Regulacio, E. Ye, and M. Y. Han, "Chemical routes to top-down nanofabrication," *Chemical Society Reviews*, vol. 42, no. 14, pp. 6006–6018, 2013.
 - [15] E. Stern, J. F. Klemic, D. A. Routenberg et al., "Label-free immunodetection with CMOS-compatible semiconducting nanowires," *Nature*, vol. 445, no. 7127, pp. 519–522, 2007.
 - [16] B. M. Venkatesan and R. Bashir, "Nanopore sensors for nucleic acid analysis," *Nature Nanotechnology*, vol. 6, no. 10, pp. 615–624, 2011.
 - [17] A. Biswas, I. S. Bayer, A. S. Biris, T. Wang, E. Dervishi, and F. Faupel, "Advances in top-down and bottom-up surface nanofabrication: Techniques, applications & future prospects," *Advances in Colloid and Interface Science*, vol. 170, no. 1-2, pp. 2–27, 2012.
 - [18] J. E. E. Baglin, "Ion beam nanoscale fabrication and lithography—a review," *Applied Surface Science*, vol. 258, no. 9, pp. 4103–4111, 2012.
 - [19] S. Kawata, H. B. Sun, T. Tanaka, and K. Takada, "Finer features for functional microdevices," *Nature*, vol. 412, no. 6848, pp. 697–698, 2001.
 - [20] Y. Qiao, D. Wang, and J. M. Buriak, "Block copolymer templated etching on silicon," *Nano Letters*, vol. 7, no. 2, pp. 464–469, 2007.
 - [21] B. Fabre, L. Henrous, S. Ababou-Girard, and C. Meriadec, "Electroless patterned assembly of metal nanoparticles on hydrogen-terminated silicon surfaces for applications in photoelectrocatalysis," *ACS Applied Materials & Interfaces*, vol. 5, no. 2, pp. 338–343, 2012.
 - [22] H. Yu, D. Wang, and M.-Y. Han, "Top-down solid-phase fabrication of nanoporous cadmium oxide architectures," *Journal of the American Chemical Society*, vol. 129, no. 8, pp. 2333–2337, 2007.
 - [23] T. Prasad Yadav, R. Manohar Yadav, and D. Pratap Singh, "Mechanical milling: a top down approach for the synthesis of nanomaterials and nanocomposites," *Nanoscience and Nanotechnology*, vol. 2, no. 3, pp. 22–48, 2012.
 - [24] S. Bashir and J. Liu, "Chapter 2 - Overviews of synthesis of nanomaterials," in *Advanced Nanomaterials and their Applications in Renewable Energy*, J. L. Liu and S. Bashir, Eds., pp. 51–115, Elsevier, Amsterdam, 2015.
 - [25] E. Valentin, S. Auvray, A. Filoramo et al., "Self-assembly fabrication of high performance carbon nanotubes based FETs," *MRS Proceedings*, vol. 772, 2003.
 - [26] S. Rauf, A. Glidle, and J. M. Cooper, "Production of quantum dot barcodes using biological self-assembly," *Advanced Materials*, vol. 21, no. 40, pp. 4020–4024, 2009.
 - [27] J.-O. Carlsson and P. M. Martin, "Chapter 7 - Chemical vapor deposition," in *Handbook of Deposition Technologies for Films and Coatings (Third Edition)*, P. M. Martin, Ed., pp. 314–363, William Andrew Publishing, Boston, 2010.
 - [28] Y. B. Pottathara, Y. Grohens, V. Kokol, N. Kalarikkal, and S. Thomas, "Chapter 1 - Synthesis and Processing of Emerging Two-Dimensional Nanomaterials," in *Nanomaterials Synthesis*, pp. 1–25, Elsevier, 2019.
 - [29] Y. Li, J. D. Cain, E. D. Hanson et al., "Au@MoS₂core-shell heterostructures with strong light-matter interactions," *Nano Letters*, vol. 16, no. 12, pp. 7696–7702, 2016.
 - [30] R. Binions and I. P. Parkin, "Novel Chemical Vapour Deposition Routes to Nanocomposite Thin Films," in *Advances in Nanocomposites - Synthesis, Characterization and Industrial Applications*, United Kingdom, 2011.
 - [31] F. Ogawa, C. Masuda, and H. Fujii, "In situ chemical vapor deposition of metals on vapor-grown carbon fibers and fabrication of aluminum-matrix composites reinforced by coated fibers," *Journal of Materials Science*, vol. 53, no. 7, pp. 5036–5050, 2018.
 - [32] J. Zhang and T. Goto, "Fabrication of Al₂O₃-Cu Nanocomposites Using Rotary Chemical Vapor Deposition and Spark Plasma Sintering," *Journal of Nanomaterials*, vol. 2015, Article ID 790361, 7 pages, 2015.
 - [33] P. R. Somani, S. P. Somani, and M. Umeno, "Planer nanographenes from camphor by CVD," *Chemical Physics Letters*, vol. 430, no. 1-3, pp. 56–59, 2006.
 - [34] Y. Shi, C. Hamsen, X. Jia et al., "Synthesis of few-layer hexagonal boron nitride thin film by chemical vapor deposition," *Nano Letters*, vol. 10, no. 10, pp. 4134–4139, 2010.
 - [35] Y. Gogotsi, "Transition metal carbides go 2D," *Nature Materials*, vol. 14, no. 11, pp. 1079–1080, 2015.
 - [36] G. Tai, T. Hu, Y. Zhou et al., "Synthesis of atomically thin boron films on copper foils," *Angewandte Chemie*, vol. 54, no. 51, pp. 15473–15477, 2015.
 - [37] R. Asmatulu, "Nanocoatings for corrosion protection of aerospace alloys," in *Corrosion Protection and Control Using Nanomaterials*, V. S. Saji and R. Cook, Eds., pp. 357–374, Woodhead Publishing, 2012.
 - [38] M. Oliveira and A. Machado, *Preparation of polymer-based nanocomposites by different routes, a book chapter in Nanocomposites: Synthesis, Characterization and Applications Book*, X. Wang, Ed., NOVA Publishers, 2013.
 - [39] Y. Lu, W. Dong, J. Ding, W. Wang, and A. Wang, "Hydroxyapatite nanomaterials: synthesis, properties, and functional applications," in *Nanomaterials from Clay Minerals*, A. Wang and W. Wang, Eds., pp. 485–536, Elsevier, 2019.
 - [40] S. K. Padmanabhan, A. Balakrishnan, M. C. Chu, Y. J. Lee, T. N. Kim, and S. J. Cho, "Sol-gel synthesis and characterization of hydroxyapatite nanorods," *Particuology*, vol. 7, no. 6, pp. 466–470, 2009.
 - [41] C. Daraio and S. Jin, "Synthesis and patterning methods for nanostructures useful for biological applications," in *Nanotechnology for Biology and Medicine: At the Building Block Level*, G. A. Silva and V. Parpura, Eds., pp. 27–44, Springer New York, New York, NY, 2012.
 - [42] V. de Oliveira Sousa Neto, T. M. Freire, G. D. Saraiva et al., "Chapter 5 - Water Treatment Devices Based on Zero-Valent Metal and Metal Oxide Nanomaterials," in *Nanomaterials Applications for Environmental Matrices*, pp. 187–225, Elsevier, 2019.
 - [43] S. Prasad, V. Kumar, S. Kirubanandam, and A. Barhoum, "Chapter 11 - Engineered nanomaterials: nanofabrication and surface functionalization," in *Emerging Applications of Nanoparticles and Architecture Nanostructures*, A. Barhoum and A. S. H. Makhoulouf, Eds., pp. 305–340, Elsevier, 2018.
 - [44] E. Moncada, R. Quijada, and J. Retuert, "Nanoparticles prepared by the sol-gel method and their use in the formation of nanocomposites with polypropylene," *Nanotechnology*, vol. 18, no. 33, p. 335606, 2007.
 - [45] S. Wang and L. Gao, "Chapter 7 - Laser-driven nanomaterials and laser-enabled nanofabrication for industrial applications," in *Industrial Applications of Nanomaterials*, S. Thomas, Y. Grohens, and Y. B. Pottathara, Eds., pp. 181–203, Elsevier, 2019.

- [46] D. Sumanth Kumar, B. J. Kumar, and H. M. Mahesh, "Chapter 3 - Quantum nanostructures (QDs): an overview," in *Synthesis of Inorganic Nanomaterials*, S. M. Bhagyaraj, Ed., pp. 59–88, Woodhead Publishing, 2018.
- [47] A. Rus, V.-D. Leordean, and P. Berce, "Silver nanoparticles (AgNP) impregnated filters in drinking water disinfection," *MATEC Web of Conferences*, vol. 137, article 07007, 2017.
- [48] W. B. Ayinde, W. M. Gitari, M. Munkombwe, A. Samie, and J. A. Smith, "Green synthesis of AgMgOnHaP nanoparticles supported on chitosan matrix: defluoridation and antibacterial effects in groundwater," *Journal of Environmental Chemical Engineering*, vol. 8, no. 5, article 104026, 2020.
- [49] N. Krithiga, A. Rajalakshmi, and A. Jayachitra, "Green synthesis of silver nanoparticles using leaf extracts of *Clitoria ternatea* and *Solanum nigrum* and study of its antibacterial effect against common nosocomial pathogens," *Journal of Nanoscience*, vol. 2015, Article ID 928204, 8 pages, 2015.
- [50] H. Alizadeh, M. Salouti, and R. Shapouri, "Bactericidal effect of silver nanoparticles on intramacrophage *Brucella abortus* 544," *Jundishapur J Microbiol*, vol. 7, no. 3, article e9039, 2014.
- [51] N. Durán, M. Durán, M. B. de Jesus, A. B. Seabra, W. J. Fávaro, and G. Nakazato, "Silver nanoparticles: a new view on mechanistic aspects on antimicrobial activity," *Nanomedicine: Nanotechnology, Biology and Medicine*, vol. 12, no. 3, pp. 789–799, 2016.
- [52] S. Mohanty, S. Mishra, P. Jena, B. Jacob, B. Sarkar, and A. Sonawane, "An investigation on the antibacterial, cytotoxic, and antibiofilm efficacy of starch-stabilized silver nanoparticles," *Nanomedicine: Nanotechnology, Biology and Medicine*, vol. 8, no. 6, pp. 916–924, 2012.
- [53] Y. Matsumura, K. Yoshikata, S. I. Kunisaki, and T. Tsuchido, "Mode of bactericidal action of silver zeolite and its comparison with that of silver nitrate," *Applied and Environmental Microbiology*, vol. 69, no. 7, pp. 4278–4281, 2003.
- [54] G. Nangmenyi, Z. Yue, S. Mehrabi, E. Mintz, and J. Economy, "Synthesis and characterization of silver-nanoparticle-impregnated fiberglass and utility in water disinfection," *Nanotechnology*, vol. 20, no. 49, article 495705, 2009.
- [55] A. H. M. El-Aassar, M. M. Said, A. M. Abdel-Gawad, and H. A. Shawky, "Using silver nanoparticles coated on activated carbon granules in columns for microbiological pollutants water disinfection in Abu Rawash area, Great Cairo, Egypt," *Australian Journal of Basic and Applied Sciences*, vol. 7, no. 1, pp. 422–432, 2013.
- [56] T. A. Dankovich and D. G. Gray, "Bactericidal paper impregnated with silver nanoparticles for point-of-use water treatment," *Environmental Science & Technology*, vol. 45, no. 5, pp. 1992–1998, 2011.
- [57] S. M. Praveena, L. S. Han, L. T. L. Than, and A. Z. Aris, "Preparation and characterisation of silver nanoparticle coated on cellulose paper: evaluation of their potential as antibacterial water filter," *Journal of Experimental Nanoscience*, vol. 11, no. 17, pp. 1307–1319, 2016.
- [58] E. N. Kallman, V. A. Oyanedel-Craver, and J. A. Smith, "Ceramic filters impregnated with silver nanoparticles for point-of-use water treatment in rural Guatemala," *Journal of Environmental Engineering*, vol. 137, no. 6, pp. 407–415, 2011.
- [59] P. Jain and T. Pradeep, "Potential of silver nanoparticle-coated polyurethane foam as an antibacterial water filter," *Biotechnology and Bioengineering*, vol. 90, no. 1, pp. 59–63, 2005.
- [60] L. A. D. Koslowski, A. L. Nogueira, S. Licodiedoff, A. T. Comper, and M. V. Folgueras, "Silver nanoparticles impregnated with polyamide-66 to disinfect drinking water," *Ambiente e Agua - An Interdisciplinary Journal of Applied Science*, vol. 13, no. 6, 2018.
- [61] N. T.-P. Nguyen, L. V. H. Nguyen, N. T. Thanh et al., "Stabilization of silver nanoparticles in chitosan and gelatin hydrogel and its applications," *Materials Letters*, vol. 248, pp. 241–245, 2019.
- [62] P. J. Reynoso-García, M. Güizado-Rodríguez, V. Barba, G. Ramos-Ortiz, and H. Martínez-Gutiérrez, "Stabilization of silver nanoparticles with a dithiocarbamate ligand and formation of nanocomposites by combination with polythiophene derivative nanoparticles," *Advances in Condensed Matter Physics*, vol. 2018, Article ID 4376051, 9 pages, 2018.
- [63] B. Chouchene, T. B. Chaabane, K. Mozet et al., "Porous Al-doped ZnO rods with selective adsorption properties," *Applied Surface Science*, vol. 409, pp. 102–110, 2017.
- [64] R. Vinodkumar, I. Navas, S. R. Chalana et al., "Highly conductive and transparent laser ablated nanostructured Al: ZnO thin films," *Applied Surface Science*, vol. 257, no. 3, pp. 708–716, 2010.
- [65] H. A. Sani, M. B. Ahmad, M. Z. Hussein, N. A. Ibrahim, A. Musa, and T. A. Saleh, "Nanocomposite of ZnO with montmorillonite for removal of lead and copper ions from aqueous solutions," *Process Safety and Environmental Protection*, vol. 109, pp. 97–105, 2017.
- [66] Z. Ma, D. Zhao, Y. Chang, S. Xing, Y. Wu, and Y. Gao, "Synthesis of MnFe₂O₄@Mn-Co oxide core-shell nanoparticles and their excellent performance for heavy metal removal," *Dalton Transactions*, vol. 42, no. 39, pp. 14261–14267, 2013.
- [67] M. Kokate, K. Garadkar, and A. Gole, "One pot synthesis of magnetite-silica nanocomposites: applications as tags, entrapment matrix and in water purification," *Journal of Materials Chemistry A*, vol. 1, no. 6, pp. 2022–2029, 2013.
- [68] A. J. S. Ahammad, J.-J. Lee, and M. A. Rahman, "Electrochemical sensors based on carbon nanotubes," *Sensors*, vol. 9, no. 4, pp. 2289–2319, 2009.
- [69] A. I. Ayesha, "Metal/metal-oxide nanoclusters for gas sensor applications," *Journal of Nanomaterials*, vol. 2016, Article ID 2359019, 17 pages, 2016.
- [70] S. Su, W. Wu, J. Gao, J. Lu, and C. Fan, "Nanomaterials-based sensors for applications in environmental monitoring," *Journal of Materials Chemistry*, vol. 22, no. 35, pp. 18101–18110, 2012.
- [71] V. D. N. Bezzon, T. L. A. Montanheiro, B. R. C. de Menezes et al., "Carbon nanostructure-based sensors: a brief review on recent advances," *Advances in Materials Science and Engineering*, vol. 2019, Article ID 4293073, 21 pages, 2019.
- [72] S. Mehdi Aghaei, M. M. Monshi, I. Torres, S. M. J. Zeidi, and I. Calizo, "DFT study of adsorption behavior of NO, CO, NO₂, and NH₃ molecules on graphene-like BC₃: a search for highly sensitive molecular sensor," *Applied Surface Science*, vol. 427, pp. 326–333, 2018.
- [73] Y. P. Zhao, S. H. Li, S. B. Chaney et al., "Designing nanostructures for sensor applications," *Journal of Electronic Materials*, vol. 35, no. 5, pp. 846–851, 2006.
- [74] R. Abdel-Karim, Y. Reda, and A. Abdel-Fattah, "Review—nanostructured materials-based nanosensors," *Journal of the Electrochemical Society*, vol. 167, no. 3, article 037554, 2020.

- [75] X. Luo, A. Morrin, A. J. Killard, and M. R. Smyth, "Application of nanoparticles in electrochemical sensors and biosensors," *Electroanalysis*, vol. 18, no. 4, pp. 319–326, 2006.
- [76] G. Maduraiveeran and W. Jin, "Nanomaterials based electrochemical sensor and biosensor platforms for environmental applications," *Trends in Environmental Analytical Chemistry*, vol. 13, pp. 10–23, 2017.
- [77] R. M. Pallares, N. T. K. Thanh, and X. Su, "Sensing of circulating cancer biomarkers with metal nanoparticles," *Nanoscale*, vol. 11, no. 46, pp. 22152–22171, 2019.
- [78] M. Lin, H. Pei, F. Yang, C. Fan, and X. Zuo, "Applications of gold nanoparticles in the detection and identification of infectious diseases and biothreats," *Advanced Materials*, vol. 25, no. 25, pp. 3490–3496, 2013.
- [79] G. Doria, J. Conde, B. Veigas et al., "Noble metal nanoparticles for biosensing applications," *Sensors*, vol. 12, no. 2, pp. 1657–1687, 2012.
- [80] J. Sun, Y. Lu, L. He, J. Pang, F. Yang, and Y. Liu, "Colorimetric sensor array based on gold nanoparticles: design principles and recent advances," *TrAC Trends in Analytical Chemistry*, vol. 122, p. 115754, 2020.
- [81] X. Che, R. Yuan, Y. Chai, J. Li, Z. Song, and J. Wang, "Amperometric immunosensor for the determination of α -1-fetoprotein based on multiwalled carbon nanotube–silver nanoparticle composite," *Journal of Colloid and Interface Science*, vol. 345, no. 2, pp. 174–180, 2010.
- [82] A. de la Escosura-Muñiz, M. Maltez-da Costa, C. Sánchez-Espinel et al., "Gold nanoparticle-based electrochemical magnetosensor for rapid detection of anti-hepatitis B virus antibodies in human serum," *Biosensors and Bioelectronics*, vol. 26, no. 4, pp. 1710–1714, 2010.
- [83] A. Ambrosi, F. Airò, and A. Merkoçi, "Enhanced gold nanoparticle based ELISA for a breast cancer biomarker," *Analytical Chemistry*, vol. 82, no. 3, pp. 1151–1156, 2010.
- [84] P. Costa, A. Amaro, A. Botelho, J. Inácio, and P. V. Baptista, "Gold nanoprobe assay for the identification of mycobacteria of the *Mycobacterium tuberculosis* complex," *Clinical Microbiology and Infection*, vol. 16, no. 9, pp. 1464–1469, 2010.
- [85] M. B. Wabuyele and T. Vo-Dinh, "Detection of human immunodeficiency virus type 1 DNA sequence using plasmonics nanoprobes," *Analytical Chemistry*, vol. 77, no. 23, pp. 7810–7815, 2005.
- [86] E. Priyadarshini and N. Pradhan, "Gold nanoparticles as efficient sensors in colorimetric detection of toxic metal ions: a review," *Sensors and Actuators B: Chemical*, vol. 238, pp. 888–902, 2017.
- [87] P. Goel and M. Arora, "Fabrication of chemical sensor for organochlorine pesticide detection using colloidal gold nanoparticles," *MRS Communications*, vol. 8, no. 3, pp. 1000–1007, 2018.
- [88] Y. Hu, S. Hua, F. Li et al., "Green-synthesized gold nanoparticles decorated graphene sheets for label-free electrochemical impedance DNA hybridization biosensing," *Biosensors and Bioelectronics*, vol. 26, no. 11, pp. 4355–4361, 2011.
- [89] T. S. Santra, F.-G. Tseng, and T. K. Barik, "Green biosynthesis of gold nanoparticles and biomedical applications," *Journal of Nano Research and Application*, vol. 2, no. 6-2, pp. 5–12, 2014.
- [90] P. Kuppusamy, M. Y. Mashitah, G. P. Maniam, and N. Govindan, "Biosynthesized gold nanoparticle developed as a tool for detection of HCG hormone in pregnant women urine sample," *Asian Pacific Journal of Tropical Disease*, vol. 4, no. 3, p. 237, 2014.
- [91] M. Ateeq, M. R. Shah, N. Ain et al., "Green synthesis and molecular recognition ability of patuletin coated gold nanoparticles," *Biosensors and Bioelectronics*, vol. 63, pp. 499–505, 2015.
- [92] S. Pandey, G. K. Goswami, and K. K. Nanda, "Green synthesis of biopolymer–silver nanoparticle nanocomposite: an optical sensor for ammonia detection," *International Journal of Biological Macromolecules*, vol. 51, no. 4, pp. 583–589, 2012.
- [93] R. Kotcherlakota, S. Das, and C. R. Patra, "Therapeutic applications of green-synthesized silver nanoparticles," in *Green Synthesis, Characterization and Applications of Nanoparticles*, S. I. A. Shukla, Ed., pp. 389–428, Elsevier, 2018.
- [94] V. M. Kariuki, S. A. Fasih-Ahmad, F. J. Osonga, and O. A. Sadik, "An electrochemical sensor for nitrobenzene using π -conjugated polymer-embedded nanosilver," *Analyst*, vol. 141, no. 7, pp. 2259–2269, 2016.
- [95] L. Sepunaru, B. J. Plowman, S. V. Sokolov, N. P. Young, and R. G. Compton, "Rapid electrochemical detection of single influenza viruses tagged with silver nanoparticles," *Chemical Science*, vol. 7, no. 6, pp. 3892–3899, 2016.
- [96] S. Palanisamy, H. F. Lee, S. M. Chen, and B. Thirumalraj, "An electrochemical facile fabrication of platinum nanoparticle decorated reduced graphene oxide; application for enhanced electrochemical sensing of H_2O_2 ," *RSC Advances*, vol. 5, no. 128, pp. 105567–105573, 2015.
- [97] R. Jiménez-Pérez, J. González-Rodríguez, M. I. González-Sánchez, B. Gómez-Monedero, and E. Valero, "Highly sensitive H_2O_2 sensor based on poly(azure A)-platinum nanoparticles deposited on activated screen printed carbon electrodes," *Sensors and Actuators B: Chemical*, vol. 298, article 126878, 2019.
- [98] G. Yin, L. Xing, X. J. Ma, and J. Wan, "Non-enzymatic hydrogen peroxide sensor based on a nanoporous gold electrode modified with platinum nanoparticles," *Chemical Papers*, vol. 68, no. 4, 2014.
- [99] R.-M. Song, Z. H. Li, P. J. Wei, X. L. Zhao, C. Chen, and Z. G. Zhu, "Flexible hydrogen peroxide sensors based on platinum modified free-standing reduced graphene oxide paper," *Applied Sciences*, vol. 8, no. 6, p. 848, 2018.
- [100] A. Safavi and F. Farjami, "Electrodeposition of gold–platinum alloy nanoparticles on ionic liquid–chitosan composite film and its application in fabricating an amperometric cholesterol biosensor," *Biosensors and Bioelectronics*, vol. 26, no. 5, pp. 2547–2552, 2011.
- [101] M. R. Mahmoudian, W. J. Basirun, and Y. Alias, "A sensitive electrochemical Hg^{2+} ions sensor based on polypyrrole coated nanospherical platinum," *RSC Advances*, vol. 6, no. 43, pp. 36459–36466, 2016.
- [102] S.-W. Jung, E. K. Lee, and S.-Y. Lee, "Communication—concentration-cell-type nafion-based potentiometric hydrogen sensors," *ECS Journal of Solid State Science and Technology*, vol. 7, no. 12, pp. Q239–Q241, 2018.
- [103] R. Xi, S. H. Zhang, L. Zhang et al., "Electrodeposition of Pd-Pt nanocomposites on porous GaN for electrochemical nitrite sensing," *Sensors*, vol. 19, no. 3, p. 606, 2019.
- [104] M. Govindhan, Z. Liu, and A. Chen, "Design and electrochemical study of platinum-based nanomaterials for sensitive detection of nitric oxide in biomedical applications," *Nanomaterials*, vol. 6, no. 11, p. 211, 2016.

- [105] M. R. Mahmoudian, Y. Alias, W. J. Basirun et al., "A sensitive electrochemical nitrate sensor based on polypyrrole coated palladium nanoclusters," *Journal of Electroanalytical Chemistry*, vol. 751, pp. 30–36, 2015.
- [106] J. Sophia and G. Muralidharan, "Polyvinylpyrrolidone stabilized palladium nanospheres as simple and novel electrochemical sensor for amperometric hydrogen peroxide detection," *Journal of Electroanalytical Chemistry*, vol. 739, pp. 115–121, 2015.
- [107] Y. Li, J. Z. Sun, C. Bian et al., "Copper nano-clusters prepared by one-step electrodeposition and its application on nitrate sensing," *AIP Advances*, vol. 5, no. 4, article 041312, 2015.
- [108] S. A. Ghoto, M. Y. Khuhawar, T. M. Jahangir, and J. . D. Mangi, "Applications of copper nanoparticles for colorimetric detection of dithiocarbamate pesticides," *Journal of Nanostructure in Chemistry*, vol. 9, no. 2, pp. 77–93, 2019.
- [109] Q. Li, F. Wu, M. Mao et al., "A dual-mode colorimetric sensor based on copper nanoparticles for the detection of mercury(II) ions," *Analytical Methods*, vol. 11, no. 31, pp. 4014–4021, 2019.
- [110] D. Nunes, A. Pimentel, A. Gonçalves et al., "Metal oxide nanostructures for sensor applications," *Semiconductor Science and Technology*, vol. 34, no. 4, article 043001, 2019.
- [111] A. Staerz, U. Weimar, and N. Barsan, "Understanding the potential of WO₃ based sensors for breath analysis," *Sensors*, vol. 16, no. 11, p. 1815, 2016.
- [112] X. Gao, Q. Zhou, Z. Lu, L. Xu, Q. Zhang, and W. Zeng, "Synthesis of Cr₂O₃ nanoparticle-coated SnO₂ nanofibers and C₂H₂ sensing properties," *Frontiers in Materials*, vol. 6, no. 163, 2019.
- [113] H. Chen, R. Bo, A. Shrestha et al., "NiO–ZnO nanoheterojunction networks for room-temperature volatile organic compounds sensing," *Advanced Optical Materials*, vol. 6, no. 22, article 1800677, 2018.
- [114] H. Wang, D. Wang, L. Tian et al., "Graphene-like porous ZnO/graphene oxide nanosheets for high-performance acetone vapor detection," *Molecules*, vol. 24, no. 3, p. 522, 2019.
- [115] K. Zhang, S. Qin, P. Tang, Y. Feng, and D. Li, "Ultra-sensitive ethanol gas sensors based on nanosheet-assembled hierarchical ZnO–In₂O₃ heterostructures," *Journal of Hazardous Materials*, vol. 391, article 122191, 2020.
- [116] S. J. Choi, I. Lee, B. H. Jang et al., "Selective diagnosis of diabetes using Pt-functionalized WO₃Hemitube networks as a sensing layer of acetone in exhaled breath," *Analytical Chemistry*, vol. 85, no. 3, pp. 1792–1796, 2013.
- [117] S. J. Choi, F. Fuchs, R. Demadrille et al., "Fast responding exhaled-breath sensors using WO₃ hemitubes functionalized by graphene-based electronic sensitizers for diagnosis of diseases," *ACS Applied Materials & Interfaces*, vol. 6, no. 12, pp. 9061–9070, 2014.
- [118] S. J. Choi, B. H. Jang, S. J. Lee, B. K. Min, A. Rothschild, and I. D. Kim, "Selective detection of acetone and hydrogen sulfide for the diagnosis of diabetes and halitosis using SnO(2) nanofibers functionalized with reduced graphene oxide nanosheets," *ACS Applied Materials & Interfaces*, vol. 6, no. 4, pp. 2588–2597, 2014.
- [119] K. Wan, J. Yang, D. Wang, and X. Wang, "Graphene oxide@3D hierarchical SnO₂ nanofiber/nanosheets nanocomposites for highly sensitive and low-temperature formaldehyde detection," *Molecules*, vol. 25, no. 1, p. 35, 2020.
- [120] D. Wang, L. Tian, H. Li et al., "Mesoporous ultrathin SnO₂-Nanosheets in situ modified by graphene oxide for extraordinary formaldehyde detection at low temperatures," *ACS Applied Materials & Interfaces*, vol. 11, no. 13, pp. 12808–12818, 2019.
- [121] K. Wan, D. Wang, F. Wang et al., "Hierarchical In₂O₃@SnO₂Core–Shell Nanofiber for high efficiency formaldehyde detection," *ACS Applied Materials & Interfaces*, vol. 11, no. 48, pp. 45214–45225, 2019.
- [122] A. Eatemadi, H. Daraee, H. Karimkhanloo et al., "Carbon nanotubes: properties, synthesis, purification, and medical applications," *Nanoscale Research Letters*, vol. 9, no. 1, p. 393, 2014.
- [123] L. Camilli and M. Passacantando, "Advances on sensors based on carbon nanotubes," *Chemosensors*, vol. 6, no. 4, p. 62, 2018.
- [124] R. Andrews, D. Jacques, D. Qian, and T. Rantell, "Multiwall carbon nanotubes: synthesis and application," *Accounts of Chemical Research*, vol. 35, no. 12, pp. 1008–1017, 2002.
- [125] J. F. Colomer, C. Stephan, S. Lefrant et al., "Large-scale synthesis of single-wall carbon nanotubes by catalytic chemical vapor deposition (CCVD) method," *Chemical Physics Letters*, vol. 317, no. 1–2, pp. 83–89, 2000.
- [126] C. Ursino, R. Castro-Muñoz, E. Drioli, L. Gzara, M. Albeirutty, and A. Figoli, "Progress of nanocomposite membranes for water treatment," *Membranes*, vol. 8, no. 2, p. 18, 2018.
- [127] I. V. Zaporotskova, N. P. Boroznina, Y. N. Parkhomenko, and L. V. Kozhitov, "Carbon nanotubes: sensor properties. A review," *Modern Electronic Materials*, vol. 2, no. 4, pp. 95–105, 2016.
- [128] K. F. Akhmadishina, I. I. Bobrinetskii, I. A. Komarov et al., "Flexible biological sensors based on carbon nanotube films," *Nanotechnologies in Russia*, vol. 8, no. 11–12, pp. 721–726, 2013.
- [129] Y. Wang and J. T. W. Yeow, "A review of carbon nanotubes-based gas sensors," *Journal of Sensors*, vol. 2009, Article ID 493904, 24 pages, 2009.
- [130] X. Zhang, H. Cui, Y. Gui, and J. Tang, "Mechanism and application of carbon nanotube sensors in SF₆ decomposed production detection: a review," *Nanoscale Research Letters*, vol. 12, no. 1, p. 177, 2017.
- [131] J. Suehiro, G. Zhou, and M. Hara, "Fabrication of a carbon nanotube-based gas sensor using dielectrophoresis and its application for ammonia detection by impedance spectroscopy," *Journal of Physics D: Applied Physics*, vol. 36, no. 21, pp. L109–L114, 2003.
- [132] S. K. Vashist, D. Zheng, K. al-Rubeaan, J. H. T. Luong, and F. S. Sheu, "Advances in carbon nanotube based electrochemical sensors for bioanalytical applications," *Biotechnology Advances*, vol. 29, no. 2, pp. 169–188, 2011.
- [133] K. A. Williams and P. C. Eklund, "Monte Carlo simulations of H₂ physisorption in finite-diameter carbon nanotube ropes," *Chemical Physics Letters*, vol. 320, no. 3–4, pp. 352–358, 2000.
- [134] C. S. Yeung, L. V. Liu, and Y. A. Wang, "Adsorption of small gas molecules onto Pt-doped single-walled carbon nanotubes," *The Journal of Physical Chemistry C*, vol. 112, no. 19, pp. 7401–7411, 2008.
- [135] M. Yoosefian, M. Zahedi, A. Mola, and S. Naserian, "A DFT comparative study of single and double SO₂ adsorption on Pt-doped and Au-doped single-walled carbon nanotube," *Applied Surface Science*, vol. 349, pp. 864–869, 2015.

- [136] X. Zhou, W. Q. Tian, and X.-L. Wang, "Adsorption sensitivity of Pd-doped SWCNTs to small gas molecules," *Sensors and Actuators B: Chemical*, vol. 151, no. 1, pp. 56–64, 2010.
- [137] S. Seenithurai, R. Kodi Pandyan, S. Vinodh Kumar, and M. Mahendran, "H₂ adsorption in Ni and passivated Ni doped 4 Å single walled carbon nanotube," *International Journal of Hydrogen Energy*, vol. 38, no. 18, pp. 7376–7381, 2013.
- [138] H. Nakano, H. Ohta, A. Yokoe, K. Doi, and A. Tachibana, "First-principle molecular-dynamics study of hydrogen adsorption on an aluminum-doped carbon nanotube," *Journal of Power Sources*, vol. 163, no. 1, pp. 125–134, 2006.
- [139] Z. Zhou, X. Gao, J. Yan, and D. Song, "Doping effects of B and N on hydrogen adsorption in single-walled carbon nanotubes through density functional calculations," *Carbon*, vol. 44, no. 5, pp. 939–947, 2006.
- [140] X. Zhang, Y. Gui, and Z. Dai, "A simulation of Pd-doped SWCNTs used to detect SF₆ decomposition components under partial discharge," *Applied Surface Science*, vol. 315, pp. 196–202, 2014.
- [141] X. Zhang, Z. Dai, Q. Chen, and J. Tang, "A DFT study of SO₂ and H₂S gas adsorption on Au-doped single-walled carbon nanotubes," *Physica Scripta*, vol. 89, no. 6, article 065803, 2014.
- [142] X. Zhang, B. Feng, J. Zhang, J. Tang, and W. Liu, "Gas sensing response of NiCl₂-doped carbon nanotubes to decomposition products of SF₆ gas due to partial discharge," *Power System Technology*, vol. 35, no. 10, pp. 189–193, 2011.
- [143] X. Zhang, B. Yang, Z. Dai, and C. Luo, "The gas response of hydroxyl modified SWCNTs and carboxyl modified SWCNTs to H₂S and SO₂," *Electrical Review*, vol. 88, no. 7B, pp. 311–314, 2012.
- [144] X. Zhang, F. Meng, and B. Yang, "Use of hydroxyl-modified carbon nanotubes for detecting SF₆ decomposition products under partial discharge in gas insulated switchgear," *IEEE Transactions on Dielectrics and Electrical Insulation*, vol. 20, no. 6, pp. 2246–2253, 2013.
- [145] T. Zhang, S. Mubeen, E. Bekyarova et al., "Poly(m-aminobenzenesulfonic acid) functionalized single-walled carbon nanotubes based gas sensor," *Nanotechnology*, vol. 18, no. 16, article 165504, 2007.
- [146] I. Sayago, H. Santos, M. Horrillo et al., "Carbon nanotube networks as gas sensors for NO₂ detection," *Talanta*, vol. 77, no. 2, pp. 758–764, 2008.
- [147] A. N. Naje, R. R. Ibraheem, and F. T. Ibrahim, "Parametric analysis of NO₂ gas sensor based on carbon nanotubes," *Photonic Sensors*, vol. 6, no. 2, pp. 153–157, 2016.
- [148] A. Kausar, "Detection of environmentally hazardous nitrogen oxide pollutants using polythiophene derivative/carbon nanotube-based nanocomposite," *Frontiers in Science*, vol. 1, no. 1, pp. 23–26, 2017.
- [149] F. Rigoni, S. Tognolini, P. Borghetti et al., "Enhancing the sensitivity of chemiresistor gas sensors based on pristine carbon nanotubes to detect low-ppb ammonia concentrations in the environment," *Analyst*, vol. 138, no. 24, pp. 7392–7399, 2013.
- [150] F. Rigoni, G. Drera, S. Pagliara, A. Goldoni, and L. Sangaletti, "High sensitivity, moisture selective, ammonia gas sensors based on single-walled carbon nanotubes functionalized with indium tin oxide nanoparticles," *Carbon*, vol. 80, pp. 356–363, 2014.
- [151] L. A. Panes-Ruiz, M. Shaygan, Y. Fu et al., "Toward highly sensitive and energy efficient ammonia gas detection with modified single-walled carbon nanotubes at room temperature," *ACS Sensors*, vol. 3, no. 1, pp. 79–86, 2017.
- [152] H. Lee, G. Shaker, K. Naishadham et al., "Carbon-nanotube loaded antenna-based Ammonia gas sensor," *IEEE Transactions on Microwave Theory and Techniques*, vol. 59, no. 10, pp. 2665–2673, 2011.
- [153] W. Zhao, D. W. H. Fam, Z. Yin et al., "A carbon monoxide gas sensor using oxygen plasma modified carbon nanotubes," *Nanotechnology*, vol. 23, no. 42, p. 425502, 2012.
- [154] A. M. Souza, A. R. Rocha, A. Fazzio, and A. J. R. da Silva, "Ab-initio calculations for a realistic sensor: a study of CO sensors based on nitrogen-rich carbon nanotubes," *AIP Advances*, vol. 2, no. 3, article 032115, 2012.
- [155] M. Moradi, A. Aghakhani, and M. J. Eshraghi, "Dispersion-corrected DFT study on the carbon monoxide sensing by B₂C nanotubes: effects of dopant and interferences," *Structural Chemistry*, vol. 27, no. 2, pp. 535–542, 2016.
- [156] G. Zhang, H. L. Tai, G. Z. Xie, Y. D. Jiang, and Y. Zhou, "A carbon monoxide sensor based on single-walled carbon nanotubes doped with copper chloride," *SCIENCE CHINA Technological Sciences*, vol. 56, no. 10, pp. 2576–2580, 2013.
- [157] S. F. Liu, S. Lin, and T. M. Swager, "An organocobalt–carbon nanotube chemiresistive carbon monoxide detector," *ACS Sensors*, vol. 1, no. 4, pp. 354–357, 2016.
- [158] L. H. H. Hsu, E. Hoque, P. Kruse, and P. Ravi Selvaganapathy, "A carbon nanotube based resettable sensor for measuring free chlorine in drinking water," *Applied Physics Letters*, vol. 106, no. 6, article 063102, 2015.
- [159] J. Muñoz, F. Céspedes, and M. Baeza, "Modified multiwalled carbon nanotube/epoxy amperometric nanocomposite sensors with CuO nanoparticles for electrocatalytic detection of free chlorine," *Microchemical Journal*, vol. 122, pp. 189–196, 2015.
- [160] R. Olivé-Monllau, A. Pereira, J. Bartrolí, M. Baeza, and F. Céspedes, "Highly sensitive CNT composite amperometric sensors integrated in an automated flow system for the determination of free chlorine in waters," *Talanta*, vol. 81, no. 4–5, pp. 1593–1598, 2010.
- [161] N. Kumar and L. S. B. Upadhyay, "19 - Polymeric gels for biosensing applications," in *Polymeric Gels*, K. Pal and I. Banerjee, Eds., pp. 487–503, Woodhead Publishing, 2018.
- [162] P. Parkhey and S. V. Mohan, "Chapter 6.1 - Biosensing applications of microbial fuel cell: approach toward miniaturization," in *Microbial Electrochemical Technology*, S. V. Mohan, S. Varjani, and A. Pandey, Eds., pp. 977–997, Elsevier, 2019.
- [163] C.-M. Tilmaciu and M. C. Morris, "Carbon nanotube biosensors," *Frontiers in Chemistry*, vol. 3, pp. 59–59, 2015.
- [164] E. Arkan, R. Saber, Z. Karimi, and M. Shamsipur, "A novel antibody–antigen based impedimetric immunosensor for low level detection of HER2 in serum samples of breast cancer patients via modification of a gold nanoparticles decorated multiwall carbon nanotube-ionic liquid electrode," *Analytica Chimica Acta*, vol. 874, pp. 66–74, 2015.
- [165] M. M. Barsan, M. E. Ghica, and C. M. A. Brett, "Electrochemical sensors and biosensors based on redox polymer/carbon nanotube modified electrodes: a review," *Analytica Chimica Acta*, vol. 881, pp. 1–23, 2015.
- [166] M. D. Rubianes and G. A. Rivas, "Carbon nanotubes paste electrode," *Electrochemistry Communications*, vol. 5, no. 8, pp. 689–694, 2003.

- [167] V. Pifferi, M. M. Barsan, M. E. Ghica, L. Falcicola, and C. M. A. Brett, "Synthesis, characterization and influence of poly(brilliant green) on the performance of different electrode architectures based on carbon nanotubes and poly(3,4-ethylenedioxythiophene)," *Electrochimica Acta*, vol. 98, pp. 199–207, 2013.
- [168] M. Pedano and G. A. Rivas, "Adsorption and electrooxidation of nucleic acids at carbon nanotubes paste electrodes," *Electrochemistry Communications*, vol. 6, no. 1, pp. 10–16, 2004.
- [169] H.-J. Liu, D.-W. Yang, and H.-H. Liu, "A hydrogen peroxide sensor based on the nanocomposites of poly(brilliant cresyl blue) and single walled-carbon nanotubes," *Analytical Methods*, vol. 4, no. 5, pp. 1421–1426, 2012.
- [170] M. E. Ghica, Y. Wintersteller, and C. M. A. Brett, "Poly(brilliant green)/carbon nanotube-modified carbon film electrodes and application as sensors," *Journal of Solid State Electrochemistry*, vol. 17, no. 6, pp. 1571–1580, 2013.
- [171] M. E. Ghica and C. M. A. Brett, "Poly(brilliant green) and poly(thionine) modified carbon nanotube coated carbon film electrodes for glucose and uric acid biosensors," *Talanta*, vol. 130, pp. 198–206, 2014.
- [172] A. de la Zerda, Z. Liu, S. Bodapati et al., "Ultrahigh sensitivity carbon nanotube agents for photoacoustic molecular imaging in living mice," *Nano Letters*, vol. 10, no. 6, pp. 2168–2172, 2010.
- [173] X. Wang, C. Wang, K. Qu et al., "Ultrasensitive and selective detection of a prognostic indicator in early-stage cancer using graphene oxide and carbon nanotubes," *Advanced Functional Materials*, vol. 20, no. 22, pp. 3967–3971, 2010.
- [174] M. Rouse <https://whatis.techtarget.com/definition/photosensor>.
- [175] M. Navvab, C. Burattini, F. Bisegna, and F. Gugliermetti, "Chapter 8 - Building automation for energy efficiency," in *Handbook of Energy Efficiency in Buildings*, F. Asdrubali and U. Desideri, Eds., pp. 597–673, Butterworth-Heinemann, 2019.
- [176] C.-M. Lin and W. Fang, "Batch-fabricated flexible carbon nanotubes' photosensor array," *Nanotechnology*, vol. 20, no. 46, p. 465502, 2009.
- [177] M. Yang, J. Xu, J. Wei, J. L. Sun, W. Liu, and J. L. Zhu, "Fabrication of double-walled carbon nanotube film/Cu₂O nanoparticle film/TiO₂nanotube array heterojunctions for photosensors," *Applied Physics Letters*, vol. 100, no. 25, article 253113, 2012.
- [178] X. Wu, B. Zhou, J. Zhou, Y. Chen, Y. Chu, and J. Huang, "Distinguishable detection of ultraviolet, visible, and infrared spectrum with high-responsivity perovskite-based flexible photosensors," *Small*, vol. 14, no. 19, article 1800527, 2018.
- [179] HBM <https://www.hbm.com/en/7646/what-is-a-pressure-sensor/>.
- [180] A. Cao, P. L. Dickrell, W. G. Sawyer, M. N. Ghasemi-Nejhad, and P. M. Ajayan, "Super-compressible foamlike carbon nanotube films," *Science*, vol. 310, no. 5752, pp. 1307–1310, 2005.
- [181] V. L. Pushparaj, L. Ci, S. Sreekala et al., "Effects of compressive strains on electrical conductivities of a macroscale carbon nanotube block," *Applied Physics Letters*, vol. 91, no. 15, p. 153116, 2007.
- [182] H.-M. So, J. W. Sim, J. Kwon, J. Yun, S. Baik, and W. S. Chang, "Carbon nanotube based pressure sensor for flexible electronics," *Materials Research Bulletin*, vol. 48, no. 12, pp. 5036–5039, 2013.
- [183] S. M. Doshi and E. T. Thostenson, "Thin and flexible carbon nanotube-based pressure sensors with ultrawide sensing range," *ACS sensors*, vol. 3, no. 7, pp. 1276–1282, 2018.
- [184] M. Adamczak, G. Kamińska, and J. Bohdziewicz, "Preparation of polymer membranes by in situ interfacial polymerization," *International Journal of Polymer Science*, vol. 2019, Article ID 6217924, 13 pages, 2019.
- [185] F. R. Passador, A. Ruvolo-Filho, and L. A. Pessan, "7 - Nanocomposites of polymer matrices and lamellar clays," in *Nanostructures*, A. L. Róz, Ed., pp. 187–207, William Andrew Publishing, 2017.
- [186] Y. Ying, W. Ying, Q. Li et al., "Recent advances of nanomaterial-based membrane for water purification," *Applied Materials Today*, vol. 7, pp. 144–158, 2017.
- [187] T. C. Huang, J. M. Yeh, and C. Y. Lai, "18 - Polymer nanocomposite coatings," in *Advances in Polymer Nanocomposites*, F. Gao, Ed., pp. 605–638, Woodhead Publishing, 2012.
- [188] H. D. Beyene and T. G. Ambaye, "Application of sustainable nanocomposites for water purification process," in *Sustainable Polymer Composites and Nanocomposites*, Inamuddin, pp. 387–412, Springer International Publishing, Cham, 2019.
- [189] T. Tian, X. Shi, L. Cheng et al., "Graphene-based nanocomposite as an effective, multifunctional, and recyclable antibacterial agent," *ACS Applied Materials & Interfaces*, vol. 6, no. 11, pp. 8542–8548, 2014.
- [190] S. Zhao, Z. Wang, X. Wei et al., "Performance improvement of polysulfone ultrafiltration membrane using well-dispersed polyaniline-poly(vinylpyrrolidone) nanocomposite as the additive," *Industrial & Engineering Chemistry Research*, vol. 51, no. 12, pp. 4661–4672, 2012.
- [191] J. Hyun, S. Min, I. Jun, J. Won, Y. Hwa, and Mohammad, "Carbon nanotube embedded multi-functional polymer nanocomposites, Nanocomposites," in *Nanocomposites: New Trends and Developments*, F. Ebrahimi, Ed., pp. 17–35, IntechOpen, 2012.
- [192] E. I. Akpan, X. Shen, B. Wetzel, and K. Friedrich, "2 - Design and synthesis of polymer nanocomposites," in *Polymer Composites with Functionalized Nanoparticles*, K. Pielichowski and T. M. Majka, Eds., pp. 47–83, Elsevier, 2019.
- [193] T. Hanemann and D. V. Szabó, "Polymer-nanoparticle composites: from synthesis to modern applications," *Materials*, vol. 3, no. 6, pp. 3468–3517, 2010.
- [194] B. Tang, Z. Huo, and P. Wu, "Study on a novel polyester composite nanofiltration membrane by interfacial polymerization of triethanolamine (TEOA) and trimesoyl chloride (TMC)," *Journal of Membrane Science*, vol. 320, no. 1-2, pp. 198–205, 2008.
- [195] B. John, "Polymer nanocomposite-based electrochemical sensors and biosensors," in *Nanorods and Nanocomposites*, IntechOpen, 2020.
- [196] R. Devi, M. Thakur, and C. S. Pundir, "Construction and application of an amperometric xanthine biosensor based on zinc oxide nanoparticles-polypyrrole composite film," *Biosensors & Bioelectronics*, vol. 26, no. 8, pp. 3420–3426, 2011.
- [197] L. Xing, Q. Rong, and Z. Ma, "Non-enzymatic electrochemical sensing of hydrogen peroxide based on polypyrrole/platinum nanocomposites," *Sensors and Actuators B: Chemical*, vol. 221, pp. 242–247, 2015.
- [198] Z. Yu, H. Li, X. Zhang et al., "Facile synthesis of NiCo₂O₄@Polyaniline core-shell nanocomposite for sensitive determination

- of glucose,” *Biosensors & Bioelectronics*, vol. 75, pp. 161–165, 2016.
- [199] Y. Fan, J. H. Liu, C. P. Yang, M. Yu, and P. Liu, “Graphene–polyaniline composite film modified electrode for voltammetric determination of 4-aminophenol,” *Sensors and Actuators B: Chemical*, vol. 157, no. 2, pp. 669–674, 2011.
- [200] K. Radhapyari, P. Kotoky, M. R. Das, and R. Khan, “Graphene–polyaniline nanocomposite based biosensor for detection of antimalarial drug artesunate in pharmaceutical formulation and biological fluids,” *Talanta*, vol. 111, pp. 47–53, 2013.
- [201] R. Jain, D. C. Tiwari, and S. Shrivastava, “A sensitive voltammetric sensor based on synergistic effect of polyaniline and zirconia nanocomposite film for quantification of proton pump inhibitor esomeprazole,” *Journal of the Electrochemical Society*, vol. 161, no. 4, pp. B39–B44, 2014.
- [202] X. Ma, T. Miao, W. Zhu et al., “Electrochemical detection of nitrite based on glassy carbon electrode modified with gold–polyaniline–graphene nanocomposites,” *RSC Advances*, vol. 4, no. 101, pp. 57842–57849, 2014.
- [203] Y.-S. Gao, J. K. Xu, L. M. Lu et al., “Overoxidized polypyrrole/graphene nanocomposite with good electrochemical performance as novel electrode material for the detection of adenine and guanine,” *Biosensors and Bioelectronics*, vol. 62, pp. 261–267, 2014.
- [204] H. Mao, J. Liang, H. Zhang et al., “Poly(ionic liquids) functionalized polypyrrole/graphene oxide nanosheets for electrochemical sensor to detect dopamine in the presence of ascorbic acid,” *Biosensors and Bioelectronics*, vol. 70, pp. 289–298, 2015.
- [205] L. Lu, O. Zhang, J. Xu et al., “A facile one-step redox route for the synthesis of graphene/poly (3,4-ethylenedioxythiophene) nanocomposite and their applications in biosensing,” *Sensors and Actuators B: Chemical*, vol. 181, pp. 567–574, 2013.
- [206] R. Jain and S. Shrivastava, “A graphene-polyaniline-Bi₂O₃ hybrid film sensor for voltammetric quantification of anti-inflammatory drug Etodolac,” *Journal of the Electrochemical Society*, vol. 161, no. 4, pp. H189–H194, 2014.
- [207] X. Tan, L. Zhang, X. Deng, L. Miao, H. Li, and G. zheng, “Redox active molybdophosphate produced by Cu₃(PO₄)₂-nanospheres for enhancing enzyme-free electrochemical immunoassay of C-reactive protein,” *New Journal of Chemistry*, vol. 41, no. 20, pp. 11867–11871, 2017.